Forward Modelling and Imaging Method Studies for Cross-Hole Radio Imaging (RIM) Data

by

Yongxing Li

A thesis submitted in partial fulfillment
of the requirements for the degree of
Doctor of Philosophy (PhD) in Mineral Deposits and Precambrian Geology

The Faculty of Graduate Studies
Laurentian University
Sudbury, Ontario, Canada

THESIS DEFENCE COMMITTEE/COMITÉ DE SOUTENANCE DE THÈSE
Laurentian Université/Université Laurentienne
Faculty of Graduate Studies/Faculté des études supérieures

Title of Thesis Titre de la thèse	Forward Modelling and Imaging Method Studies for Cross-Hole Radio Imaging (RIM) Data
Name of Candidate Nom du candidat	Li, Yongxing
Degree Diplôme	Doctor of Philosophy
Department/Program Département/Programme	Date of Defence: June 6, 2017 PhD Mineral Deposits and Pre-Cambrian Geology

APPROVED/APPROUVÉ

Thesis Examiners/Examinateurs de thèse:

Dr. Richard Smith
(Supervisor/Directeur(trice) de thèse)

Dr. Ralph Meyer
(Committee member/Membre du comité)

Dr. Glenn McDowell
(Committee member/Membre du comité)

Dr. Colin Farquharson
(External Examiner/Examinateur externe)

Dr. Gennady Chitov
(Internal Examiner/Examinateur interne)

Approved for the Faculty of Graduate Studies
Approuvé pour la Faculté des études supérieures
Dr. David Lesbarrères
Monsieur David Lesbarrères
Dean, Faculty of Graduate Studies
Doyen, Faculté des études supérieures

ACCESSIBILITY CLAUSE AND PERMISSION TO USE

Abstract

The radio imaging method (RIM) is a cross-hole electromagnetic (EM) method which employs radio frequency EM waves to estimate the electric properties between boreholes. RIM is applied in hard rock mining to find and delineate sulfide mineral deposits. A basic and relatively simple method for imaging and interpreting RIM data is the straight-ray method. However, the strengths and weaknesses of the straight-ray method and other more sophisticated methods have not been studied thoroughly.

In the first part this research, I modelled RIM data using a finite element package, Comsol Multiphysics. To validate the Comsol approach, I compared the Comsol model data with the analytical solution of an electric dipole in a homogeneous whole-space model, and some published analytical solutions and numerical solutions of models with conductive objects. The Comsol generated data are consistent with the analytical and the published results.

Secondly, I used Comsol synthetic data to assess the effectiveness of the straight-ray method for interpreting RIM data and to study the characteristics of the radio-frequency EM fields. I studied four sets of models with conductive objects embedded in resistive environments, which resemble ore deposits in mining settings. The experiments show that the characteristics of the EM fields mainly depend on the wavelength. Longer wavelengths are associated with lower frequencies. In this condition, EM induction is strong. Shorter wavelengths are associated with higher frequencies. In this condition, the scattering effects of EM waves dominate. In the radio-frequency range, I concluded that the straight-ray method cannot always provide high quality imaging results for RIM data.

To account for the scattering effects, I adopted the contrast source inversion (CSI) method, which was originally developed for microwave tomography in medical imaging, to invert the

RIM data. The CSI method was tested with Comsol synthetic data and field data. The synthetic studies show that the CSI method provides images with more accurate locations and shapes of the conductive objects when compared with the straight-ray method. The case studies show that CSI imaging results are more consistent for data collected at different frequencies and are easier to interpret geologically.

Keywords

Forward modelling, Finite-element method (FEM), Comsol, Cross-hole, Radio-imaging method (RIM), Electromagnetic, SIRT, Back scattering inversion, Contrast source inversion (CSI), TE, 2D inversion

Co-Authorship Statement

This manuscript is composed of six chapters of which four (Chapters 2 to 5) are research papers. Chapter 2 has been published in *Computers and Geosciences*. Chapter 3 has been published in *Geophysical Prospecting*. Chapter 4 has been accepted for publication in *Journal of Applied Geophysics* and Chapter 5 is going to be submitted to the *Journal of Applied Geophysics* as well.

All four papers are co-authored with Dr. Richard S. Smith. My supervisor, Dr. Smith put together the original research proposal, and guided the research by his support and advice. In chapters 2 to 5, where the text is from papers with multiple authors, the pronoun “we”, has been used following standard practise for scientific papers, but in the Abstract, Introduction and Conclusion of this thesis, the pronoun “I” is used to reflect the fact that the opinions are my own and are a drawn from my PhD research.

Acknowledgments

I express my gratitude to my supervisor Dr. Richard Smith. He provided me suggestions and support on this research project, shared with me his experiences and encouraged me on trying every possibility in the research.

I would like to thank my committee members: Glenn McDowell (Vale) and Dr. Ralf Meyer (Laurentian) for their advice on the research. I would also like to thank other geophysicist from Vale: Sean Dickie, Krystal O'Neill and Kevin Fenlon. They expressed great interests on the research and provided the case history data and the straight-ray imaging sections.

Special thanks to Dr. Peter Fullagar. He helped me run the ImageWin program. He showed great interest in the research and provided suggestions.

Thanks to Mr. Bob Lo, for encouragement to work on this project, and to apply for scholarships, as well as his help on adapting to life in Canada.

The radio-imaging research is part of the Industrial Research Chair (IRC) project which is funded by the Natural Sciences and Engineering Research Council of Canada (NSERC), Vale, KGHM International, Sudbury Integrated Nickel Operations A Glencore Company, Wallbridge Mining and the Centre for Excellence in Mining Innovation (CEMI). I express my acknowledgments to the sponsors.

Thanks for the scholarships from the Goodman School of Mines (GSM) and Canadian Exploration Geophysical Society (KEGS), and the travel grant from the Society of Exploration Geophysicists (SEG).

Thanks to my fellow graduate students in the Harquail School of Earth Sciences, particularly Christoph Schaub, Tomas Naprstek, Omid Mahmoodi, Frederic Gaucher, Nikolas Gazo and Yujian Wang etc.

I express my gratitude and love to my families and friends for their trust and support.

Table of Contents

List of Tables

List of Figures

Chapter 1

1 Introduction

1.1 Motivation and thesis arrangement

The radio imaging method (RIM), also known as radio-frequency electromagnetic (EM) tomography, is a cross-hole geophysical method, which employs radio-frequency (typically 0.1 MHz to 10 MHz) EM waves to image the distribution of electric properties between boreholes. RIM has been applied to prediction of coal-seam hazards (Hill, 1984), delineation of ore bodies (Thomson and Hinde, 1993; Zhou et al., 1998; Mutton, 2000) and site selection for underground disposal of nuclear waste (Korpisalo and Heikkinen, 2014).

When there are two vertical or sub vertical boreholes, if the lithologic information associated with each of the two boreholes are complicated, or the geology could change significantly between the boreholes, it is difficult to interpret the geologic structure between the boreholes. In this case, an image showing the spatial distribution of electric properties in the borehole section would be helpful to interpret the geology. To acquire such an image, cross-hole EM data are required. The data are collected with one antenna lowered into one borehole that can be used for transmitting EM waves, and an antenna into another borehole that can be used to receive the EM signal. The transmitter and the receiver are relocated to measure data at a multiplicity of different locations. The measured data are affected by the distribution of the electrical properties of materials between boreholes, which are the information to be inferred from the data. More details about the geometric configuration of these types of tomographic experiments are described in Section 2.2.

The idea of RIM is similar to X-ray computerized tomography (CT) used in medical imaging (Dines and Lytle, 1979; Jackson and Tweeton, 1994). The straight-ray method is commonly used in CT to generate a section image. In the straight-ray imaging frame work, the EM

waves are assumed to be propagating from the transmitter to the receiver along a straight-ray path. The electric properties of the media affect the attenuation rate and the speed that the EM rays pass through the media. By discretizing the borehole section into a grid, it is possible to build linear equations that describe the relationships between the total attenuations (or the travel times) of the rays and the attenuation rates (or the phase coefficients) of the cells in the grid. By solving the equations, the electric properties for all the cells are inferred and used to plot the section image. The details about the straight-ray method and algorithms are introduced in Section 3.2 and 3.3.

The straight-ray imaging method is the primary method for interpreting RIM data in the mining exploration community (Steven et al., 2000; McDowell et al., 2007). The reconstructed images sometimes are helpful to interpret the geologic structure, but sometimes are misleading, and make interpretation even more difficult, leading to a question whether the straight-ray method is suitable for RIM data. This thesis starts with an attempt to study the EM fields and to determine how well the straight-ray method is applied for interpreting RIM data. In Chapter 2, I will introduce a finite-element modelling tool Comsol Multiphysics (Li and Smith, 2015). To model the radio-frequency EM fields, I used the RF module. Comsol provides a user interface, with which I can build a 3D model with simple geometries and mesh the model with tetrahedrons. Before I make use of this tool, I compare the Comsol modelling results with analytical solutions of dipole source in a homogeneous whole-space model, and other published analytic and numerical solutions of more complicated models. These comparison studies show the Comsol method is accurate when the discretization is appropriate and are documented in Chapter 2. The modelling studies in this thesis are for a RIM instrument with an electric antenna source and an electric antenna receiver. EM fields at a set of discrete frequencies are transmitted from the source and measured by the receiver. The measured data are then compared with a reference signal from the source, and then

decomposed to an amplitude component and a phase shift. One field device used to measure this type of data is the FARA system (Stevens et al., 2000; McDowell et al., 2007), which is often used in Sudbury. The antennae lengths for the FARA system are 20 or 40 m. For simplicity, the source antennae are treated as electric dipoles in this study. The antennae are insulated from the material in the borehole, and because it is the radiated fields that are utilized, electrical connection between the source and the rocks are not required. Typical frequencies for the FARA system are 312.5, 625, 1250 and 2500 kHz.

With Comsol Multiphysics, I simulate the data for synthetic models, and use that to test the straight-ray method. Modelling studies on RIM are rarely found in the literature and the behaviour of the EM fields in the radio-frequency range is not well explained. Yu et al. (1998) carried out synthetic studies using finite-difference modelling of perfectly conductive models and their results show how the imaging results vary by dissipation number *D*. However, they did not investigate the detailed behaviour of the EM fields and its interaction with the model. In Chapter 3, I document modelling experiments and imaging studies using the straight-ray method. The studies start with similar models as those in Yu et al. (1998). I build models with rectangular prismatic conductors in models of different background conductivities, and excite these with sources of different frequencies. In the thesis, I mostly focus on the conductivity contrast, because the conductivity contrast is dominant in the mining environment, and currently there is not much information about the permittivity of the rocks available. In these studies, I used a relative permittivity value of 6 for the whole model to correspond with the permittivity value commonly used in Sudbury (Fullagar and Livelybrooks, 1994). I also study a few experiments which are of interest to the mining exploration community: 1) models with L-shaped conductors; 2) imaging with and without a reciprocal data set; 3) models with conductive zones of different lengths extended into the borehole plane from one borehole. In these cases, the imaging results are inadequate. To

make my arguments more convincing, I investigate the physical phenomena for each model by studying the spatial pattern of the excited EM fields. My findings from these experiments are that the straight-ray imaging method cannot provide high quality imaging results for RIM data, because the dominant effects are the EM induction in lower frequencies (< 1 MHz) and EM diffraction in higher frequencies (> 1 MHz). The straight ray method is not able to model either of these phenomena.

The findings of Chapter 3 lead to a further question: is there another method which is better for the RIM data? From the modelling studies, I found that compared with higher-frequency EM methods, such as ground penetrating radar which uses the frequency range from 10 MHz to 1 GHz (Davis and Annan, 1989), the radio-frequency EM waves have lower frequencies and longer wavelengths. Hence, it is more appropriate to describe the radio-frequency EM problem as a back scattering problem, rather than a ray propagation problem.

Inversion methods have been developed for the EM back scattering problem (Devaney, 1984; Joachimowicz et al., 1991; van den Berg and Kleinman, 1997; Mojabi and LoVetri, 2009). These methods were developed in the 1990s and recently applied to microwave tomography in medical imaging for tumour diagnosis (Joachimowicz et al., 1991; Catapano et al., 2009). These methods are based on forward modelling the EM fields using the moment method (Gibson, 2014). The relation between model parameters and the modelled data is highly nonlinear. There are currently two categories of back scattering inversion schemes. One category is based on the Gauss-Newton frame work: at each iteration, forward modelling is used to calculate the misfit between the measured data and the fitted data; and the Jacobian matrix is derived for modifying the model for the next iteration. The algorithm iterates until the data misfit is less than a predetermined threshold, and the latest model is the final result (Joachimowicz et al., 1991; Mojabi and LoVetri, 2009; Mojabi et al., 2011). Another

category of back scattering inversion is based on the contrast source inversion (CSI) approach. By defining a contrast source to be the product of the object profile and the electric field, a cost function is built that is the sum of two quadratic functions, which is easy to minimize. A full forward model is not required at each iteration, so it is computationally faster than the Gauss-Newton scheme (van den Berg and Kleinman, 1997; van den Berg et al., 1999; Abubakar, et al., 2002).

In Chapter 4, I implement the contrast source inversion method for 2D interpretation of RIM data and demonstrate its effectiveness for 3D synthetic data calculated with Comsol Multiphysics. Specifically, I study a) data from a prismatic perfect conductor model, b) the same data with noise, c) the same data, but with transmitters only in a single borehole, and d) the data from a model with an L-shaped perfect conductor.

In Chapter 5, I apply the CSI method to the synthetic data of a more complex model, and real data acquired near Sudbury, Ontario. The synthetic model has a perfect conductor and a moderate conductor embedded in a layered background, which represent a more realistic mining setting. The inversion results are encouraging and helpful for the interpretation of the results of the real data. For the real data, I apply some pre-processing to the data so that the data is consistent with the assumption of my implementation of CSI. After that, I implement the CSI inversion and compare the CSI inversion results with the straight-ray imaging results to evaluate the effectiveness of the CSI method.

In Chapter 6, I will conclude the findings of the studies, and present suggestions for future research.

1.2 References

Abubakar, A., van den Berg, P.M. and Mallorqui, J.J., 2002. Imaging of biomedical data using a multiplicative regularized contrast source inversion method. *IEEE Transactions on Microwave Theory and Techniques*, **50**(7), 1761-1771. doi: 10.1109/TMTT.2002.800427.

Catapano, I., Di Donato, L., Crocco, L., Bucci, O. M., Morabito, A. F., Isernia, T. and Massa, R., 2009. On quantitative microwave tomography of female breast. *Progress in Electromagnetics Research*, **97**, 75-93. doi: 10.2528/PIER09080604.

Davis, J. L. and Annan, A. P., 1989. Ground-penetrating radar for high-resolution mapping of soil and rock stratigraphy. *Geophysical prospecting*, **37**(5), 531-551. doi: 10.1111/j.1365-2478.1989.tb02221.x.

Devaney, A.J., 1984. Geophysical diffraction tomography. IEEE Transactions on Geoscience and Remote Sensing. GE-22(1), 3-13. doi: 10.1109/TGRS.1984.350573.

Dines, K.A., Lytle, R.J., 1979. Computerized geophysical tomography. *Proceedings of the IEEE*, **67**(7), 1065-1073. doi:10.1109/PROC.1979.11390.

Fullagar, P. K., and Livelybrooks, D. 1994. Trial of tunnel radar for cavity and ore detection in the Sudbury mining camp, Ontario. Extended Abstract, In *Fifth International Conference on Ground Penetrating Radar*. European Association of Geoscientists and Engineers.

Gibson, W. C., 2014. *The method of moments in electromagnetics*. CRC press. doi: 10.1080/001075109030 73302.

Hill, D., 1984. Radio propagation in a coal seam and the inverse problem. *Journal of Research of the National Bureau of Standards*, **89**(5), 385-394. doi: 10.6028/jres.089.022.

Jackson, M.J., Tweeton, D.R., 1994. *MIGRATOM—Geophysical tomography using wavefront migration and fuzzy constraints*. Report of Investigations RI9497, Department of Interior, US Bureau of Mines, Minneapolis, MN, USA, 41 pp.

Joachimowicz, N., Pichot, C. and Hugonin, J. P., 1991. Inverse scattering: An iterative numerical method for electromagnetic imaging. *IEEE Transactions on Antennas and Propagation*, **39**(12), 1742-1753. doi: 10.1109/8.121595.

Korpisalo, A., Heikkinen, E., 2014. Radiowave imaging research (RIM) for determining the electrical conductivity of the rock in borehole section OL-KR4-OL-KR10 at Olkiluoto, Finland. Exploration Geophysics. doi: 10.1071/EG13057.

Korpisalo A. L. 2016. *Electromagnetic Geotomographic Research on Attenuating Material Using the Middle Radio Frequency Band*. PhD thesis, University of Helsinki, Finland.

Li, Y. and Smith, R. S., 2015. Forward modeling of radio imaging (RIM) data with the Comsol RF module. *Computers & Geosciences*, **85**, 60-67. doi: 10.1016/j.cageo. 2015.08.012.

McDowell G. M., Stewart R. and Monteiro R. N. 2007. In-mine Exploration and Delineation Using an Integrated Approach. *Proceedings of Exploration*, **07**, 571-589.

Mojabi, P. and LoVetri, J., 2009. Microwave biomedical imaging using the multiplicative regularized Gauss-Newton inversion. *IEEE Transactions on Antennas and Wireless Propagation Letters*, **8**, 645-648. doi: 10.1109/LAWP.2009. 2023602.

Mojabi, P., LoVetri, J. and Shafai, L., 2011. A multiplicative regularized Gauss–Newton inversion for shape and location reconstruction. *IEEE Transactions on Antennas and Propagation*, **59**(12), 4790-4802. doi: 10.1109/TAP. 2011.2165487.

Mutton, A.J., 2000. The application of geophysics during evaluation of the Century zinc deposit. *Geophysics*, **65**(6), 1946-1960. doi: 10.1190/1.1444878.

Stevens K., Watts A. and Redko G. 2000. In-mine applications of the radio-wave method in the Sudbury igneous complex. *In 2000 SEG Annual Meeting. Expanded Abstracts*, 1130-1133. doi: 10.1190/1.1815587.

Thomson, S., Hinde, S., 1993. Bringing geophysics into the mine: radio attenuation imaging and mine geology. *Exploration Geophysics*, **24**(3-4), 805-810. doi: 10.1071/EG993805.

van den Berg P.M. and Kleinman, R.E., 1997. A contrast source inversion method. *Inverse Problems*, **13**(6), 1607-1620. doi: 10.1088/0266-5611/13/6/013.

van den Berg, P.M., Van Broekhoven, A.L. and Abubakar, A., 1999. Extended contrast source inversion. *Inverse Problems*, **15**(5), 1325 - 1344.

Yu, L., Chouteau, M., Boerner, D.E., 1998. On the imaging of radio-frequency electromagnetic data for cross-borehole mineral exploration. *Geophysical Journal International*, **135**(2), 523-541. doi: 10.1046/j.1365-246X.1998.00655.x.

Zhou, B., Fullagar, P.K., Fallon, G.N., 1998. Radio frequency tomography trial at Mt Isa Mine. *Exploration Geophysics*, **29**(3-4), 675-679. doi: 10.1071/EG998675.

Chapter 2

2 Forward modeling of radio imaging (RIM) data with the Comsol RF module[1]

2.1 Abstract

The radio imaging method (RIM) is an electromagnetic (EM) tomographic method, which can be applied to image the electrical properties (principally the conductivity) in the plane defined by two boreholes. RIM employs the EM waves at radio frequencies between 100 kHz and 10 MHz, and the manner that these waves propagate around subsurface ore bodies has not been studied thoroughly. We studied the wave propagation using the finite element modeling (FEM) algorithm as implemented in the Comsol RF module. An appropriate element size is quantified by comparing the Comsol modeling results of 6 types of element sizes at 4 frequencies with the analytical solution in the homogeneous whole space. The FEM model data with 5 elements per wavelength have errors less than 5%; 7 to 8 elements per wavelength provide the errors around 1%; when there are 10 elements per wavelength, the errors are less than 1%. Comparison studies for more complicated models with anomalous conductivity structures show that the Comsol modeling results are consistent with results derived from analytical solutions, finite-difference time-domain methods and integral equations. To illustrate the flexibility of the Comsol method for RIM modeling, we provide an example with two moderately conductive bodies between boreholes. Receiver profiles and a relative variation map show that when the conductive bodies are two wavelengths away from the source, the EM wave attenuation and reflection by the conductive bodies can be observed. The amplitude tomography of the model data reveals that with the simultaneous iterative reconstruction technique, the location of the conductive anomalies can be reconstructed successfully, although, some limitations exist such as low resolution, incorrect

[1] Paper published in *Computers and Geosciences*. The abstract, content, conclusion and references of the original manuscript are included in this chapter.

conductivity estimation, and some artifacts. From our work, we conclude that Comsol modeling is helpful to study radio wave propagation and imaging methods.

2.2 Introduction

The radio imaging method (RIM), also known as radio-frequency tomography, is a cross-hole geophysical method, which employs radio-frequency electromagnetic (EM) waves to image the distribution of electric properties between boreholes. RIM can be applied to prediction of coal-seam hazards (Hill, 1984), delineation of ore bodies (Thomson and Hinde, 1993; Zhou et al., 1998; Mutton, 2000) and site selection for underground disposal of nuclear waste (Korpisalo and Heikkinen, 2014). As shown in Figure 2-1, in a RIM survey, we put a transmitter in one borehole (BH_1), and a receiver in another borehole (BH_2) and move each to a multiplicity of positions where the EM field is measured. If there is material between the boreholes that is more conductive than the background, the EM fields attenuate faster and travel more slowly. This situation results in a measured response (dotted line on the right of Figure 2-1) which is less than the response of the background only (depicted with the dashed line). In the case when the material is extremely conductive, the measured data can drop below the noise level (as depicted with the solid line on the right of Figure 2-1). The situation in Figure 2-1 shows the simple case of straight rays propagating directly from the transmitter to the receiver and those that strike the anomalous body being completely absorbed (attenuated). As discussed below, the situation is, in reality, more complex.

Figure 2-1 shows one transmitter and a multiplicity of receivers (with rays going from the transmitter to each receiver). A full tomographic survey comprises many transmitter positions at multiple depths down the hole. This full survey data is used to reconstruct an image on the cross-hole plane.

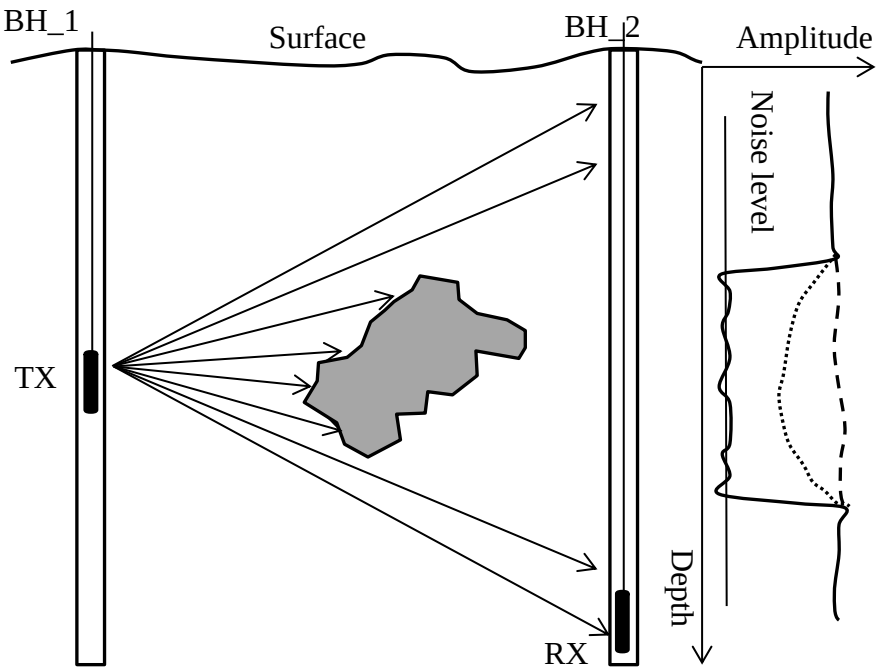

Figure 2-1: Diagram of Radio Imaging Method. This shows one transmitter (TX) position in the left hole (BH_1). The receiver is lowered down the right hole (BH_2). Three amplitude profiles are shown schematically in the right panel: the dashed line is when there is no body present between holes and the dotted and solid lines show the situation when the grey body between holes results in partial and complete attenuation of the signal.

The mathematical foundation of image reconstruction is similar to X-ray computerized aided tomography (CAT) in medical imaging (Jackson and Tweeton, 1994). The idea of tomography has been successfully applied to explore the earth, with seismic waves (Dines and Lytle, 1979) or high-frequency (typically 10 – 1500 MHz) EM waves (Holliger et al., 2001). In mining exploration for sulphide minerals in a hard rock environment, we focus more on the EM waves, because the EM data can be used to infer the electric properties of minerals and the electrical properties of ore bodies are normally strongly anomalous. However, high-frequency EM waves typically attenuate quickly in the subsurface, which results in very short propagation distances (usually meters to tens of meters). Boreholes in mining exploration are usually on the order of hundreds of meters apart. Hence, it is necessary to lower the frequency to the medium frequency range (0.1 – 10 MHz) in order to

obtain sufficient signal. However, the EM fields in this frequency range do not behave as simply as X-rays in CAT scans (as depicted on Figure 2-1). In the medium-frequency range, the waves can be refracted and reflected, and as the frequency lowers, currents can be induced in the anomalous body and reradiated. A modeling tool capable of simulating all of these situations is required to better understand the RIM method. Wilkinson (2005) argued that at the medium-frequency range, the modeling tool needs to be able to account for changes in conductivity and dielectric permittivity. Additionally, Naprstek (2014) found that magnetic permeability also had an impact on the response, although this was easily confused with the impact of changes in conductivity. Hence, it is necessary to solve the full Maxwell equations and not ignore either conductivity effects or permittivity effects. Solutions that assume propagating rays generally solve the wave equation and assume the conductivity is zero, while other solutions might solve the diffusion equation and assume the permittivity is zero. A method that solves the full Maxwell equations will allow us to better understand the RIM method and hence better utilize the data.

A number of attempts have been made to model RIM data using a variety of methods. Monaghan (2007) built scaled physical models and used a corresponding higher-frequency EM wave to quantify the EM wave propagation in coal seams. The disadvantages of the scaled models are that the effects of the model boundaries were not considered; measurements are limited on the surface of the models; and model making is expensive and time-consuming. Alternatives are numerical modeling methods. Johnson (1997) employed the finite-difference time-domain method (FDTD) to model the RIM data. He investigated the interaction of the fields from a magnetic dipole with perfect electric conductors. His modeling revealed diffraction of the EM wave, which may result in artifacts on ray-based images. His studies were restricted to highly conductive plate-like models. Other models such as layered models, spherical models and weakly conductive bodies were not studied.

Another widely used method is the finite-element method (FEM), which is not restricted to square network discretization and enables the use of tetrahedral elements, as these are more efficient for simulating complex 3-D models (Bondeson et al., 2005). Over the last decades, numerical modeling algorithms are now being built into commercial or open-source software. Comsol Multiphysics is one of the commercial numerical modeling software packages that is based on the FEM. Comsol Multiphysics has been applied to model geophysical fields, such as gravitational, magnetic, electric and electromagnetic fields (Butler and Sinha, 2012; Park et al., 2010). In this paper, we apply the Comsol Multiphysics package and specifically the RF module to model RIM data.

We began by comparing the Comsol package with the analytical solution for a whole space. This allowed us to evaluate the modeling precision and define some rules for defining the element sizes in our models. Then, we built confidence in the Comsol package by comparing the results with published results from other numerical algorithms. Finally, we showed how it is possible to generate a response from a realistic field situation and how this data can be used to better understand the propagation of EM fields and tomographic imaging methods.

2.3 Comsol Modelling

The Comsol Multiphysics package has graphic user interfaces (GUIs), which make the implementation of the FEM much easier. Complex geophysical models can be developed in this environment with simple geometries such as blocks, spheres and cylinders and the meshes or grids required for representing the fields can be generated easily. In order to simulate the EM data in the medium frequency range, we used the RF module available for the Comsol platform, as this module solves the full Maxwell's equations. With the RF module, we can assign the necessary physical properties for the full EM solution, including conductivity, dielectric permittivity and magnetic permeability. The EM field sources can be

from an electric dipole, magnetic dipole, electric current or magnetic current, etc. For comparison with the analytical solutions, we used the frequency-domain electric dipole source. The configurations of dipole source include selecting the position, orientation, dipole moment and frequency.

To simulate EM fields in unbounded models, we configured perfectly matched layers (PMLs) on the edges of the models to absorb the outgoing EM waves, with the thickness defined in accordance with the users' guide (Multiphysics, 2012). The domains of PMLs are discretized with swept meshes, which start along the grids on the surface between the inner domain and the PMLs and then mesh along the direction perpendicular to the surface, which generates prismatic elements. The swept meshes are discretized with 5 layers by default (Figure 2-2b). In the inner domains, we use free tetrahedral elements to discretize the models. The user can control the sizes of the elements in every subdomain, which is useful because we often want to use finer elements in regions that we are more interested in.

After building and meshing the models, Comsol generates the partial differential equations and solves the equations on the mesh. We choose the biconjugate gradient stabilized iterative method (BiCGStab), which is time and memory efficient for the vector field (Multiphysics, 2012).

2.4 Tests of the Comsol software

In this section we determine the optimal element size for sampling a whole space. For non-whole-space models, we compare the Comsol results with published data of analytical solutions and other numerical methods.

2.4.1 Comparison with homogeneous models to determine optimal element size.

Ward and Hohmann (1988) derived the analytical solution of an electric dipole in a homogeneous whole space for low frequency EM, in which the dielectric permittivity was ignored. To calculate the EM fields in the medium frequency range, the impact of dielectric permittivity should be considered. The *x*-component and *z*-component of electric field at P(*x*, *y*, *z*) generated by a *z*-directed dipole source with dipole moment Ids at the origin of Cartesian coordinates are as follow:

$$\mathbf{E_x} = \frac{I\,ds}{4\pi(\sigma + i\varepsilon\omega)r^3} \cdot \frac{xz(-k^2r^2 + 3ikr + 3)}{r^2} e^{-ikr} \tag{2-1}$$

$$\mathbf{E_z} = \frac{I\,ds}{4\pi(\sigma + i\varepsilon\omega)r^3} \left(\frac{z^2(-k^2r^2 + 3ikr + 3)}{r^2} + k^2r^2 - ikr - 1 \right) e^{-ikr} \tag{2-2}$$

where, I is the transmitting current; ds is the length of the dipole; σ is the conductivity; ε is the dielectric permittivity, $\varepsilon = \varepsilon_r \cdot \varepsilon_0$, in which, ε_r is the relative permittivity and ε_0 the free space permittivity; ω is the angular frequency, $\omega = 2\pi f$, in which f is the frequency; r is the distance from the dipole to P; and k is the wave number, $k^2 = \mu\varepsilon\omega^2 - i\mu\sigma\omega$, in which, μ is the magnetic permeability, $\mu = \mu_r \cdot \mu_0$, where, μ_r is the relative permeability and μ_0 the free space permittivity. The *y*-component is always 0. We focus on the *z*-component, because, usually, only the *z*-component can be measured in vertical boreholes. These formulae are identical to the equation (2.40) in Ward and Hohmann (1988), except, they removed the terms with ε.

In the Comsol model building environment, we created a homogeneous model with σ = 0.001 S/m, ε_r = 1 and μ_r = 1. The frequencies of the EM source are 312.5, 625, 1250 and 2500 kHz. These are the operating frequencies of the FARA system, which is commonly used in Sudbury, Canada. The wavelength can be calculated by the formula,

$$\lambda = \frac{2\pi}{\beta}\ , \tag{2-3}$$

where, β is the phase coefficient, which can be obtained from equation (1.48) in Ward and Hohmann (1988),

$$\beta = \left\{\frac{\omega^2\mu\varepsilon}{2}\left[\left(1+\frac{\sigma^2}{\varepsilon^2\omega^2}\right)^{1/2}+1\right]\right\}^{1/2}\ . \tag{2-4}$$

Using equation (2-3) and (2-4), the wavelengths of these frequencies are 177, 124, 86 and 59 m respectively. The modeled region is a 400 by 400 by 400 m cube, with its center at the origin. A vertical dipole source is at (x, y, z) = (-50, 0, 0), with the dipole moment 4000 Am. A 50 m-thick PML is configured on the outer surface of the region to absorb the outgoing fields. A 120 m-long receiver traverse is located from (50, 0, -60) to (50, 0, 60). The rectangular prism that includes the source and receiver line with a strike extent of 50m (25 m into and out of the section) is deemed our "region of interest" (as shown in Figure 2-2a). In our test studies, we meshed this region with 6 types of different elements sizes, which are shown in Table 2-1. The first four element sizes (with maximum edge lengths of 35, 25, 17, and 12 m) are designed to meet a criterion of 5 elements per wavelength for the four frequencies (177, 124, 86 and 59 m). The Mesh Type 5 and 6 are added to study the modeling errors obtained by using even smaller element sizes. For comparison, we want the element sizes of each type to fall within a fixed range, so that adjacent mesh types do not have overlap (Table 2-1). From the edge of the region of interest to the PMLs, the element sizes are free to increase to as large as 60m, which can reduce the number of elements, and hence save computation time. Figure 2-2b illustrates the Mesh Type 4.

The magnitudes of the z-component model data for mesh type 2, 4 and 6 at 2.5 MHz along the receiver line are plotted in Figure 2-3 with open circle, open square and solid circle

symbols respectively. The figure shows that as the element size decreases, the data spacing along the receiver line decreases. The modeling errors also decrease, as smaller discrepancies between modeling data and the analytical solution (solid line) can be observed.

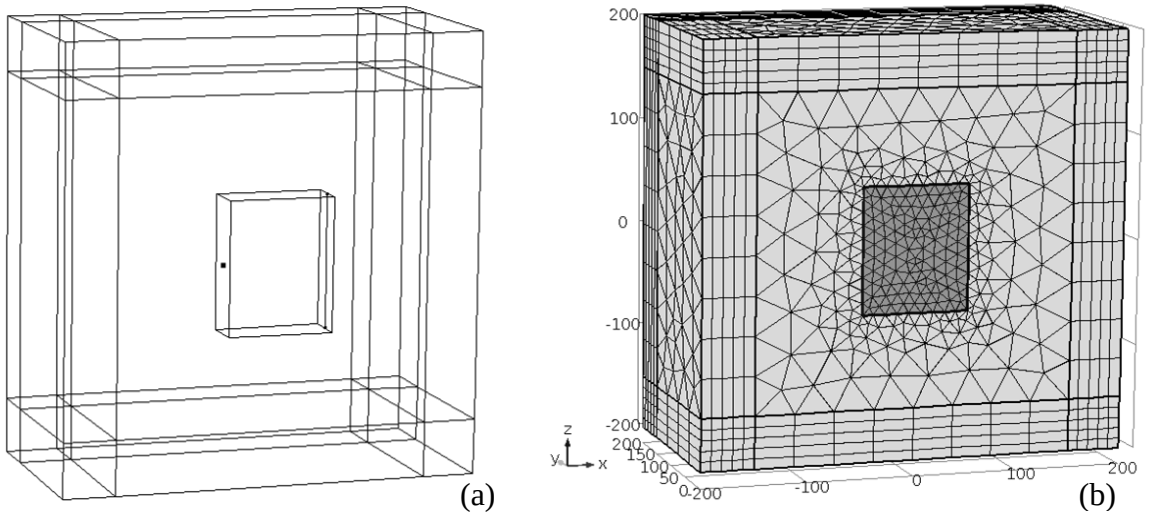

Figure 2-2. (a) Transparent view of the homogeneous model without the front half. The innermost prism including the transmitter (the dot on the left) and receiver line (the vertical line on the right) is our region of interest. (b) The region of interest (dark grey area of (b)) is meshed with Mesh Type 4. Element sizes between the region of interest and the PML can increase to 60 m. The PML is discretized with 5 layer swept meshes. (The front half is removed and the rest is meshed along the XZ-plane for illustration)

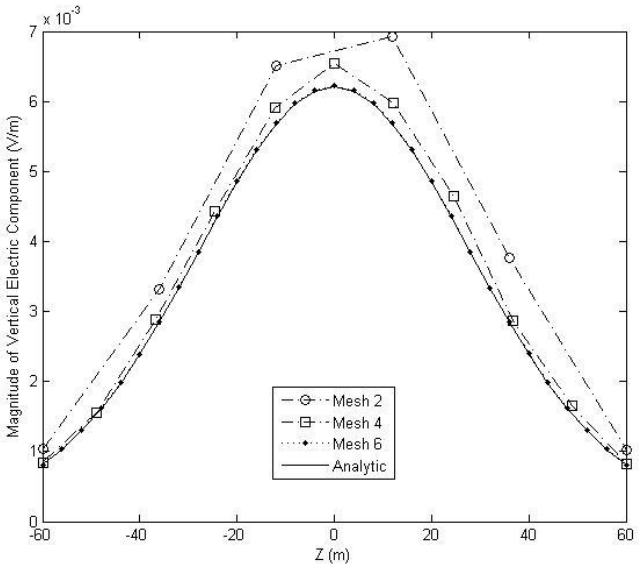

Figure 2-3. Receiver profiles of 2.5 MHz data for three different mesh sizes and the analytic solution. The mesh sizes are shown in Table 2-1.

Table 2-1. Mesh sizes and modeling error, memory usage and run time

Mesh type	Element edge length	Modeling error (RMS, %)				Degrees of freedom	Memory usage (GB)	Run time (s)
		312.5k	625k	1.25M	2.5M			
1	25-35 m	**4.30**	16.40	43.00	266.87	186,084	3.11	64
2	17-25 m	*3.38*	**4.37**	7.05	23.98	188,846	3.16	66
3	12-17 m	0.84	*0.76*	**4.95**	13.28	209,284	3.26	75
4	8-12 m	0.56	0.76	*1.38*	**4.92**	252,842	3.53	87
5	6-8 m	0.24	0.27	0.45	*1.13*	373,052	4.51	130
6	3-6 m	0.10	0.17	0.24	0.73	574,756	5.73	186

We calculated the Root Mean Square (RMS) of the modeling errors along the receiver line for the six mesh types at all frequencies. The results are listed in Table 2-1. We can see from Table 2-1 that the mesh types that have 5 elements per wavelength (bolded numbers) can provide a modeling precision with the errors within 5%. As the sizes become smaller to 7 to 8 elements per wavelength, the modeling errors converge to around 1% (italic numbers), except for the 312.5 kHz case. The reason for this is that at low frequency, the wavelength is so large that the receiver line is relatively close to the source. The near-field effect makes the EM fields more complicated. As the sizes decrease to 10 elements per wavelength, the modeling data have errors less than 1% for all four frequencies (underlined numbers).

However, greater precision comes with longer computational time and larger memory requirements. As the discretization is finer, the degrees of freedom of the partial differential equation are higher, so that it takes more time and larger memory to find a solution. The memory usage and the run times listed in Table 2-1 are obtained in an 8-core computer with a clock speed of 2.65 GHz. It can be observed from Table 2-1 that the memory usages and run times are approximately proportional to the degrees of freedom. However, the algorithm takes more time when the model is more complex. In the heterogeneous modeling example we present in the next section, the degrees of freedom is around 7 million, while the memory

usage is 86.7 GB and the run time is 4130 s (69 minutes) for 1 transmitter location. This run time is almost twice as large as would have been predicted from Table 2-1.

Therefore, to maintain reasonable modeling precision with affordable computational time and memory, we recommend discretization no less than 7 elements per wavelength within the region of interest, while outside of the region of interest, the element sizes could increase to be much larger to save memory and computation time.

The optimal mesh sizes have been derived by comparison with a whole-space model. In order to gain confidence that these mesh sizes can be applied more generally, we have calculated the response using Comsol for models that have been published in the literature that contain heterogeneous bodies in a uniform background.

2.4.2 Comparison of Comsol and published results for anomalous models

The Comsol RF module has been compared with the analytical solutions and a FDTD numerical modeling code for a spherical model. The profiles plotted on Figure 2-4 are the solutions of conductive spherical anomalies of differing conductivity in a homogeneous whole space. Two transmitters are at point A (0, 0, 2) and point B (0, 0, 22), with the transmission frequency 1M Hz, and the dipole moment 1 Am. The center of the spherical body is at (50, 0, 0) and its radius is 20 m. The receiver line is from (100, 0, -50) to (100, 0, 50). The physical properties of the background are σ = 0.001S/m, ε_r = 3, μ_r = 1. The geometry of the transmitter points, the sphere and the receiver line is shown on the bottom right of Figure 2-4. All of these parameters are fixed, but the conductivities of the sphere are 0.01, 0.1, 1 S/m, and in the limit that the sphere is defined to be a perfect conductor ($\sigma \to \infty$). The wavelengths and the maximum element edge lengths in the sphere and the background are in the left of Table 2-2. The element sizes are designed to meet at least the $1/5^{th}$ wavelength requirement, except for 1 S/m sphere as the computation time would be too large. The perfect

conductor is simulated with perfectly conductive boundary condition, so the element sizes in the sphere do not matter in this case. In Figure 2-4, the analytical solutions of the spherical models with conductivity 0.01, 0.1, 1 S/m and the FDTD solution of the perfectly conductive sphere are from Yu et al., (1998). We can see that the Comsol modeling results match the analytical solutions very well, especially for models with conductivity of 0.01 and 0.1S/m. The Comsol modeling results show the more conductive the sphere, the higher the data values, such that the largest data profile is the solution of a perfect conductor. Whereas, the FDTD profile is erratic, with some parts being too large and other parts lie between the analytical solutions of 0.1 and 1.0 S/m. Hence, we argue that for this model, the Comsol results are better than the FDTD result.

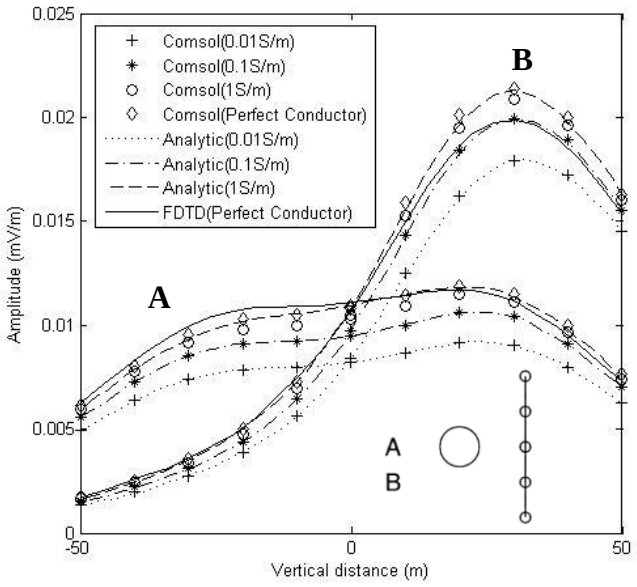

Figure 2-4. Modeling results of spherical models with different conductivities calculated by Comsol Multiphysics, compared with the analytical solutions and the FDTD solution. The conductivities of the sphere and the solution methods are shown in the legend. The results derived by the analytical solution and the FDTD method are from Yu et al., (1998). The geometry is shown as a cross section view in button right of the figure and the five open circles represent the receiver locations (although there are more than 5).

Our second test study compares the FDTD and the integral equation solutions (Xiong and Tripp, 1997) of a cubic model, also published in Yu et al. (1998). Transmitters are at slightly

different location points A (0, 0, 0) and B (0, 0, 30), with the same operating frequency and dipole moment as the previous example. The size of the cube is 24 × 24 × 24 m, with its center at (50, 0, 0). The receiver line is also the same as the previous model and the geometry is depicted on the top left of Figure 2-5. The relative permittivity and the relative permeability are 10 and 1 respectively for the whole model. The background conductivity is 0.001S/m, while the conductivity of the cube is 0.1S/m. The wavelengths and the element sizes are in the right of Table 2-2. In Figure 2-5, the solid line shows the Comsol solution; the asterisks the FDTD solution and the solid line the integral equation solution. The figure shows that the Comsol solutions are comparable with the FDTD solutions and the integral equation solutions. From these two results we conclude that the guidelines we have developed for element sizes yield good results in anomalous regions.

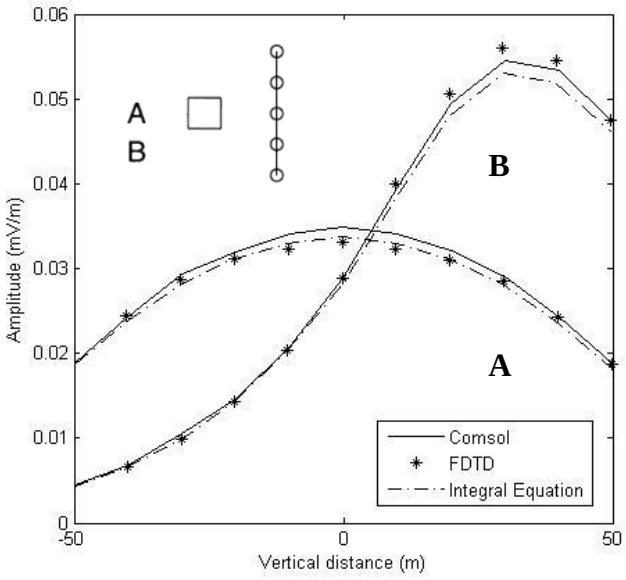

Figure 2-5. Modeling results of a 0.1 S/m cubic model by Comsol Multiphysics (solid line), FDTD (asterisks) and integral equation method (dash-dot line). The data derived using FDTD method and integral equation method are from Yu et al. (1998)). The geometry is shown as a cross section view in the top left of the figure and the five open circles represent the receiver locations (although there are more than 5).

Table 2-2. Wavelengths and element sizes for anomalous models

Spherical model ($\varepsilon_r = 3$, $\mu_r = 1$)			Cubic model ($\varepsilon_r = 10$, $\mu_r = 1$)		
σ (S/m)	λ (m)	Max. Element (m)	σ (S/m)	λ (m)	Max. Element (m)
0.001	92.03	10	0.001	76.68	10
0.01	31.36	4	0.1	9.97	2
0.1	9.99	2			
1	3.16	1			
∞	1/∞	1			

2.5 Modeling Example

Here we provide a demonstration that Comsol can be used to study the EM fields of more realistic scenarios. We also use the modeled data to study the efficacy of a tomographic image reconstruction method in the case when the true model is known. Figure 2-6a is an XZ plane view (at $y = 0$) of the 3D model. The transmitter borehole (TX) is from (0, 0, 100) to (0, 0, 440), with the transmitter spacing 20 m (so there are 18 transmitter locations in total). The transmitter frequency is 2.5 MHz and the dipole moment is 4000 Am. The receivers (RX) are along the line from (-200, 0, 100) to (-200, 0, 440). There are two targets in the model. Target 1 (T1) is a rectangular prism, with its center at (-110, 0, 175). Its cross section on the XZ-plane is a 96 × 32 m rectangle, with a 45 degree dip; the strike length is 96 m in the y-direction, with its center at the XZ-plane. Target 2 (T2) is a 32 m-thick layer dipping at a 55.4 degree angle, starting at (-60, 0, 400), all the way to the left edge of the model near x = -240. Its strike length is 300m, with its center at the XZ-plane. The rectangular prism bounded on the left and right by the TX and RX boreholes, with a strike length of 200m, is the region of interest selected for finer discretization. The size of the whole model is 400 × 400 × 560m, including a 50m-thick PML on the edge of the model (Figure 2-6a).

The model has conductivities of 0.001 S/m for T1 and T2, and 0.0001 S/m elsewhere. Other physical parameters are $\varepsilon_r = 6.5$ and $\mu_r = 1$ for the whole model. The wavelength is 46.96 m in the background, and 42.14 m for T1 and T2. We discretize the model with element sizes of 3 – 5 m in T1 and T2, and 4 – 6 m elsewhere within the region of interest, giving cells that are approximately 1/8th of the wavelength. From the outer surface of the region of interest to the PMLs, the edge length of the element can increase to 20 m. By numerically solving Maxwell's equations, the *x*-, *y*-, and *z*-components of the electric field on the nodes of the elements will be determined. Along the receiver borehole, the node spacing is 4-6 meters, but we can interpolate to get the *z*-component E field response every meter.

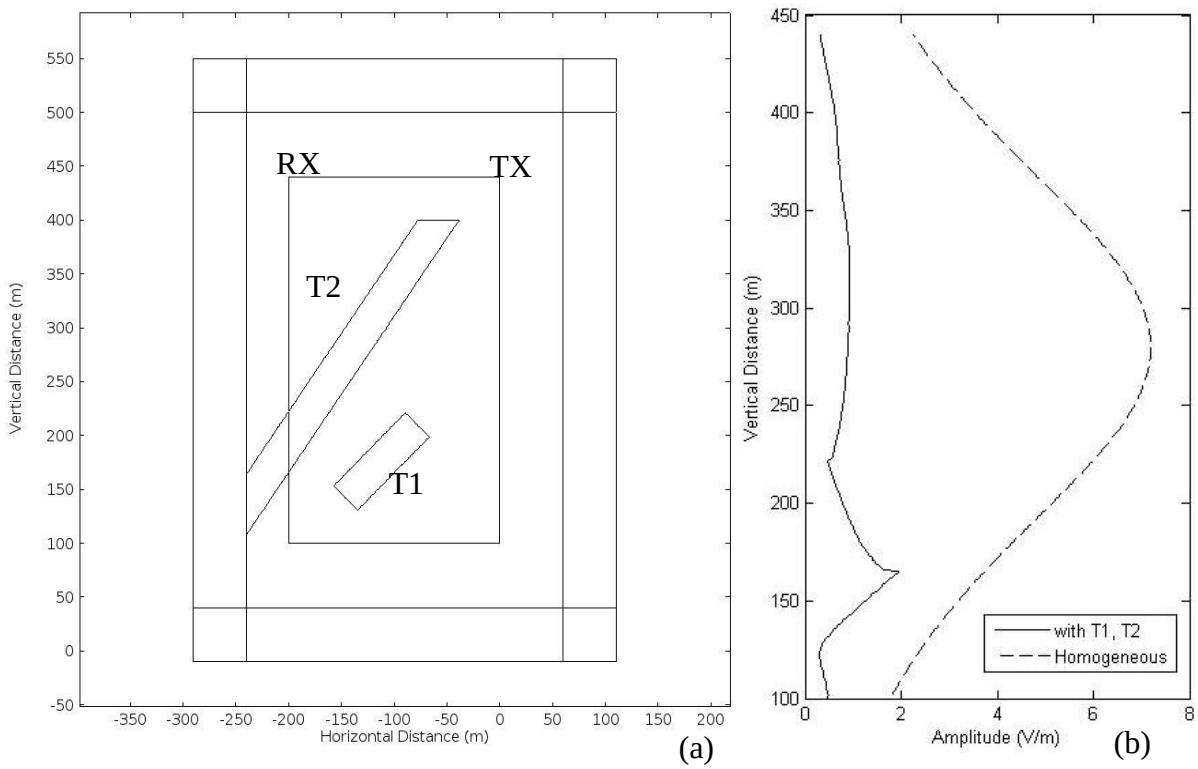

Figure 2-6. (a) XZ-plane view of the synthetic model with two vertical boreholes containing the transmitter (right) and receiver (left). There are two anomalous bodies T1 and T2, centred on the XZ plane with strike lengths of 96 and 300 meters respectively. The inner rectangle is the region of interest, and the PML is between the outer two rectangles. The strike length of the whole model is 400 m. (b) Receiver profiles of transmitter position at *z* = 280 m with (solid) and without anomalies (dashed).

As one example we have plotted the *z*-component amplitude data for the case when the transmitter is at *z* = 280 m (Figure 2-6b). The dashed profile is the data in a homogeneous model with conductivity of 0.0001S/m (and peaks at the same depth as the source – 280 m), while the solid profile is the synthetic data with T1 and T2 inserted into the model. It can be seen from the figure that in the second case receiver data are attenuated by the presence of T1 and T2, with the profile peaking at *z* = 160 m, where a ray from the transmitter would pass through the gap between T1 and T2. The receiver data has its lowest value at *z* = 220 m, which corresponds to the upper edge of the T2, where a ray from the transmitter has the longest passage through T2. The receiver profiles on Figure 2-6b show that for this frequency, straight ray attenuation theory can generally represent the characteristics of the response.

To study the spatial variation of the EM field on the XZ plane for the case when the transmitter is at *z* = 280 m, we exported the *z*-component data from Comsol and calculated the relative variation on the plane. The relative variation is defined as the difference from the homogeneous model data at the corresponding position normalized by the homogeneous model data,

$$V_R = \frac{A_a - A_h}{A_h} \times 100\% \,, \tag{2-5}$$

where, V_R is the relative variation; A_a is the amplitude data with the anomalous models T1 and T2; and A_h is the homogeneous model amplitude data. From the map of the relative variation on the plane (Figure 2-7a), we can see where and how much the field is increased or decreased by the T1 and T2. Warm colors represent an increase, while cool colors depict a decrease. The straight ray attenuation theory can explain the shadow zone within and behind T1 and T2, but does not work well near the edges of the conductive bodies. The shadow, created by T1, has a larger area than would be predicted by the straight-ray model. The

attenuation is strong right behind the conductive bodies, and changes gradually to non-attenuated field, far away from the edges of the objects. There are striped patterns between the source and the conductive bodies, which cannot be interpreted with the straight-ray theory either. One possible explanation is the EM wave is reflected at the surface of the conductive bodies, and is shifted slightly in phase and interferes with source field causing the increased and decreased fields with a wavy pattern. Considering the wavelength of the background is 46.96 m the closest conductive anomaly is almost 100 m away from the source, which is about twice the wavelength. In this case, $|kr|$ = 13.40, which satisfies the condition that $|kr| >> 1$, so the second order term, which is inductive contribution, is small. We infer that the induction phenomenon will only have a minor effect in this case.

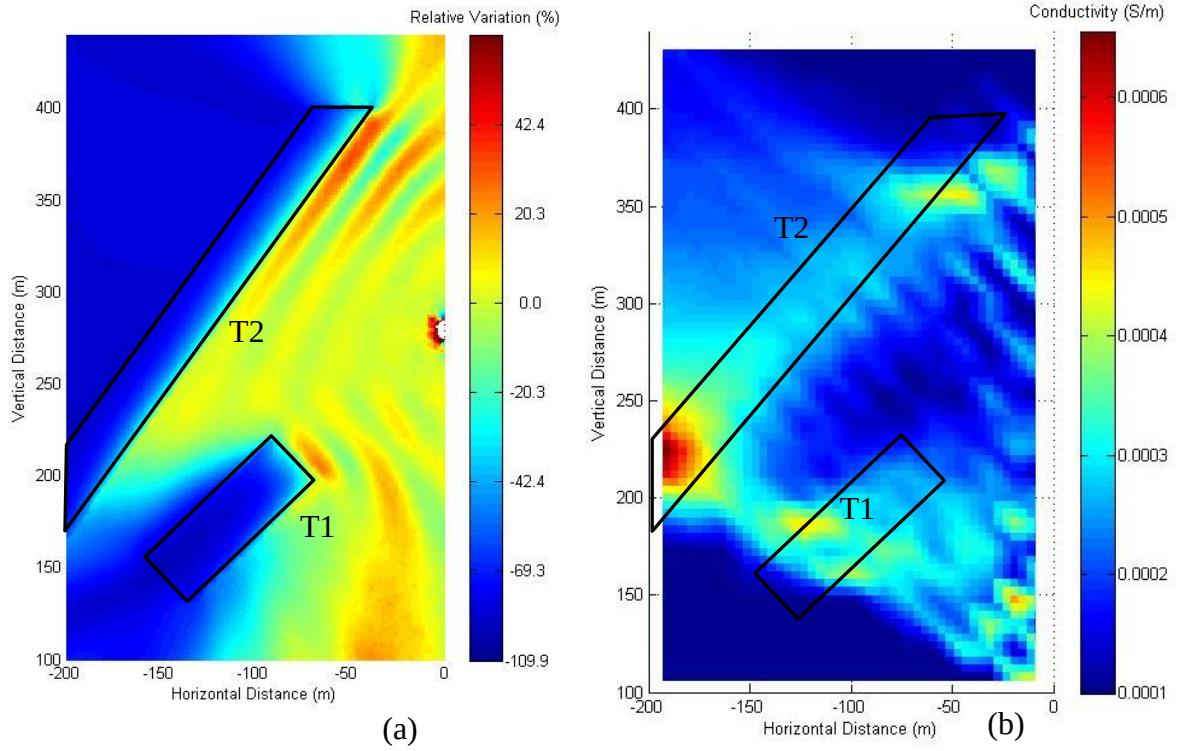

Figure 2-7. (a) Relative variation map (generated using the differences between Comsol data and the data of a homogeneous model) for the case when the transmitter is at *z* = 280 m. (red is increased relative to the homogeneous whole space and blue is decreased) (b) Imaging results of SIRT algorithm. Outlines of T1 and T2 are added for comparison.

To study the imaging methods, we export the receiver data for all the transmitter locations, and input the synthetic data into a tomographic algorithm. Here we give an example of the Simultaneous Iterative Reconstruction Technique (SIRT) algorithm (Jackson and Tweeton, 1994; Pears and Fullagar, 1998). The SIRT algorithm (based on the straight-ray EM propagation model), together with the data pre-processing, has been implemented in the ImageWin program (www.fullagargeophysics.com). Here, we process the data as follow: 1) converting the amplitude data to decibel units by taking the logarithm; 2) radiation pattern correction using an assumed spherical spreading; 3) source strength correction using the source term calculated with the transmitted current. The borehole plane is discretized with a pixel size of 4 × 4 m. The attenuation of a certain ray path is the sum of the attenuations in each pixel the ray passed through. The attenuation in each pixel is the product of the attenuation rate and the distance that the ray traverses in that specific pixel. The distance can be calculated according to the geometry of the borehole plane and the pixel size (assuming a straight ray). We can use these relations to construct a set of equations. By solving the equations, we reconstruct an image of attenuation rate on the borehole plane (Hill, 1984). After that, we transform the attenuation rate to conductivity by rearranging equation (1.49) in Ward and Hohmann (1988),

$$\alpha = \left\{\frac{\omega^2\mu\varepsilon}{2}\left[\left(1+\frac{\sigma^2}{\varepsilon^2\omega^2}\right)^{1/2}-1\right]\right\}^{1/2}, \tag{2-6}$$

where, α is the attenuation rate. Figure 2-7b shows the transformed conductivity data.

We can see that the imaging results of the SIRT algorithm are of acceptable quality, with the locations and the shapes of T1 and T2 being somewhat blurred. There is a good ability to identify the middle of T1, but not the bottom. The location where T2 intersects the receiver line dominates the image. However, the length of T2 is only weakly resolved, and the top is displaced somewhat. The value of the background conductivity seems reasonably resolved,

but the value of the conductivity in the conductive anomalous zones is not successfully recovered. There are some artifacts near the transmitted borehole. Some defects are inherent in the RIM method, which means that the imaging quality could not be improved with any imaging method; for example, the smeared area on the upper-left of the image is due to poor data coverage. We can see that the lower edge of the T2 is better resolved than the upper edge, because the lower edge is closer to the center of the cross-hole section, where more rays are coming from a larger angle range, which gives the lower edge a better data coverage (Jackson and Tweeton, 1994). However, some problems might be due to the ray-based imaging method, for example, a poor ability to distinguish T1 and T2. Figure 2-7a shows that the EM-field propagation does not follow a precise straight ray path. Alternative imaging methods based on a curved-ray model or diffraction tomography (Devaney, 1984; Nekut, 1994), may possibly give better imaging results. However, based on the current observation, we cannot draw strong conclusions. We need to carry out further studies to find out what kinds of imaging methods are appropriate for the RIM data, and the Comsol package can play a role in generating synthetic RIM data where the electric properties are known.

2.6 Conclusions

The ability of the Comsol RF module to simulate RIM data was investigated. By comparing the Comsol modeling results (with 6 types of element sizes at 4 frequencies) with the analytical solution for the homogeneous whole space, we find that the synthetic data generated with 5 elements per wavelength have modeling errors less than 5%; 7 to 8 elements per wavelength yield the errors around 1%; and 10 elements per wavelength give errors less than 1%. The comparison studies for anomalous models show that the Comsol modeling results are consistent with the analytical solutions and the solutions of other numerical modeling methods. Further, the guidelines for element sizes derived from homogeneous whole space models can be applied to inhomogeneous models.

We provide a modeling example with two moderately conductive bodies between boreholes to illustrate the modeling capability of the Comsol package. In the example, we use a receiver profile and the relative variation map to understand the physical phenomena of radio-frequency EM waves. We find that attenuation in the two conductive bodies is apparent in the relative variation maps and that a shadow cast by the transmitter is also apparent; however, this shadow is not as sharp as the ray theory would predict. Some reflections are also apparent between the source and the conductive bodies. The imaging example reveals that with the SIRT algorithm, the location and the shape of the conductive anomalies can be reconstructed somewhat successfully. The imaging results have some problems such as low resolution, incorrect conductivity estimation, and some artifacts. To better understand the imaging algorithms, we need further studies, and the Comsol package can serve as a useful FEM modeling tool for these studies.

2.7 Acknowledgments

The authors express acknowledgments to the Natural Sciences and Engineering Research Council of Canada (NSERC), Vale, KGHM International, Sudbury Integrated Nickel Operations A Glencore Company, Wallbridge Mining and the Centre for Excellence in Mining Innovation for sponsoring the research. We would also like to thank Peter Fullagar for interesting discussions and help in running the ImageWin program.

2.8 References

Bondeson, A., Rylander, T., Ingelström, P., 2005. Computational Electromagnetics. Texts in Applied Mathematics Vol. 51, Springer: New York, 222pp. doi: 10.1007/b136922.

Butler, S.L., Sinha, G., 2012. Forward modeling of applied geophysics methods using Comsol and comparison with analytical and laboratory analog models. Computers & Geosciences 42, 168-176. doi: 10.1016/j.cageo.2011.08.022.

Devaney, A.J., 1984. Geophysical diffraction tomography. IEEE Transactions on Geoscience and Remote Sensing. GE-22(1), 3-13. doi: 10.1109/TGRS.1984.350573.

Dines, K.A., Lytle, R.J., 1979. Computerized geophysical tomography. Proceedings of the IEEE 67(7), 1065-1073. doi:10.1109/PROC.1979.11390.

Hill, D., 1984. Radio propagation in a coal seam and the inverse problem. Journal of Research of the National Bureau of Standards 89(5), 385-394. doi: 10.6028/jres.089.022.

Holliger, K., Musil, M., Maurer, H.R., 2001. Ray-based amplitude tomography for crosshole georadar data: A numerical assessment. Journal of Applied Geophysics 47(3-4), 285-298. doi: 10.1016/S0926-9851(01)00072-6.

Jackson, M.J., Tweeton, D.R., 1994. MIGRATOM—Geophysical tomography using wavefront migration and fuzzy constraints. Report of Investigations RI9497, Department of Interior, US Bureau of Mines, Minneapolis, MN, USA, 41 pp.

Johnson, D.M., 1997. Finite difference time domain modeling of cross-hole electromagnetic survey data. M. Sc. Thesis, University of Utah, Salt Lake City, UT, USA, 89 pp.

Korpisalo, A., Heikkinen, E., 2014. Radiowave imaging research (RIM) for determining the electrical conductivity of the rock in borehole section OL-KR4-OL-KR10 at Olkiluoto, Finland. Exploration Geophysics. doi: 10.1071/EG13057.

Monaghan, W.D., 2007. Experimental studies of electromagnetic signals to enhance radio imaging method (RIM). M. Sc. Thesis. West Virginia University, Morgantown, WV, USA, 115 pp.

COMSOL Multiphysics User Guide, 2012. Version 4.3 a, COMSOL AB, Stockholm, Sweden.

Mutton, A.J., 2000. The application of geophysics during evaluation of the Century zinc deposit. Geophysics 65(6), 1946-1960. doi: 10.1190/1.1444878.

Naprstek, T., 2014. Modelling radio imaging method data using electric dipoles in a homogenous whole space. M. Sc. Thesis, Laurentian University, Sudbury, ON, Canada, 84 pp.

Nekut, A.G., 1994. Electromagnetic ray-trace tomography. Geophysics 59(3), 371-377. doi: 10.1190/1.1443599.

Park, J., Bjørnarå, T.I., Farrelly, B.A., 2010. Absorbing boundary domain for CSEM 3D modelling. In: Excerpt from the Proceedings of the COMSOL Conference 2010, Paris.

Pears, G.A., Fullagar, P.K., 1998. Weighted tomographic imaging of radio frequency data. Exploration Geophysics 29(3-4), 554-559. doi: 10.1071/EG998554.

Thomson, S., Hinde, S., 1993. Bringing geophysics into the mine: radio attenuation imaging and mine geology. Exploration Geophysics 24(3-4), 805-810. doi: 10.1071/EG993805.

Ward, S. H., Hohmann, G. W., 1998. Electromagnetic theory for geophysical applications, In: Nabighian M. N.(Ed.) Electromagnetic Methods in Applied Geophysics Vol. 1, Society of Exploration Geophysicists, pp 131-311. doi: 10.1190/1.9781560802631.ch4.

Wilkinson, P.B., 2005. Cross borehole electromagnetic tomography: scoping study and literature review. Internal Report IR/05/146, British Geological Survey, Keyworth, Nottingham, England, 15 pp.

Xiong, Z., Tripp, A.C., 1997. 3-D electromagnetic modeling for near-surface targets using integral equations. Geophysics 62(4), 1097-1106. doi: 10.1190/1.1444210.

Yu, L., Chouteau, M., Boerner, D.E., 1998. On the imaging of radio-frequency electromagnetic data forcross-borehole mineral exploration. Geophysical Journal International 135(2), 523-541. doi: 10.1046/j.1365-246X.1998.00655.x.

Zhou, B., Fullagar, P.K., Fallon, G.N., 1998. Radio frequency tomography trial at Mt Isa Mine. Exploration Geophysics 29(3-4), 675-679. doi: 10.1071/EG998675.

Chapter 3

3 Modelling and straight-ray tomographic imaging studies of cross-hole radio-frequency electromagnetic data for mineral exploration[2]

3.1 Abstract

Radio-frequency electromagnetic (EM) tomography (RIM) employs radio-frequency (typically 0.1 – 10 MHz) EM wave propagation to delineate the distribution of electric properties between two boreholes. Currently, the straight-ray imaging method is the primary imaging method for the RIM data acquired for mineral exploration. We carried out synthetic studies using 3D finite-element modelling implemented in Comsol Multiphysics to study the EM field characteristics, and to assess the capability of the straight-ray imaging method using amplitude and phase data separately. We studied four sets of experiments with models of interest in the mining setting. In the first two experiments, we studied models with perfect conductors in homogeneous backgrounds, which show that the characteristics of the EM fields depend mainly on the wavelength. When the borehole separations are less than one wavelength, induction effects occur; conductors with simple geometries can be recovered acceptably with amplitude data, but are incorrectly imaged on the phase tomogram. When the borehole separations are larger than two wavelengths, radiation effects play a major role. In this case, phase tomography provides images with acceptable quality; while amplitude tomography does not provide satisfactory results. The third experiment shows that imaging with both original and reciprocal data sets is somewhat helpful to improve the imaging quality by reducing the impact of noise. In the last experiment, we studied models with conductive zones extended into the borehole plane with different lengths, which were not accurately recovered with amplitude tomography. The experiment implies that it is difficult to determine the extent of a mineralized zone which has been intersected by one of the

[2] Paper published in *Geophysical Prospecting*.

boreholes. Due to the large variation of the wavelength in the radio frequency range, we suggest investigating the local electric properties to select an operating frequency prior to a survey. We conclude that straight-ray tomography with either amplitude or phase data cannot provide high quality imaging results. We suggest using more general methods based on full EM modelling to interpret the data. In circumstances when computational time is critical, we suggest saving time by using either induction methods for borehole separations less than one wavelength or wave-based methods (only radiation fields are considered) for borehole separation larger than two wavelengths.

3.2 Introduction

Radio-frequency electromagnetic (EM) tomography, or the radio imaging method (RIM), is a cross-hole exploration method which employs radio-frequency EM waves propagating between boreholes to image the distribution of electric properties in the plane containing the two boreholes. The electromagnetic waves in the radio-frequency range (typically 0.1 – 10 MHz) provide a good balance between imaging resolution and the signal-to-noise ratio level (Wilkinson 2005). This exploration method has been applied to coal-seam hazards detection (Hill 1984), ore body delineation (Thomson and Hinde 1993; Mutton 2000; Stevens *et al*. 2000) and site selection for underground disposal of nuclear waste (Korpisalo and Heikkinen 2014). A few RIM systems based on EM fields radiated at discrete frequencies have been developed which can measure the amplitude and phase data simultaneously (Yu *et al*. 1998; Karimi-Sharif 2013; Korpisalo and Heikkinen 2014). The information provided by cross-borehole imaging becomes more critical when the mining activities go deeper, as drilling becomes more expensive and more information is required from the boreholes to understand the geology between boreholes.

Due to the large amount of computation for full EM modelling and inversion, some approximations are often made for faster data interpretation. One approximation for low-frequency methods (less than 10^5 Hz, usually used for EM exploration) is the diffusive approximation, in which the impact of the displacement currents is ignored (Ward and Hohmann, 1988). For higher frequencies, the wave equation approximation is made by ignoring the conduction currents, which is the basis for wave-based methods such as diffraction tomography (Devaney, 1984). For very high frequencies, the EM energy can be treated as travelling along rays, which is the basis for the straight-ray imaging method used for X-ray tomography (Dines and Lytle 1979), and the bended-ray tomography used for Ground Penetrating Radar (GPR) data interpretation (Huisman *et al*. 2003). The idea of using electromagnetic tomography for mineral exploration, together with the image reconstruction methods, was adopted from X-ray computer aided tomography (CAT) used in medical imaging, which gained tremendous successes in the 1970s (Dines and Lytle 1979; Jackson and Tweeton 1994). Since then, the straight-ray imaging method has become the primary RIM data interpretation method used in the mining exploration community (Steven et al. 2000; McDowell et al. 2007; Korpisalo 2016). The straight-ray imaging algorithms used to solve the inverse problem include the back projection technique (BPT), the algebraic reconstruction technique (ART), the simultaneous iterative reconstruction technique (SIRT) and conjugate gradient least-square method (CGLS) (Radcliff and Balanis 1979; Hansen and Saxild-Hansen 2012). Of these methods, the SIRT algorithm is the one primarily used in the mining exploration community (Jackson and Tweeton 1994; Yu *et al*. 1998). A critical question usually asked after a survey is whether the reconstructed image is reliable. Wilkinson (2005) argued that the characteristics of EM fields are determined by the dissipation number (also known as loss tangent, $D = \sigma/\omega\epsilon$, where σ is conductivity; ω is angular frequency and ϵ is dielectric permittivity). If $D << 1$, the EM fields are in the

propagation regime and the medium will support radiative waves that depend on the permittivity; if $D >> 1$, the EM fields are in the diffusive regime and the conductivity will heavily damp the EM fields; otherwise, the EM fields are in the transition zone and the characteristics are more complicated and will depend on both of these parameters. Unfortunately, the frequency range used by RIM, together with the physical properties in base-metal mines, renders the EM fields in the transition zone.

Modelling studies on RIM are rarely found in the literature and the behaviour of the EM fields in the transition zone has not been extensively studied. One of the problems is the lack of efficient forward modelling tools. Li and Smith (2015) used the Comsol Multiphysics RF module, which is based on the finite element method, to model the RIM data and they demonstrated its competency by comparing the Comsol modelling results with data from other numerical methods. Li and Smith (2015) investigated the modelling precision and recommended that, to achieve modelling errors less than 1%, there should be at least 7 to 8 elements per wavelength (the models are meshed with tetrahedrons for 3D modelling). The models in this paper will follow this discretization rule from Li and Smith (2015). In this paper, we will carry out synthetic modelling studies to investigate EM field characteristics and assess the capability of the straight-ray imaging method (implemented in ImageWin, www.fullagargeophysics.com) for RIM data. ImageWin is commonly used in the mining industry for rapid RIM data imaging and interpretation.

In section 3.3, we will introduce the theoretical basis of straight-ray tomography, the pre-processing of the amplitude and phase data, and the SIRT algorithm. In the section 3.4, we will use the SIRT algorithm to image the synthetic amplitude and phase data separately. We undertake four experiments on three different types of models of interest to mineral explorationists. Firstly, we will simulate models with a perfectly conductive rectangular

prism embedded in a whole space with varying background conductivities and excited by different transmitter frequencies. We use perfect conductors because the targets of interest (massive sulphides) in mineral exploration usually have high conductivities of the orders of 1 S/m to 100 S/m (Palacky 1987). The idea of these experiments is to reveal the EM field characteristics and assess the capability of the straight-ray imaging method in the transition zone. Yu *et al*. (1998) carried out studies using perfectly conductive models and their results show how the imaging results vary by dissipation number *D*, but they did not compare the results with varying wavelength and skin depth. Secondly, we will use an L-shaped model to assess the ability of straight-ray tomography to delineate conductors with more complex geometries.

Reciprocal data are always collected as a standard procedure in mineral exploration. The original data set has the transmitter in one hole and the receiver in the other hole and the reciprocal data set has the transmitter and the receiver switched. Jackson and Tweeton (1994) carried out studies on imaging with different data coverages using synthetic travel time data, which showed that the imaging results can be improved with configurations that have more transmitters located in a wider range of directions. In our third experiment, we will generate images with the original data, the reciprocal data and the combined data set from the L-shaped models, and will compare the imaging results of data with and without noise, to verify the usefulness of the reciprocal data for straight-ray imaging. Finally, we will build models with conductive zones of different extents from one borehole to assess the ability of straight-ray tomography to delineate the lateral extent of a conductor.

3.3 Methodology

We build models in COMSOL using a discrete-frequency EM source at a specific position (Li and Smith 2015). The output EM data include the amplitude and the phase of the axial

component, which need to be processed before being imaged with the SIRT algorithm. The processes which we use to manipulate the amplitude data are known as the amplitude data reduction (Jackson and Tweeton 1994); the phase data processing is known as phase recovery (Ying 2006).

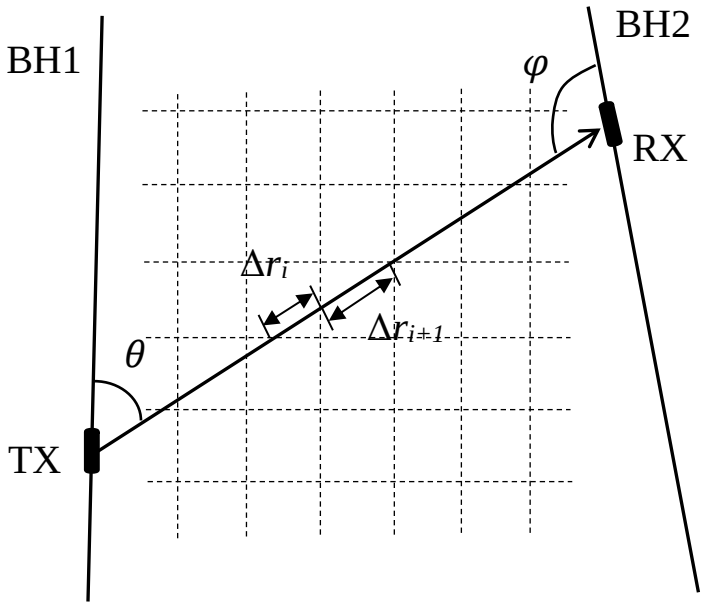

Figure 3-1. Diagram of cross-hole tomography. Transmitter (TX) and receiver (RX) are placed in the borehole 1 (BH1) and borehole 2 (BH2) respectively; θ and φ are polar angles of the transmitter and the receiver, respectively. The cross-hole plane is meshed with a grid. The physical properties within each cell are uniform. The distances in the cells which the straight ray passed through (Δr_i) are calculated according to the geometry of the borehole plane and the cell sizes.

3.3.1 Straight-ray approximation

We assume that the two boreholes are vertical or sub vertical, so the two boreholes are approximately on a 2D plane. The electric fields induced by an antenna in a borehole (Figure 3-1) are approximately considered as the EM fields from a dipole source in a whole-space model. The electric fields induced by a discrete-frequency source in a homogeneous whole-space in spherical coordinates are (after formula (2.40) in Ward and Hohmann 1988),

$$E = \frac{-i\mu\omega kIds}{4\pi} e^{-ikr}\left[\left(-\frac{1}{kr}+\frac{i}{(kr)^2}+\frac{1}{(kr)^3}\right)\sin\theta\, u_\theta + \left(\frac{2}{(kr)^3}+\frac{2i}{(kr)^2}\right)\cos\theta\, u_r\right], \quad (3\text{-}1)$$

where, $\mu = \mu_0\mu_r$ is the magnetic permeability, in which μ_0 is the vacuum permeability and μ_r is relative permeability; $\omega = 2\pi f$ is the angular frequency, in which f denotes the frequency; $k = (\omega^2\mu\epsilon - i\omega\mu\sigma)^{1/2}$ is the wave number, in which $\epsilon = \epsilon_0\epsilon_r$, where ϵ_0 is vacuum permittivity and ϵ_r relative permittivity; Ids is the electric dipole moment; r is the distance from the transmitter to the receiver, θ is the transmitter polar angle (the angle between where the field is evaluated and the axis of the transmitting antenna); u_θ denotes the polar component and u_r denotes the radial component.

The polar component has a first-order term of $1/kr$, a second-order term $1/(kr)^2$, and a third-order term $1/(kr)^3$, which correspond to the radiation field, induction field and the quasi-static field, respectively (Wilkinson 2005). If the receiver is far away from the source ($kr >> 1$), higher order terms tend to zero. The electric field measured by an antenna in another borehole is thus given by the far-field approximation (after removing the second and the third order terms in equation (3-1)),

$$E = \frac{i\mu\omega Ids}{4\pi}\frac{1}{r}\sin\varphi\sin\theta\, e^{-ikr} = E_0\frac{\sin\varphi\sin\theta}{r}e^{-ikr}, \quad (3\text{-}2)$$

where E is with units of V/m, E_0 is the source strength $i\mu\omega Ids/4\pi$, with the units of volts; φ is the receiver polar angle. The wavenumber k can be divided into a real part and an imaginary part: $k = \beta + i\alpha$, in which, β is the phase coefficient, which affects the phase data; α is the attenuation rate, which determines the amplitude data. The values of β and α can be calculated if the physical properties (σ, ϵ, μ) of the material and the transmitting

frequency *f* are known using the formula (1.48) and (1.49) in Ward and Hohmann (1988), which are given as followed,

$$\alpha = \left\{\frac{\omega^2\mu\epsilon}{2}\left[\left(1+\frac{\sigma^2}{\epsilon^2\omega^2}\right)^{1/2}-1\right]\right\}^{1/2}, \tag{3-3}$$

$$\beta = \left\{\frac{\omega^2\mu\epsilon}{2}\left[\left(1+\frac{\sigma^2}{\epsilon^2\omega^2}\right)^{1/2}+1\right]\right\}^{1/2}. \tag{3-4}$$

3.3.2 Amplitude data reduction

If the amplitude data is considered in the straight-ray method, we can image the attenuation rate of the materials. Following the approach of Jackson and Tweeton (1994) and taking the natural logarithm of the amplitude of equation (3-2), we have

$$\ln(E) + \ln(r) - \ln(E_0) - \ln(\sin\theta) - \ln(\sin\varphi) = \alpha r. \tag{3-5}$$

In this equation, E is the amplitude data measured in the receiver hole; $\ln(r)$ is called the geometry spherical correction; $\ln(\sin\theta)$ is the radiation pattern correction; $\ln(\sin\varphi)$ is the receiving angle correction; $\ln(E_0)$ is the source strength correction. By all these operations, we calculate the reduced amplitude data A_R (defined as the left hand side of equation (3-5)). It can be seen from equation (3-5) that the reduced data vary linearly with the attenuation rate of the homogeneous earth material, α. For inhomogeneous models with varying attenuation rates along the ray path, the total attenuation can be represented in an integral form,

$$A_R = \int_0^{r_R} \alpha(r')\mathrm{d}r', \tag{3-6}$$

where r_R denotes the distance along the straight ray from the transmitter to the receiver.

3.3.3 Phase recovery

The phase of the electric field used in the straight-ray method is determined by the imaginary part of the exponential in equation (3-2). The source term E_0 is positive and imaginary, so the phase of the source is $\pi/2$. The phase Φ of the measured electric field is,

$$\Phi = \text{wrap}\left(\frac{\pi}{2} - \beta r\right), \tag{3-7}$$

where the function *wrap* ensures the angle is in the range of ($-\pi$, π). We recover the absolute phase by unwrapping and adding 2π to the data for each cycle change. This assumes that the phase data are continuous (no rapid change) and all the data are above the noise level. The recovered phase data Ph_R are linear with the phase coefficients,

$$Ph_R = \frac{\pi}{2} - \text{unwrap}(\Phi) + n \times 2\pi = \int_0^{r_R} \beta(r)\,\mathrm{d}r, \tag{3-8}$$

in which, the function *unwrap* is to deal with the phase change from $-\pi$ to π, or from π to $-\pi$. We need to estimate how many cycles there are between the transmitters and the receivers and add the quantity ($n \times 2\pi$) to the unwrapped phase data. The number of cycles can be estimated by comparing the r and the wavelength calculated with the physical properties.

3.3.4 Tomography

The panel of interest, defined as the plane between the two boreholes, is discretized with a grid (Figure 3-1). The physical properties are assumed to be uniform within each cell. The total attenuation and the recovered phase of each measurement (each associated with a ray-path) are the sums of the attenuation and the phase shift in all the cells the ray passed through. The attenuation (the phase shift) of a specific cell is the product of the attenuation rate (the phase coefficient) and the distance the ray propagates inside that cell. Equations (3-6) and (3-8) have the form,

$$d_j = \sum_{i=1}^{N} \Delta r_{ij} x_i \,, \quad \text{with } j = 1, \dots, M \text{ and } i = 1, \dots, N \tag{3-9}$$

where, d_j denotes the jth data (either reduced amplitude or recovered phase data); M is number of measurements; x_i is the model properties of the ith cell (either attenuation rate or phase coefficient); N is the number of cells; Δr_{ij} denotes the distance that the jth ray path passed through the ith cell, which is calculated according to the geometries of the boreholes and the cell sizes. All the borehole planes in this paper are meshed with a cell size of 4 m × 4 m. Combining all the measurements, we can put equation (3-9) in matrix form,

$$\mathbf{D} = \mathbf{R}\mathbf{X}. \tag{3-10}$$

where $\mathbf{D}$ and $\mathbf{X}$ are column vectors of length M and N respectively; $\mathbf{R}$ is an $M \times N$ matrix. Now, the problem becomes solving a set of linear equations to find the solution, $\mathbf{X}$.

A number of inversion techniques have been developed for algebraic iterative reconstruction methods (Hansen and Saxild-Hansen 2012). In this paper, we use the SIRT algorithm,

$$\mathbf{X}_{k+1} = \mathbf{X}_k + \mathbf{R}^{\mathrm{T}}(\mathbf{D} - \mathbf{R}\mathbf{X}_k), \tag{3-11}$$

where, $\mathbf{X}_k$ and $\mathbf{X}_{k+1}$ denote the input model and output model respectively in each iteration; the superscript T means transposition of the matrix. The stopping criterion for the algorithm is that the number of iterations reaches a pre-set maximum (50 iterations for all the presented tests) and no observable changes are present in the model with more iterations. The initial value of $\mathbf{X}_0$ is set to a constant background value.

After we have an inversion model satisfying equation (3-10), we transform the model value (either attenuation rate or phase coefficient) to conductivity by rearranging equation (3-3) and (3-4) as,

$$\sigma = \omega\epsilon\left[\left(\frac{2\alpha^2}{\mu\epsilon\omega^2} - 1\right)^2 - 1\right]^{1/2}, \tag{3-12}$$

$$\sigma = \omega\epsilon\left[\left(\frac{2\beta^2}{\mu\epsilon\omega^2} + 1\right)^2 - 1\right]^{1/2}. \tag{3-13}$$

The transformations assume that ϵ and μ are constants. The dissipation (*D*, as mentioned in the introduction), wavelength (λ) and the skin depth (δ) can be calculated with,

$$D = \frac{\sigma}{\omega\epsilon}, \tag{3-14}$$

$$\lambda = \frac{2\pi}{\beta}, \tag{3-15}$$

$$\delta = \frac{1}{\alpha}. \tag{3-16}$$

These three quantities are discussed further in this paper.

3.4 Modelling study

3.4.1 Imaging at or near the transition zone

We build models with two 100 m-long vertical boreholes which are 100 m apart. As shown in Figure 3-2, we define the centre location between the boreholes as the origin of a Cartesian coordinate system, with the *x*-axis from left to right, the *z*-axis from down to up and the *y*-axis perpendicular to the borehole plane (the borehole plane is at *y* = 0 m). We put a vertical electric dipole in the left borehole to simulate a transmitter antenna and calculate the vertical field in the right borehole (the synthetic receiver data). To simulate a RIM survey, we repeated the simulation with transmitters every 5 m along the borehole. The receiver data separation in the other borehole depends on the element size, and we simulated evenly spaced

field data by interpolating the data to give receiver stations spaced 1 m apart. A perfectly conductive anomaly is placed between two boreholes (from x = -15 m to x = 15 m, from y = -20 m to y = 20 m and from z = -10 m to z = 10 m). Intersections of the conductor with the borehole plane are shown as the black outlines on Figure 3-2. We carried out experiments to study the EM fields excited by a conductor with different conductivities using radio frequency electromagnetic fields (not shown in this paper), which showed that the excited EM fields are not significantly affected if the conductivity varies in the range greater than 1 S/m. So, massive sulphide ore-bodies with conductivity over 1 S/m can be treated as perfect conductors.

Table 3-1. Dissipation (D), Wavelength (λ) and skin depth (δ) of the background model (see equation (3-12), (3-13) and (3-14)).

Conductivity (S/m)		0.0001113	0.0003338	0.001113
Dissipation	3 MHz	0.11	0.33	
	1 MHz	0.33	1	3.3
	0.3 MHz		3.3	
Wavelength (m)	3 MHz	40.7	40.3	
	1 MHz	120.8	111.4	81.8
	0.3 MHz		272.6	
Skin depth (m)	3 MHz	117.0	39.5	
	1 MHz	118.4	42.8	17.5
	0.3 MHz		58.3	

To build models at the transition between the diffusive regime and the propagation regime, we used a background conductivity of 0.0003338 S/m and a transmitted frequency of 1 MHz to meet the condition of D = 1. The relative permittivity and the magnetic permeability are uniform throughout the models in all the experiments in this paper: ϵ_r = 6, μ_r = 1. We used

homogeneous permittivity and magnetic permeability because, in the mining environment, the conductivity usually plays a major role in the electrical property contrasts. To simulate two cases closer to the diffusion regime (D = 3.3), we i) increased the conductivity to σ = 0.001113 S/m and ii) decreased the frequency to f = 0.3 MHz. For the propagation regime (D = 0.33), we i) decreased the conductivity to σ = 0.0001113 S/m and ii) increase the frequency to f = 3 MHz. We also studied the model with σ = 0.0001113 S/m and f = 3 MHz (D = 0.11), which is used to substantiate our arguments below. The model parameters, as well as the dissipation, wavelength and the skin depth for these cases are shown in Table 3-1.

A prism of 100 m × 100 m × 40 m (with the two boreholes on either side) is deemed as the domain of interest for the 3D model in Comsol. For the models of 3 MHz, we discretize the domain of interest with maximum element size of 5 m. For the models of 1 MHz and 0.3 MHz, we discretize the domain of interest with a maximum element size of 6 m. The element sizes meet the requirement of more than 8 elements per wavelength to achieve a modelling error within 1% (Li and Smith 2015) and provide fine enough sampling to ensure accurate results at closely sampled receivers. The sizes of elements outside the domain of interest can be larger, because these element sizes do not significantly affect the modelling precision. We have implemented a perfect conductor in Comsol by using a perfectly conductive boundary condition, so the element size inside the conductor is immaterial. These meshing parameters are also applied for the models in the following subsections. We use the biconjugate gradient stabilized iterative method (BiCGStab) (COMSOL Multiphysics User Guide, 2012) as the solver for all the models in this paper.

We applied the amplitude data reduction to the synthetic data and then performed amplitude tomography. The imaged conductivities for all models on each region of interest are shown in Figure 3-2. If the imaging results vary only with the dissipation number D, then we would

expect images along the upward diagonals to be similar. However, the similarities are greater along rows; the imaging results for 0.3 MHz (bottom row) and 1 MHz (middle row) seem much better than those for 3 MHz (top row), if one considers the location and shape of the conductors. The lower limits of the colour bars are associated with the background conductivities, and the upper limits are associated with about three times the value of the background conductivities. While the conductors have infinite conductivity, the imaged conductivities are about 1.5 to 2.5 times the conductivities of the background for the imaging results of 0.3 MHz and 1MHz. Using the value of wavelength in Table 3-1, we infer that the value of the conductivity varies with the wavelength: the longer the wavelength, the larger the conductivity is above the background.

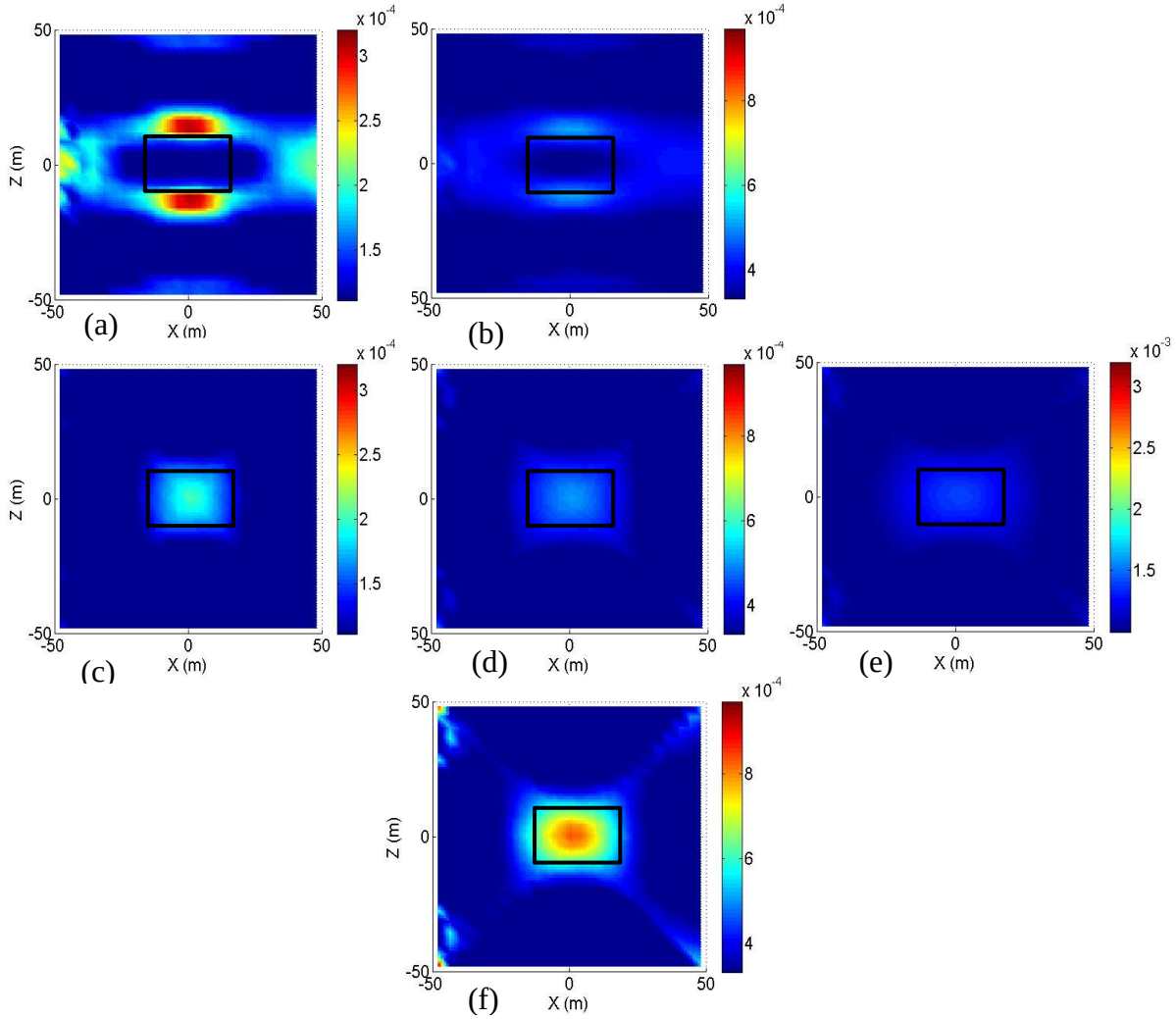

Figure 3-2. Tomograms derived from reduced amplitude data for a perfectly conductive anomaly with a size of 30 m × 20 m × 40 m at the centre of each panel (outlines shown in black). (a): f = 3 MHz, σ = 0.0001113 S/m; (b): f = 3 MHz, σ = 0.0003338 S/m; (c): f = 1 MHz, σ = 0.0001113 S/m; (d): f = 1 MHz, σ = 0.0003338 S/m; (e): f = 1 MHz, σ = 0.001113 S/m; (f): f = 0.3 MHz, σ = 0.0003338 S/m. Dissipation, wavelength and skin depth for each panel are shown in Table 3-1 (same spatial arrangement for Figure 3-3, Figure 3-4 and Figure 3-5). The quantity on the colour bars is conductivity, with unit S/m.

To understand how the EM fields interact with the conductors, we plotted the relative-amplitude-variation maps of the *E* fields for the models with the transmitters at the centre of the borehole (x = -50 m, z = 0 m). We define the relative-amplitude variation V_R as

$$V_R = \frac{A_c - A_h}{A_h} * 100\%, \tag{3-15}$$

where, A_C is the amplitude data with the conductor in the model; A_h is amplitude data for the homogeneous whole-space model. We used the vertical component of the electric field for A_c and A_h. The relative-amplitude-variation maps are plotted in Figure 3-3. Reddish (and blueish) colours in these maps illustrate where and by how much the magnitudes are increased (and decreased) by the presence of the conductor.

As expected, the amplitude values inside the conductors decrease drastically, due to the electric shielding effects. For the case of f = 0.3 MHz (Figure 3-3f) and the cases of f = 1 MHz with low conductivities of the background (Figure 3-3c and d), the amplitude values above and below the conductor show significant increases. Due to the long wavelengths for these conditions (over 100 m, see Table 3-1), the distance between the boreholes is less than one wavelength. We interpret that the increased E fields are caused by fields induced in the conductor by the source field. For the higher-frequency cases of 3 MHz (Figure 3-3a and b), radio shadows behind the conductors are observed, but there are 'brighter spots' (light blue) centred on (x = 50 m, z = 0 m), which we interpret to be caused by interference of the EM fields that passed around the conductive bodies. These features are caused by the diffraction phenomenon, which occurs when the size of an object is comparable to the wavelength (Devaney 1984). Further experiments (not shown in this paper) show that the diffraction phenomenon exists up to f = 10 MHz (λ = 12 m). These bright spots are what the receiver in the right borehole senses and this larger amplitude is responsible for a more resistive zone in the centre of the tomograms (Figure 3-2a and b). The more attenuated (dark blue) zones above and below are responsible for the conductive zones above and below the central zone in the tomograms of Figure 3-2a and b.

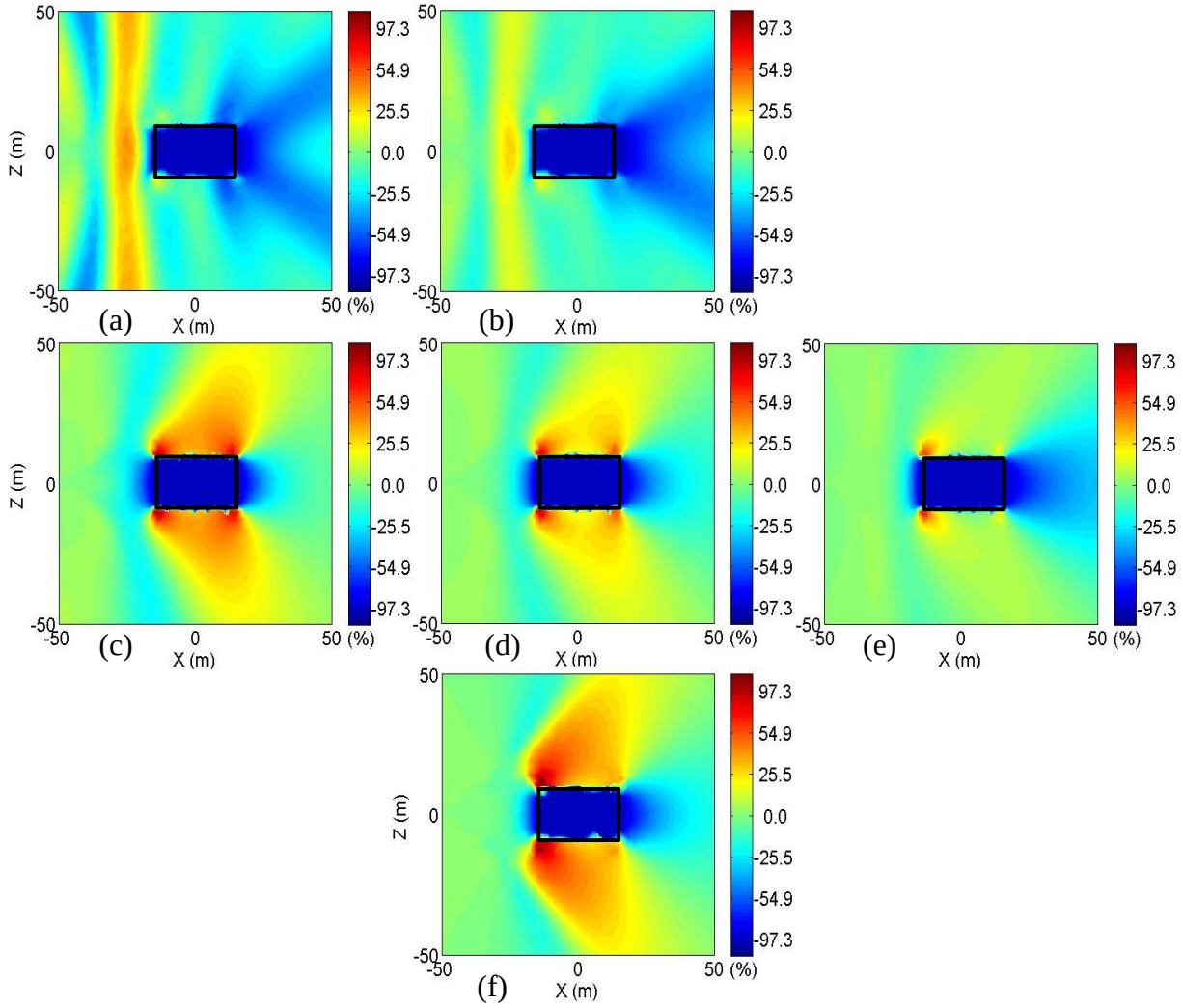

Figure 3-3. Relative-amplitude-variation V_R maps of electric fields with the source at the point (x = -50 m, z = 0 m) and perfectly conductive anomalies at the centre. Reddish colours indicate where and how much the fields are increased, while blueish colours show a decrease. Units on the colour bars are percent (%). Frequency and background conductivity vary in each panel as in Figure 3-2 and Table 3-1.

Note that Figure 3-2b, Figure 3-2c and Figure 3-3b, Figure 3-3c have identical dissipation numbers (D = 0.33), but the imaging results and the EM field interactions are quite different, which indicates that dissipation number is not a strong determinant of the quality of a tomographic reconstruction. A resemblance between Figure 3-2a (Figure 3-3a) and Figure 3-2b (Figure 3-3b) can be observed. We can see from Table 3-1 that the dissipation numbers

are different, but the wavelengths are similar (around 40 m). Thus, we infer that, for this example the imaging results and the EM field interaction depend on the wavelength.

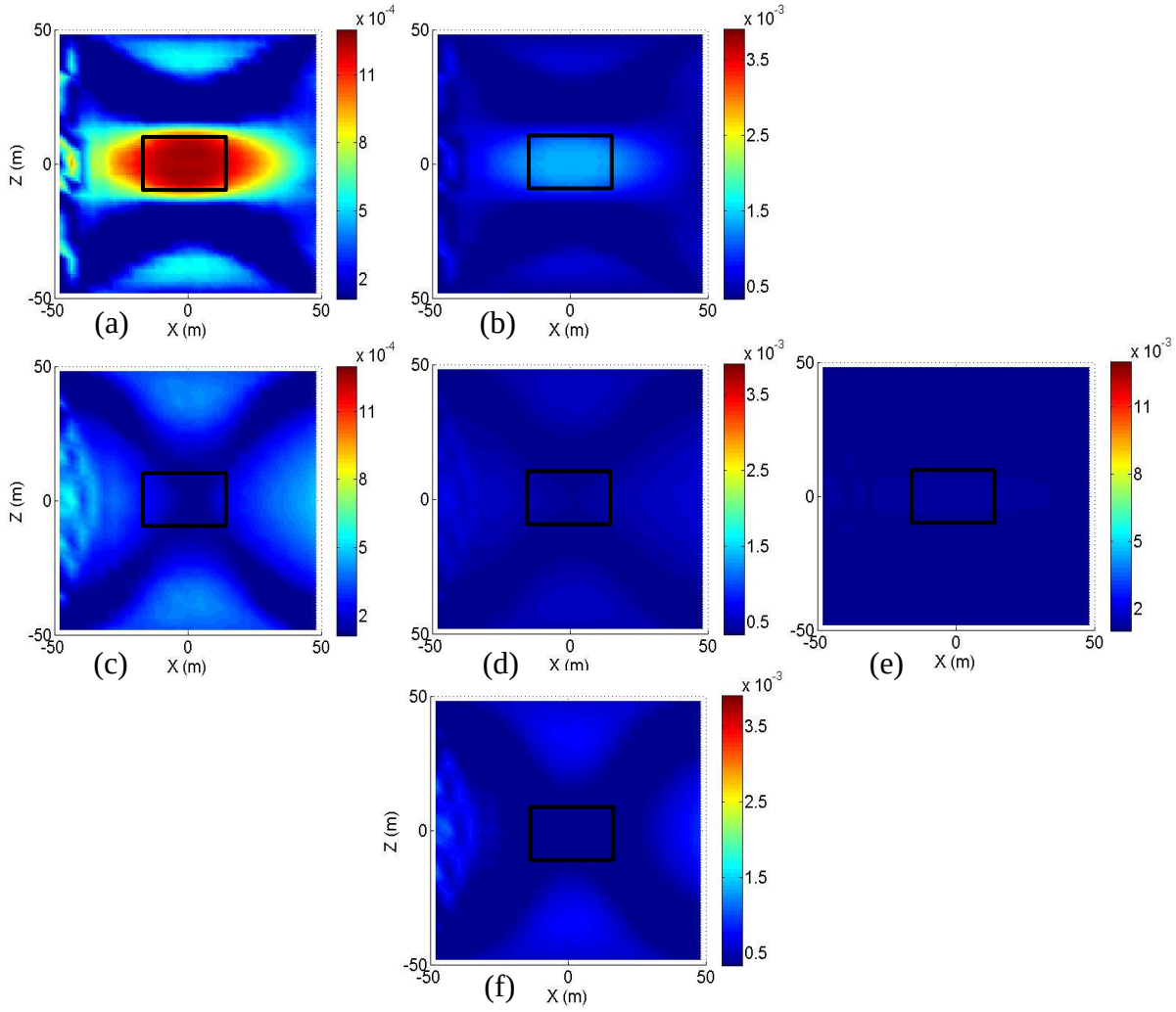

Figure 3-4. Tomograms derived from recovered phase data. The quantity on the colour bars is conductivity, with unit S/m. The arrangement of panels is the same as Figure 3-2.

We recovered the phase data and performed phase tomography (Figure 3-4). The lower limits of the colour bars in the tomograms are associated with the background conductivities, and the upper limits are associated with around 12 times the value of the background conductivities. The location and the shape of the conductors are shown correctly on the tomograms of 3 MHz (Figure 3-4a and b, top row), but not shown on the tomograms of 0.3 MHz and 1MHz (Figure 3-4c, d, e and f). We can see a transition of the tomographic results

in the case of Figure 3-4e (f = 1 MHz, σ = 0.001113 S/m), in which the petal-shaped artefacts (see Figure 3-4c, d and f) are suppressed and the correct shape of the conductor is beginning to appear. The imaged anomaly on Figure 3-4a is much stronger than that on Figure 3-4b, although the wavelengths for these two models (Table 3-1) are similar. We also observe that the maximum obtained conductivities on Figure 3-4a and b are approximately the same: 0.0015 S/m. We infer that there is an upper threshold of conductivity that the phase tomography is able to resolve. The lower the background conductivity is, the stronger the recovered anomaly. From Table 3-1 and Figure 3-4, we infer that the phase imaging results are more suitable for the models with shorter wavelengths and higher conductivity contrasts.

To better understand the phase tomography results, we plotted the phase grid maps with contours of the electric fields for the cases when the transmitters were at the vertical centre point (x= -50 m, z = 0 m). In the phase grid maps, the areas on the borehole plane with the same phase value have the same colour and denote the wave front, which reveal the propagation path of the EM wave. We can see from Figure 3-5 that the shorter the wavelength, the faster the phase data change and thus, the shorter the distance between repetitions of a colour. The wavelength for the case of Figure 3-5b is 40.3 m, which is about the distance for one phase cycle (from red to the next red).

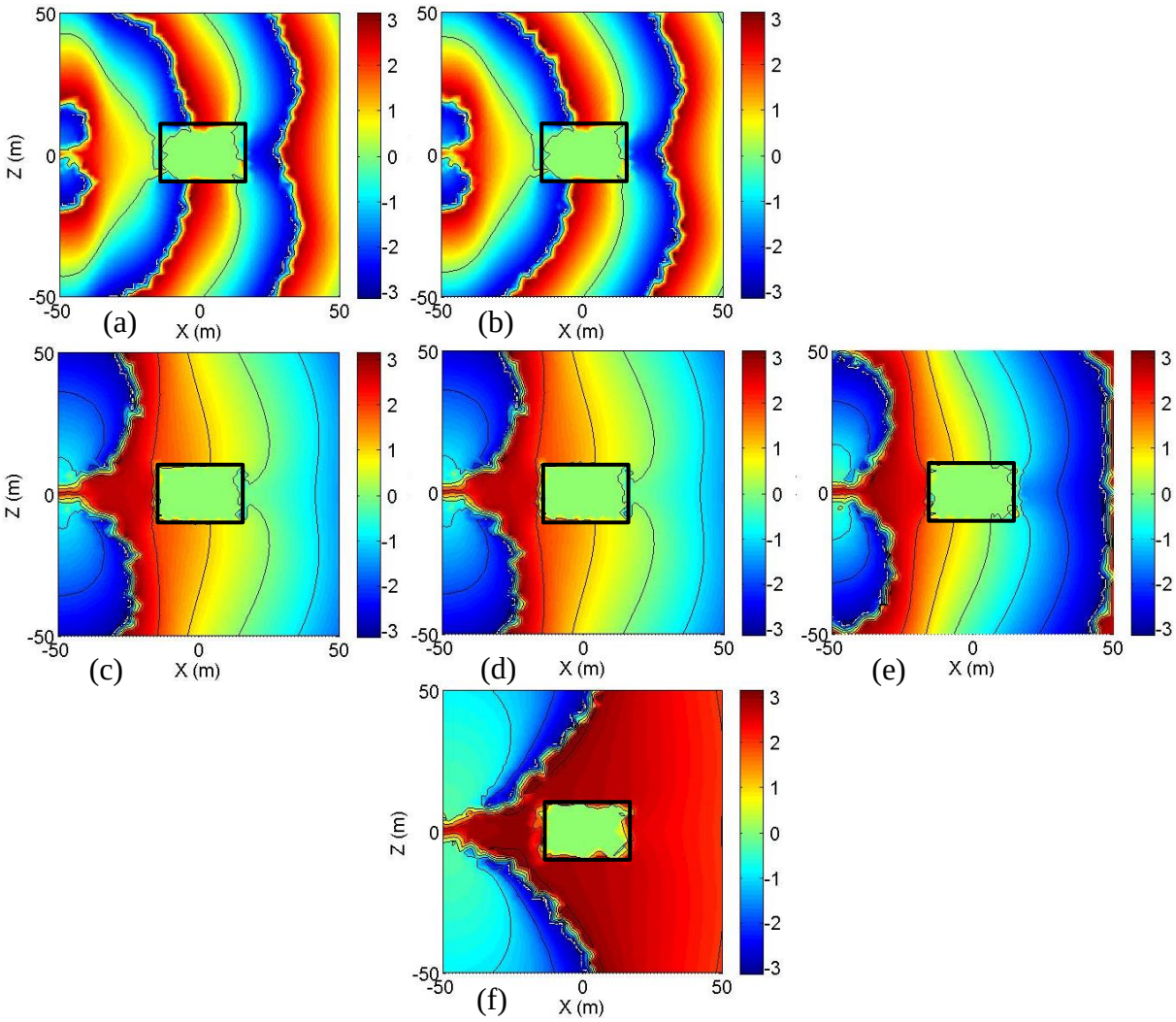

Figure 3-5. Contoured phase grid maps with sources at the point (*x* = -50 m, *z* = 0 m). The quantity on the colour bars is the phase angle, with unit of radians. Panels (a) and (b) have contours on phase value of (-3, 0, 3); (c), (d), (e) and (f) have contours (-3, -2, -1, 0, 1, 2, 3).

It can be noticed in Figure 3-5a and b that, the geometric shape of the phase distribution closest to the source (distances less than 1 wavelength) is different from the phase further away from the source. More than 1.5 wavelengths away from the source, the phase change depends only on the distance from the source (not the angle), so areas with the same value form arc-shape stripes, which have the centre at the source position (e. g. the red stripes cutting through the conductors in Figure 3-5a and b, if we ignore the phase in the conductor). While, closer to the source, the arc shape is distorted to be sub-vertical (e. g. the yellow stripes in Figure 3-5d and e). Within half a wavelength, the phase distribution changes to the

shape of two circles (near-field dipole approximation), where the phase values vary with changing polar angle (blue areas in Figure 3-5c and f). For the longer wavelength cases there is very little distortion of the phase data by the conductors on the far right (where the receivers are), so the phase tomography is unable to recover the anomalous model.

We can understand the phase variation from equations (3-1) and (3-8). For locations far away from the source ($kr >> 1$), only the first-order term needs to be considered, so the far-field approximation in equations (3-2) and (3-7) is applicable, in which case the phase change is linear with the distance. However, for locations closer to the source, the higher-order terms have larger effects. For locations less than half wavelength from the source, the third-order term dominates (quasi-static fields from the electric dipole), which forms the two circles above and below the source.

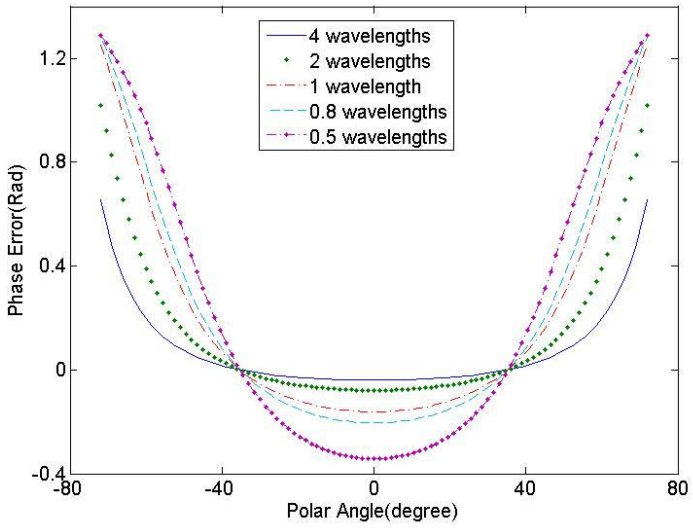

Figure 3-6. Phase discrepancies (Ph_d - Ph_f) between the approximated far-field (Ph_f) and the dipole field (Ph_d) for different distances (0.5, 0.8, 1, 2, and 4 λ) away from the source plotted against the polar angles.

We illustrate the effects of higher-order terms by comparing equations (3-1) and (3-2). Figure 3-6 shows the discrepancies of the phase value of the approximated far-field (Ph_f) and the phases of the dipole field (Ph_d — equation (3-1)) for different distances (0.5, 0.8, 1, 2, and 4

wavelengths) away from the source plotted as a function of the polar angle. From Figure 3-6, we can see that, within 1 wavelength, the phase discrepancies between the dipole field and the far-field are large for the whole range of polar angles. Between the polar angle of about -35 to 35 degrees, the phase of the dipole field is smaller than the far-field phase; outside of this range, the dipole phase is larger than the far-field phase. For distances greater than two wavelengths and in the polar angle range of about -50 to 50 degree, the phase discrepancies are small (< 0.1 radians). The tomograms for Figure 3-4a and b meet these conditions, which explains why the conductors can be recovered.

The phase grid maps in Figure 3-5 show how the conductor retards the phase. For perfect conductors, it is observed that the EM waves pass around the target, which is not accounted for in the straight-ray assumption. As the EM waves pass around the conductors, it takes longer for the EM waves to propagate, and this distortion is manifest as a retardation of the phase at the receiver. We can see from Figure 3-5 that, the contrast of phase retardation is higher for shorter wavelengths (comparing the contours of Figure 3-5a with those of Figure 3-5c). We infer that this is the second reason the phase imaging results are better at higher frequencies.

From the modelling and imaging experiments above, we found that the characteristics of radio-frequency EM depend mainly on the wavelength, rather than the dissipation or the skin depth. If there is a conductor less than 1 wavelength away from the source, the induction fields play a major role on the data. In this situation, phase tomography does not work well due to the effects of higher-order terms of the dipole fields; whereas amplitude tomography seems to work well (discussed further in the next subsection). If the conductor is more than 2 wavelengths away from the source, the induction fields decay significantly and the radiation fields play a major role on the data. In this case, phase tomography works quite well because

the far-field approximation is applicable; whereas amplitude tomography generates poor images with low conductivity zones at the centre of the conductors because of the diffraction phenomenon.

The wavelengths in the radio-frequency range in common resistive geological environments actually vary from about 12 m to 1000 m (Table 3-2). We can see from Table 3-2 that the wavelength depends on both the frequency (for the whole radio-frequency range), as well as the conductivity, particularly for lower frequencies (0.1 to 1 MHz). For common borehole separations of several hundred meters, the EM field interaction with the geological targets can vary from mainly induction to mainly radiation. So, it is necessary to know the wavelength of the EM fields in exploration. To calculate the wavelength, we need to estimate the conductivity of geological materials around the boreholes either by borehole logging, measuring the core samples or using a simple whole-space modelling tool (Naprstek and Smith 2016).

Table 3-2. Wavelength (λ) in the radio-frequency range in common resistive environments.

conductivity (S/m)	frequency (MHz)				
	0.1	0.3	1	3	10
0.001	311.0	173.7	84.9	37.1	12.1
0.0001	848.8	371.4	121.1	40.7	12.2
0.00001	1210.7	407.5	122.4	40.8	12.2

3.4.2 L-shaped models

From Figure 3-2, it seems that the shape of the conductive anomalies can be reconstructed with amplitude data at the frequencies of 0.3 MHz and 1 MHz (Figure 3-2c, d, e and f), as well as the phase data at 3 MHz (Figure 3-4a and b). We built models with more complex shapes to assess the general capability of straight-ray tomography to resolve the shape of the conductors. The coordinate system is the same as the previous model study. An L-shaped

conductive body is constructed by cutting a 25 m × 25 m ×40 m rectangular prism out of a 40 m × 40 m × 40 m cube. The intersection of the body on the borehole plane is an L-shaped object (outlines on Figure 3-7), with the strike from y = -20 m to y = 20 m. The object is a perfect conductor, in a background of σ = 0.0003338 S/m. The transmitter and receiver spacing are the same as for the previous experiments. We computed the data for both 1 MHz and 3 MHz, and did amplitude tomography for 1 MHz and phase tomography for 3MHz.

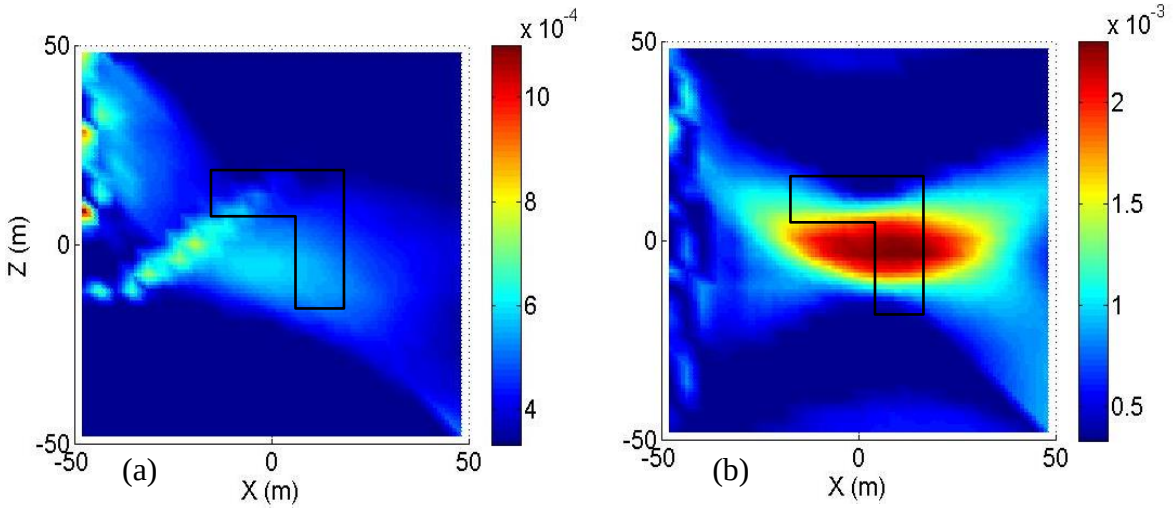

Figure 3-7. Amplitude tomogram of 1 MHz (a) and phase tomogram of 3 MHz (b) of the model with an L-shaped perfect conductor. The transmitters are in the left borehole. Background σ = 0.0003338 S/m. The quantity on the colour bars is conductivity, with unit S/m.

The amplitude tomographic result of 1 MHz (Figure 3-7a) shows limitations. There are artefacts associated with transmitter positions at the top of the hole and a diagonal linear artefact. The feature associated with the conductor (light blue zone at (x, z) = (-5, -5)) is in roughly the correct location, but the shape is not recovered. We interpret that the artefacts on the upper left of Figure 3-7a are caused by the strong induced fields by the left part of the conductor, and the sparse transmitter spacing compared with the cell size (the cell size of all the tomograms in this paper is 4 m × 4 m), such that some cells close to the transmitters do not have many rays passing through them, while others do. The phase tomogram of 3 MHz (Figure 3-7b) shows one body roughly centred on the L-shaped object. Though the shape of

the body is not correct, the reconstructed image does show the right part of the body more conductive than the left. Also, the conductivity contrast is higher compared to the background, which makes it easier to identify the anomaly.

Our experiments on rectangular prisms (the previous subsection) show that amplitude tomography works for 0.3 MHz and 1 MHz for a simple model, but it does not work well for more complicated models. We interpret that, the rectangular prism model is a special case in which the induction in the conductive body generates a symmetric decrease of the field behind the conductors, which is similar to the radio shadow. That explains why the imaging results for 0.3 MHz and 1 MHz (Figure 3-2c, d, e and f) are reasonable. But, the manner that the fields decrease is not the same as is implicit in the assumptions made by the straight-ray tomography, either in terms of the ray path or the relative changes of the E-field magnitude (Figure 3-3c, d, e and f). So, for more complicated models, the imaging results are unsatisfactory. The imaging results with phase tomography for 3 MHz data are quite stable, even for a complicated model. Unfortunately, the phase data are not able to be recovered in all circumstances (see subsection Lateral extent of conductors).

3.4.3 Reciprocity and noise

To verify the usefulness of reciprocal data, we computed a synthetic reciprocal data set with Comsol using the same L-shaped model used in the previous subsection, but switched the positions of the transmitters with the receivers for both the 1 MHz and 3 MHz cases, while keeping the transmitter spacing 5 m and the receiver spacing 1m. Figure 3-8 shows the amplitude tomograms for 1 MHz (Figure 3-8a and c) and phase tomograms for 3 MHz (Figure 3-8b and d). The upper row of Figure 3-8 is the imaging results with the reciprocal data (Figure 3-8a and b), while the lower row shows the results from the combined data set (Figure 3-8c and d).

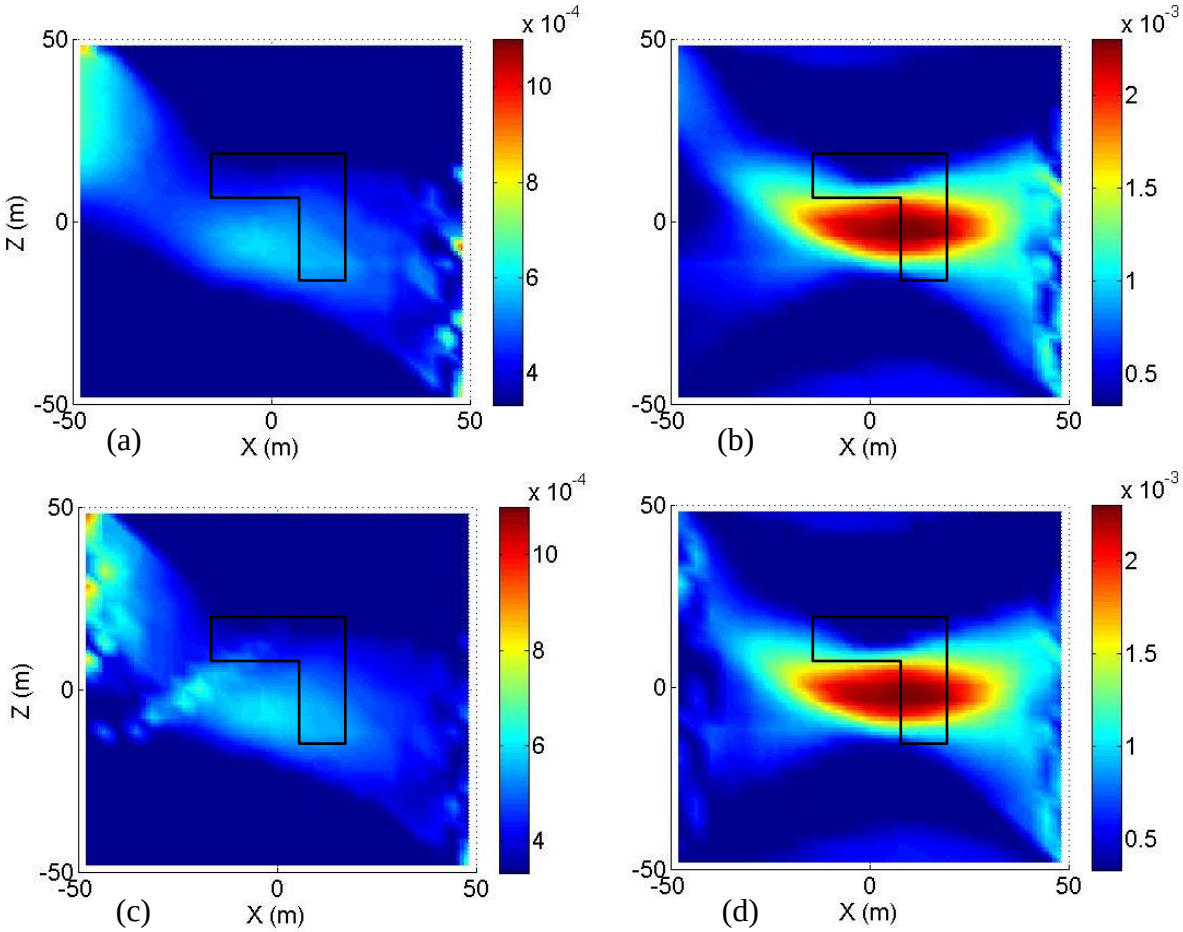

Figure 3-8. Tomograms of the L-shaped anomaly with reciprocal data with transmitters in the right borehole (upper row) and tomograms with the both data sets combined (lower row). The results with transmitters on the left are shown in Figure 3-7. (a) and (c): amplitude tomogram for 1 MHz; (b) and (d): phase tomogram for 3 MHz. The quantity on the colour bars is conductivity with unit S/m.

Compared with Figure 3-7, switching the transmitters to the right borehole (Figure 3-8a and b) switched the discrete artefacts to the same side. Apart from the transmitter artefacts, and the narrow diagonal artefact in Figure 3-8a, the tomograms with reciprocal data are very similar to the results obtained from the original data set. The imaging results with both data sets combined (Figure 3-8c and d) are consistent with the original and reciprocal tomograms. The imaging qualities are not significantly improved: the artefacts are now present on both left and right sides of the combined tomogram.

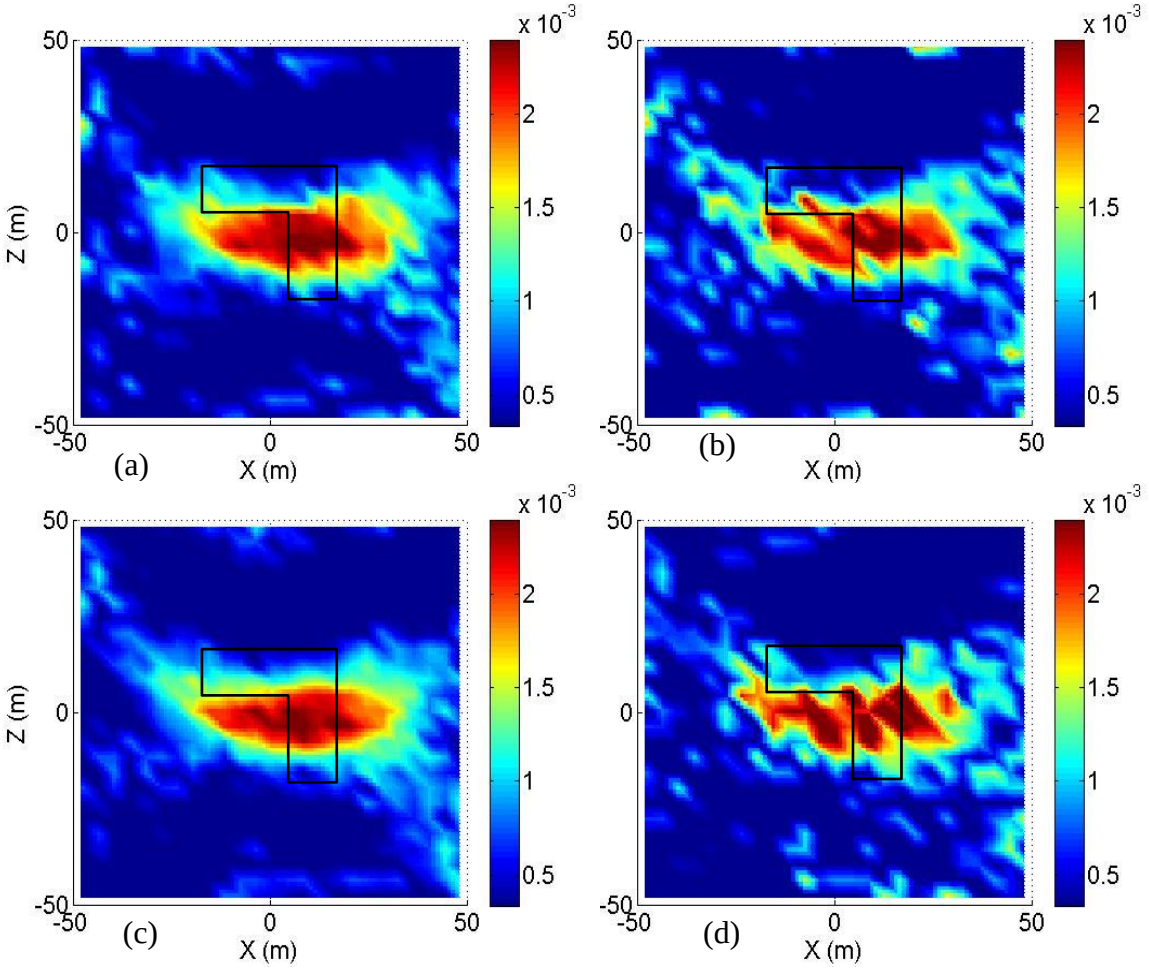

Figure 3-9. Phase tomograms of an L-shaped perfect conductor for 3 MHz with (a) transmitters on the left and 5% noise; (b) transmitters on the left and 10% noise; (c) both reciprocal data sets with 5 % noise; and (d) both data sets with 10% noise. The quantity on the colour bars is conductivity, with units of S/m.

Until now all experiments have been performed with noise free data. To find out how noise affects the imaging results, we added 5% and 10% random multiplicative noise (random distribution in the ranges of (0.95, 1.05) and (0.9, 1.1)) to the 3 MHz phase data of the L-shaped model. The imaging results are shown in Figure 3-9. Figure 3-9a and b are the imaging results with transmitters on the left; Figure 3-9c and d are the imaging results with both data sets. We added 5% noise to the data of Figure 3-9a and c; and 10 % to Figure 3-9b and d. It is observed from Figure 3-9 that the imaging results are patchier than those in Figure 3-7 and Figure 3-8; the results of data with 10% noise (Figure 3-9b and d) are even worse.

Compared to images derived from one of the reciprocal data sets, the imaging result of the combined data set with 5% noise (Figure 3-9c) shows some improvement. The tomogram of combined data sets with 10% noise (Figure 3-9d) looks quite patchy, but we can observe in the left part of the tomogram, particularly the area between the conductor and the left borehole, that a slight improvement is made compared with the result derived from the single data set (Figure 3-9b). The tomogram with the single data set (Figure 3-9b) is patchier in such a manner that the conductive area could be erroneously interpreted to extend from the right borehole all the way to the upper left borehole. Whereas, the tomogram with the combined data set (Figure 3-9d) is somewhat cleaner on the left part and we are more likely to interpret a distinct conductive area midway between two boreholes. Hence we conclude that if there is noise in the data, imaging with both of the reciprocal data sets combined can in some instances improve the imaging quality somewhat by reducing the impact of noise.

3.4.4 Lateral extent of conductors

To evaluate the efficiency of RIM to delineate the extent of a conductive zone that traverses one borehole, we made two models with conductive zones of different lengths in the borehole section. The first model has a 30 m × 20 m × 40 m conductive zone, which intersects the borehole plane with a 30 m × 20 m rectangle (10 m is to the left of the borehole and 20 m to the right — outlined on Figure 3-10a and c). The strike of the zone is 40 m (from y = - 20 m to y = 20 m). The second model has a 70 m × 20 m × 40 m conductive zone, which intersects the borehole plane with a 70 m × 20 m rectangle (10 m to the left of the borehole, 60 m to the right — outlined on Figure 3-10b and d). The conductivity of the zones is σ = 1 S/m, while the background σ = 0.0003338 S/m. We put the transmitters in the right borehole and compute the synthetic data for 1 MHz and 3 MHz. The experiments on rectangular prisms demonstrated that the amplitude tomography does not work well when the wavelength is short compared with the transmitter conductor separation. Even so, we have included the

amplitude tomographic results of the 3 MHz data to investigate how diffraction affects the imaging results when the conductive zone intersects one borehole. Due to the high conductivity of the zone, the receiver data inside the conductive zone are highly attenuated and hence the phase data are not continuous. In this case, we are not able to unwrap the phase information, so phase tomography was not carried out.

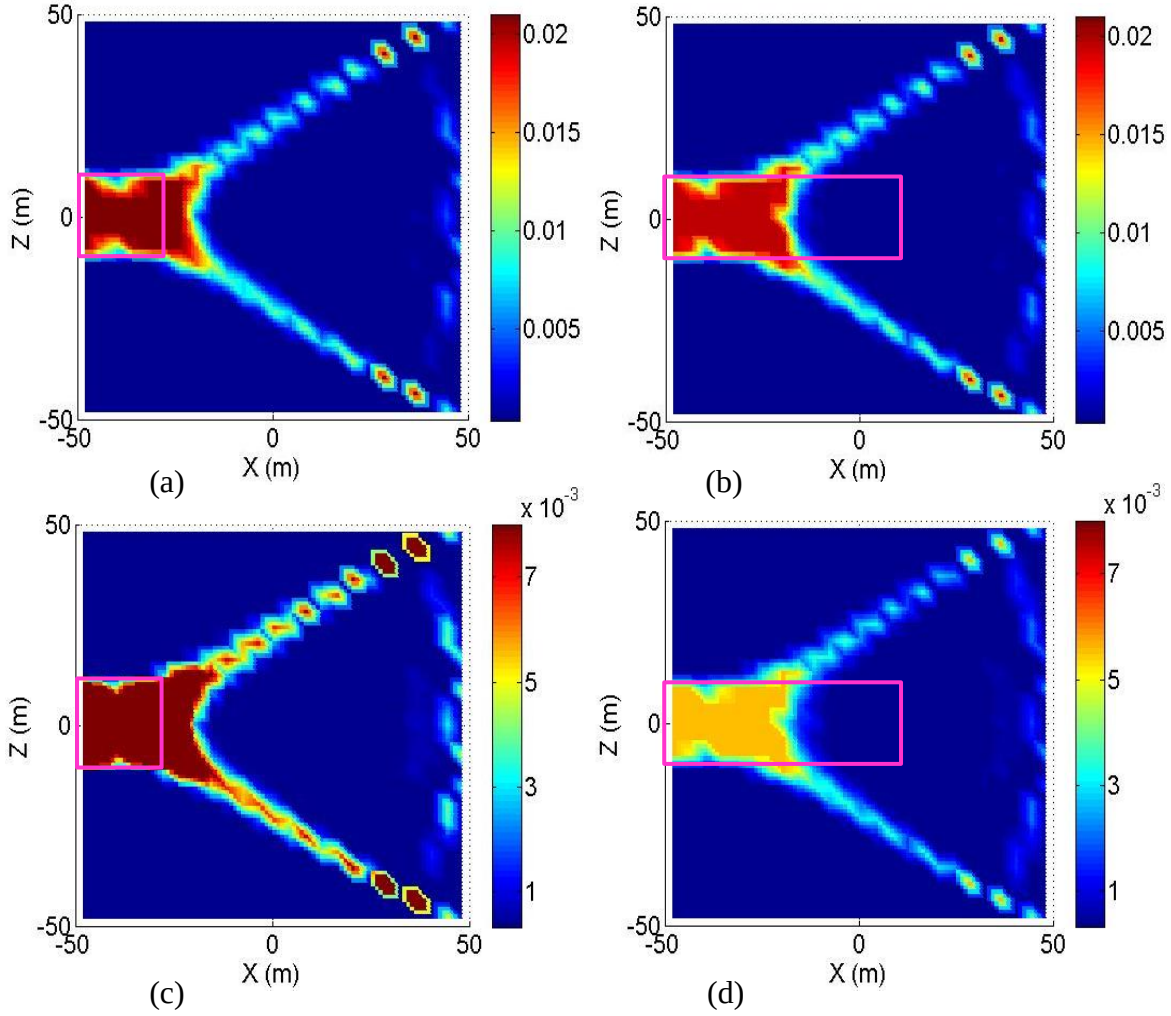

Figure 3-10. Amplitude tomograms of conductive zones of different length with 1 MHz (upper row) and 3 MHz (lower row) EM sources in the right borehole. (a) and (c): the conductive zone (purple outline) extends 20m from the left borehole; (b) and (d): the zone extends 60 m from the left borehole. The quantities on the colour bars are conductivities, with unit S/m.

Tomographic results of the amplitude data are shown in Figure 3-10. The positions where the receiver boreholes intersect with the conductive zone are apparent in all the cases. But, the lateral extent of the zones cannot be resolved (the conductive zones in all the images extend

about 30 m from the left borehole). The 1 MHz tomograms have a wider range of conductivity. There are diagonal artefacts from the edge of the zones to both ends of the transmitter borehole for all the cases, which are caused by lack of viewing angles at the top and bottom of the plane (Jackson and Tweeton, 1994).

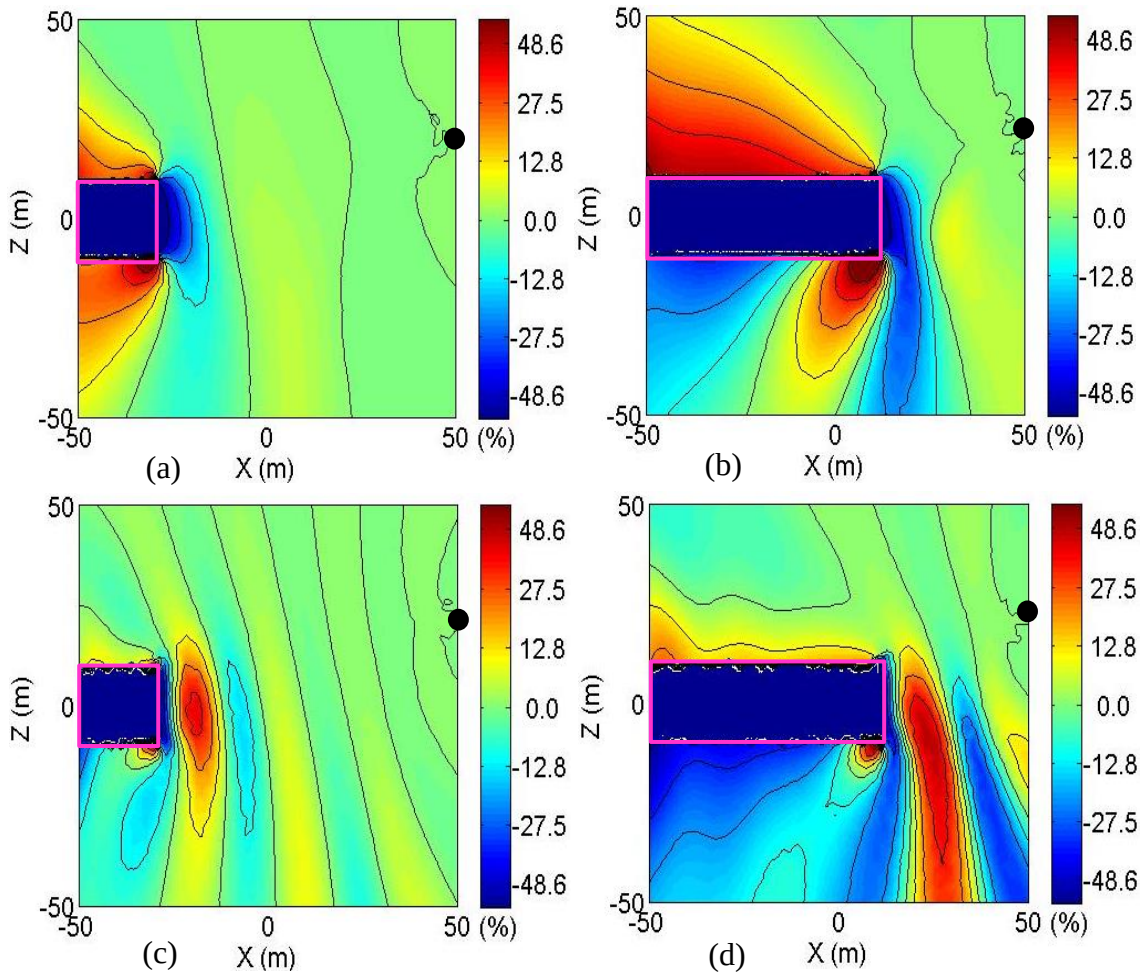

Figure 3-11 Amplitude-variation maps of the electric fields with the sources at (*x* = 50 m, *z* = 20 m) (black dots on the upper right of the tomograms are the transmitter locations). The frequency is 1 MHz for the upper row and 3 MHz for the lower row.

To study how the EM fields interact with the conductive zones, we plotted the amplitude variation maps for a source location at the point (x = 50 m, z = 20 m) for both frequencies and both extents (black dots on Figure 3-11). The areas inside the conductive zone show drastic attenuations, which are much stronger than the attenuations beneath the conductive zone. The straight-ray imaging method only accounts for the attenuation of the EM fields by the

conductors. The strong attenuations inside the conductive zone at the receiver position, which are similar for all cases, play the most dominant role in the imaging process, so the imaging results for all cases are similar.

Although the tomograms are similar in shape for all cases, the interaction between the EM wave and the conductors as well as the data along the receiver borehole, are somewhat different. The induction effects, which show an increase of the field (red) above and beneath the conductors, are stronger for lower frequency and/or closer to the source. For the 3 MHz cases, the induction effects is present around the right side of the conductive zone, and it is smaller in amplitude and restricted to a smaller area; the reflective waves, which interfere with the source field and show a wavy pattern between the source and the conductors (Li and Smith 2015), can be observed for both models (Figure 3-11c and d) at the higher frequency; for the tomogram with 70 m-extent conductor (Figure 3-11d), diffraction can be observed where the EM waves pass around the bottom right corner of the conductor, which shows EM field fluctuation beneath the conductor .

3.5 Discussions and conclusions

From the modelling and imaging studies at the transition between the diffusive regime and the propagation regime, we conclude that the characteristics of radio-frequency EM fields depend mainly on the wavelengths and the geometry of the borehole configuration. When a perfect conductor is less than one wavelength from the source, the induction fields play a major role on the data. In this situation, straight-ray phase tomography cannot recover the location of the conductor; but amplitude tomography can recover the location of the objects with simple geometries. When a conductor is more than two wavelengths away from the source, wave propagation effects play a major role on the data. In this situation, phase tomography works quite well if the absolute phase data can be recovered successfully;

however, amplitude tomography generates low-quality images with a conductive zone surrounding a more resistive zone at the centre of the conductor due to the diffraction phenomenon.

The far-field approximation is applicable more than about two wavelengths away from the source in the polar angle ranges between about -50 and +50 degrees. In this situation, the diffraction of EM waves around highly conductive objects causes retardation of the phase data, which is similar to the phase shift propagating inside moderate conductors, which explains why an anomaly can be recovered. For highly conductive bodies, the interactions of the radiation waves with the conductors mainly causes attenuation inside the conductors, and reflection and diffraction outside the conductors, which results in amplitude tomography providing low-quality images. Although in some circumstances amplitude tomography can recover the location of conductors of simple geometries and phase tomography can reconstruct the location and rough shape of conductors, the value of the reconstructed conductivities are just a few times higher than the background conductivity, which is much lower than the conductivities of most ore zones. Practitioner should be aware that the precise conductivity value cannot be recovered from the straight-ray tomograms.

From the imaging studies with reciprocal data generated for the L-shaped model, we found that, for noise-free data, the imaging results with the original data, the reciprocal data and the combined data set are similar; and the reciprocal data do not significantly improve the imaging qualities. However, for noisy phase data, imaging with the combined data set can suppress the impact of noise and improve the quality of the images somewhat, compared to those images generated with only one data set. This suggests that it is beneficial to collect the reciprocal data.

From the amplitude tomographic studies of the conductive models with different lateral extents, we found that the extents of the conductive zones cannot be imaged accurately. The imaging results for models with conductive zones of different lengths and using two different frequencies are similar, because the electric field attenuations at the receivers inside the conductor are so strong that their impact on the imaging was overwhelming. Practitioners should be aware that if a conductive zone is intersected by one hole, it is difficult to determine how far that conductive zone extends towards the other hole using straight-ray tomography.

Although imaging studies showed that we can recover the location and rough shape of conductors with phase tomography, the phase data are not always recovered successfully. For example, we did not show the phase tomograms in the imaging studies for conductors of different lateral extent, because highly conductive materials near the boreholes result in noisy data at the receivers, and thus the absolute phase data cannot be recovered. This is a limitation of phase tomography in many circumstances. As different-wavelength EM fields have different characteristics and the wavelength varies over a large range, it is necessary to investigate the wavelengths of the EM fields before carrying out a RIM survey. The wavelength depends on both frequency and electric properties (conductivity and relative permittivity) of the environment and we recommend that study of the local electric properties should be carried out.

From the experimental results in this paper, we conclude that the straight-ray attenuation model is not appropriate for describing the EM field distribution over the whole radio-frequency range. Even so, we acknowledge that the positions of conductor can be recovered in some limited conditions, which explains the results of some case studies (Thomson and Hinde 1993; Stevens *et al*. 2000). Hence, the straight-ray method can be used in appropriate

circumstances as a preliminary imaging method because of its fast processing time (the time consumed for each experiment in this paper is less than 10 seconds on a dual-core computer with the clock speed 2.6 GHz).

To better interpret RIM data, inversion algorithms based on the full EM solution would be a more generally applicable method, and development efforts in this direction should be expended. If there is a limitation on the computation time and an approximation of the EM field has to be used, we recommend using imaging methods that account for induction effects (e.g. Yu and Edwards 1997, MacLennan *et al*. 2013) to image the near-field data (less than one wavelength; lower frequencies); and for far-field data (more than two wavelengths away; high frequencies), we suggest using wave-based tomographic methods (e. g. Joachimowicz *et al.* 1991, Abubakar *et al*. 2002).

3.6 Acknowledgements

The authors express acknowledgments to the Natural Sciences and Engineering Research Council of Canada (NSERC), Vale, KGHM International, Sudbury Integrated Nickel Operations, A Glencore Company, Wallbridge Mining and the Centre for Excellence in Mining Innovation for sponsoring the research. We would also like to thank Peter Fullagar for interesting discussions and help in running the ImageWin program.

3.7 References

Abubakar A., Van den Berg P.M. and Mallorqui J.J. 2002. Imaging of biomedical data using a multiplicative regularized contrast source inversion method. *IEEE Transactions on Microwave Theory and Techniques* **50**, (7), 1761-1771.

COMSOL Multiphysics User Guide, 2012. Version 4.3 a, COMSOL AB, Stockholm, Sweden.

Devaney A. J. 1984. Geophysical diffraction tomography. *Geoscience and Remote Sensing, IEEE Transactions on* **GE-22**, (1), 3-13.

Dines K. A. and Lytle R. J. 1979. Computerized geophysical tomography. *Proceedings of the IEEE* **67**, (7), 1065-1073.

Hansen P. C. and Saxild-Hansen M. 2012. AIR tools—a MATLAB package of algebraic iterative reconstruction methods. *Journal of Computational and Applied Mathematics* **236**, (8), 2167-2178.

Hill D. 1984. Radio propagation in a coal seam and the inverse problem. *Journal of Research of the National Bureau of Standards* **89** (5), 385-394.

Huisman J. A., Hubbard S. S., Redman J. D. and Annan A. P. 2003. Measuring soil water content with ground penetrating radar. *Vadose zone journal* **2**, (4), 476-491.

Jackson M. J. and Tweeton D. R. 1994. *MIGRATOM: Geophysical tomography using wavefront migration and fuzzy constraints*. Report of Investigation, RI 9497. Bureau of Mines, United States Department of Interior.

Joachimowicz N., Pichot C. and Hugonin J. P. 1991. Inverse scattering: An iterative numerical method for electromagnetic imaging. *Antennas and Propagation, IEEE Transactions on* **39**, (12), 1742-1753.

Karimi-Sharif L. 2013. *Application of the cross-hole radio imaging method in detecting geological anomalies, Maclennan township, Sudbury Ontario*. Master Thesis, Laurentian University, Canada.

Korpisalo A. and Heikkinen E. 2014. Radiowave imaging research (RIM) for determining the electrical conductivity of the rock in borehole section OL-KR4− OL-KR10 at Olkiluoto, Finland. *Exploration Geophysics* **46**, (2), 141-152.

Korpisalo A. L. 2016. *Electromagnetic Geotomographic Research on Attenuating Material Using the Middle Radio Frequency Band*. PhD thesis, University of Helsinki, Finland.

Li Y. and Smith R. S. 2015. Forward modeling of radio imaging (RIM) data with the Comsol RF module. *Computers & Geosciences* **85**, 60-67.

MacLennan K., Karaoulis M. and Revil A. 2013. Complex conductivity tomography using low-frequency crosswell electromagnetic data. *Geophysics* **79**, (1), E23-E38.

McDowell G. M., Stewart R. and Monteiro R. N. 2007. In-mine Exploration and Delineation Using an Integrated Approach. *Proceedings of Exploration* **07**, 571-589.

Mutton A. J. 2000. The application of geophysics during evaluation of the Century zinc deposit. *Geophysics* **65**, (6), 1946-1960.

Naprstek T. and Smith R. 2016. SIRIM: an algorithm for forward modelling data from the radio imaging geophysical exploration method. Submitted to *Computers & Geosciences*.

Palacky G. J. 1987. Clay mapping using electromagnetic methods. *First Break* **5**, (8), 295-306.

Radcliff R. D. and Balanis C. 1979. Reconstruction algorithms for geophysical applications in noisy environments. *Proceedings of the IEEE* **67**, (7), 1060-1064.

Stevens K., Watts A. and Redko G. 2000. In-mine applications of the radio-wave method in the Sudbury igneous complex. In *2000 SEG Annual Meeting*. Expanded Abstracts, P1130.

Thomson S. and Hinde S. 1993. Bringing geophysics into the mine: radio attenuation imaging and mine geology. *Exploration Geophysics* **24**, (3-4), 805-810.

Ward S. H. and Hohmann G. W. 1988. Electromagnetic theory for geophysical applications. In: *Electromagnetic Methods in Applied Geophysics, Vol. 1*, (ed. M. N. Nabighian), pp. 131-311. Society of Exploration Geophysicists.

Wilkinson P. B. 2005. *Cross borehole electromagnetic tomography: scoping study and literature review*. British Geological Survey, Internal Report IR/05/146.

Ying L. 2006. Phase unwrapping. In: *Wiley Encyclopedia of Biomedical Engineering*, 1st Ed. (ed. Akay M.), pp. 1-12. Wiley-interscience.

Yu L. and Edwards R. N. 1997. On crosswell diffusive time-domain electromagnetic tomography. *Geophysical Journal International* **130**, (2), 449-459.

Yu L., Chouteau M., Boerner D. E. and Wang J. 1998. On the imaging of radio-frequency electromagnetic data for cross-borehole mineral exploration. *Geophysical Journal International*, **135**, (2), 523-541.

Chapter 4

4 Contrast source inversion (CSI) for cross-hole radio imaging (RIM) data - part 1: theory and synthetic studies[3]

4.1 Abstract

The 2D contrast source inversion (CSI) method is introduced for interpreting cross-hole radio imaging (RIM) data. The contrast source is defined as the product of the electric field and the object profile, the latter of which contains information about the conductivity and the permittivity of a model. We built a cost function and used the conjugate gradient iterative method to minimize the cost function by alternatively updating the contrast source and the object profile. We propose an equivalent 2D model as the background model, one of the input parameters in the inversion. To demonstrate the effectiveness of CSI, we applied the method to synthetic data generated from 3D models calculated with a finite element modelling package (Comsol Multiphysics). Specifically, we inverted a) data from a prismatic perfect conductor model, b) the same data with noise, c) the same data, but with transmitters only in a single borehole, d) the data from a model with an L-shaped perfect conductor. We conclude that isolated conductors between the holes can be identified with the inverted conductivity model. For the conductors larger than half the wavelength, the location and shape can be interpreted with confidence; for smaller conductors, the central location can be interpreted from the inverted conductivity. The modelling studies with the noisy data show that the CSI method is very robust to the existence of noise. The experiment with the transmitter location only in a single borehole shows that the single borehole data are not enough to provide satisfactory inversion results. From the synthetic studies, we infer that the conductivity values may not be correctly estimated from the inversion results. The inversion times for the data in

[3] Original manuscript accepted to be published in *Journal of Applied Geophysics*.

this paper are less than 20 minute for 200 iterations, which is reasonable and significantly less than the computation time for the 3D synthetic data.

4.2 Introduction

The radio imaging method (RIM) is a cross-hole exploration method which employs radio-frequency (typically 0.1 to 10 MHz) electromagnetic (EM) wave to image the electric properties on a plane between two boreholes. RIM can be applied to delineate ore bodies, detect mining hazards and select sites for underground nuclear waste disposal (Hill, 1984; Mutton, 2000; Korpisalo and Heikkinen, 2014). Currently, the straight-ray imaging method is the primary method used for RIM data interpretation (Dines and Lytle, 1979; Jackson and Tweeton, 1994; Korpisalo, 2016). Li and Smith (2015) modelled the RIM data with a finite element modelling package Comsol Multiphysics and assessed the straight-ray imaging method with synthetic data (Li and Smith, 2017a), which showed that the straight-ray method is not always appropriate for RIM data interpretation. The best results were obtained using phase tomography for the higher frequency range (1 to 10 MHz). However, in practise, the absolute phase data are difficult to recover, especially when the data are very noisy.

Compared with higher-frequency EM methods, such as ground penetrating radar which use the frequency range from 10 MHz to 1 GHz (Davis and Annan, 1989), the radio-frequency EM waves have lower frequencies and longer wavelengths. It is more appropriate to describe the radio-frequency EM problem as a back scattering problem, rather than a ray propagation problem. The EM back scattering inversion was developed in the 1990s and recently applied to microwave tomography in medical imaging for tumours diagnosis (Joachimowicz et al., 1991; Catapano et al., 2009). The back scattering inversion method is based on forward modelling the EM fields using the moment method (Gibson, 2014). The relation between model parameters and the modelled data is highly nonlinear.

There are currently two categories of back scattering inversion schemes. One category is based on the Gauss-Newton frame work: at each iteration, forward modelling is used to calculate the misfit between the measured data and the fitted data; and the Jacobian matrix is derived for modifying the model for the next iteration. The algorithm iterates until the data misfit is less than a predetermined threshold, and the latest model is the final result (Joachimowicz et al., 1991; Mojabi and LoVetri, 2009; Mojabi et al., 2011). Li and Smith (2016) used synthetic studies to demonstrate that this method can be applied to RIM data and it can provide better imaging results than the straight-ray method. Another category of back scattering inversion is based on the contrast source inversion (CSI) approach. By defining a contrast source to be the product of the object profile and the electric field, a cost function is built as the sum of two quadratic functions, which is easy to minimize. A full forward model is not required at each iteration, so it is computationally faster compared with the Gauss-Newton scheme (van den Berg and Kleinman, 1997; van den Berg et al., 1999; Abubakar, et al., 2002).

In this paper, we will introduce the contrast source inversion method for 2D interpretation of RIM data and demonstrate its effectiveness using 3D synthetic data calculated with Comsol Multiphysics (Li and Smith, 2015). In the next section (Section 4.3), we will describe the 2D back scattering problem, and describe how the CSI algorithm can be used to fit the transverse electric (TE) mode EM field. In our numerical experiments we generate synthetic data for a 3D model with a dipolar source, but the CSI method assumes a 2D model with an equivalent 2D source. There is an implicit assumption that the EM fields scattered by a conductor in 2D is similar the manner that a 3D conductor scatters fields. In Subsection 4.4.1, we will demonstrate that the EM fields of a 2D homogeneous model can be used to represent the EM fields of a 3D dipole source in a homogeneous background. An appropriate 2D model will be used as input parameters in the CSI inversion process. In Subsection 4.4.2 and 4.4.3, we will

study the synthetic models with a prismatic perfect conductor, for two transmitting frequencies (1 MHz and 3 MHz), and for data with and without noise.

We define the data with transmitters in one borehole and receivers in the other borehole as the data from transmitters in a single borehole, while the data with the transmitters and the receivers switched is defined as the reciprocal data. Li and Smith (2017a) showed that, for the straight-ray method, imaging with both data sets provide slightly better imaging result by suppressing the impact of noise comparing with the result of single data set. In Subsection 4.4.4, we will invert the data using a transmitter in a single borehole and compare with the results using both data sets. All the other experiments in this paper (except the one in Subsection 4.4.4) are conducted with both data sets.

To evaluate the effectiveness for models with more complicated geometry, in Subsection 4.4.5, we will carry out experiments for models with an L-shaped perfect conductor. In Subsection 4.4.6, we discuss the computation time for the synthetic studies in the paper.

In a companion paper (Li and Smith, 2017b) we generate synthetic data from a much more complicated model that closely mimics the situation often seen in Sudbury, Canada. The CSI image is then used as a guide to interpreting real data that has been inverted with the CSI method.

4.3 Methodology

4.3.1 Problem statement

In the cross-hole RIM configuration, two antennas are placed in two vertical or sub-vertical boreholes. We assume that two boreholes are on a 2D plane, and sometimes it is appropriate to treat this as a 2D problem. EM waves are transmitted from the antenna in one borehole and received by the antenna in the other borehole. The amplitude and phase of the electric fields

are the data measured by the antenna. The electric properties (the conductivity and the electric permittivity) of the materials on the borehole plane have an effect on the data and they are the parameters we are trying to estimate. We mesh the borehole plane with a grid (Figure 4-1). The electric properties and electric field within each cell are assumed to be uniform.

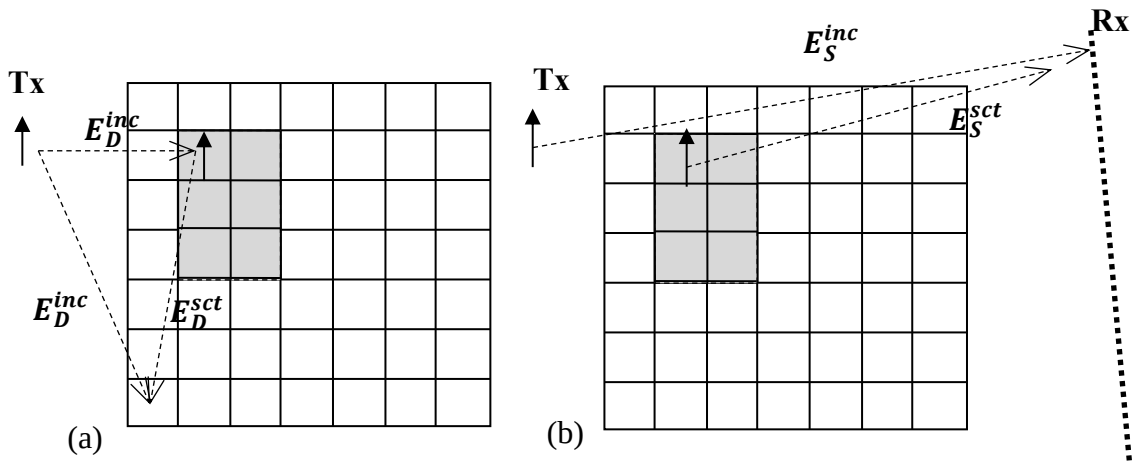

Figure 4-1. Discretization of a borehole plane for inversion. (a) Scattered field from a cell to another cell in the object domain D; (b) scattered field from a cell in the object domain D to a receiver location in the data domain S.

The total electric field vector $\boldsymbol{E}^{total}$ at any position $\boldsymbol{x}$ is decomposed to the incident field $\boldsymbol{E}^{inc}$ from the source and the scattered field $\boldsymbol{E}^{sct}$ from the model,

$$\boldsymbol{E}^{total}(\boldsymbol{x}) = \boldsymbol{E}^{inc}(\boldsymbol{x}) + \boldsymbol{E}^{sct}(\boldsymbol{x}), \tag{4-1}$$

The antennas are placed along the borehole trajectories, so the transmitted currents are on the borehole plane. We define the location of a transmitter as the origin of a spherical coordinate system, and the borehole as the polar axis. The distance from the transmitter to the receiver is the radial distance. The angle between the polar axis and the radial direction is the polar angle. The electric fields of the radiated EM waves at the receiver locations only have a polar component (within the borehole plane and perpendicular to the radial direction), there is no

radial and azimuthal component (perpendicular to the borehole plane). We followed Abubakar et al. (2002) and treat this as the TE mode of the electromagnetic problem. The relation between the scattered field from all the cells in the model and the total field $\boldsymbol{E}^{total}(\boldsymbol{x}')$ ($\boldsymbol{x}' \in D$, where D denotes the object domain) satisfies the integral equation (Joachimowicz et al., 1991; van den Berg et al., 1999),

$$\boldsymbol{E}^{sct}(\boldsymbol{x}) = (k_0^2 + \boldsymbol{\nabla}^R \boldsymbol{\nabla}^R) \int_D g(\boldsymbol{x} - \boldsymbol{x}') \chi(\boldsymbol{x}') \boldsymbol{E}^{total}(\boldsymbol{x}') dv(\boldsymbol{x}'), \tag{4-2}$$

where, g is the 2D Green's function for the transverse magnetic (TM) mode (the transmitting current is perpendicular with the 2D plane),

$$g(\mathbf{r}) = -\frac{i}{4} H_0^{(2)}(k_0|\mathbf{r}|)\,, \tag{4-3}$$

where, $H_0^{(2)}$ is the zero-order Hankel function of the second kind and $|\mathbf{r}|$ denote the radial distance; χ is the object profile,

$$\chi(\boldsymbol{x}) = (k^2(\boldsymbol{x}) - k_0^2)/k_0^2; \tag{4-4}$$

k is the wavenumber,

$$k^2(\boldsymbol{x}) = \mu\omega^2\epsilon(\boldsymbol{x}) - i\mu\omega\sigma(\boldsymbol{x}), \tag{4-5}$$

in which, μ is the magnetic permeability: in our studies, we assume $\mu \equiv 1.2566370614 \times 10^{-6}$ H/m; $\omega = 2\pi f$ is the angular frequency, where f is the transmitted frequency; $\epsilon = \epsilon_0\epsilon_r$ is the dielectric permittivity, where $\epsilon_0 = 8.854\,187\,817 \times 10^{-12}$ F/m and ϵ_r is the relative permittivity; σ is the conductivity; and k_0 denotes the background wavenumber.

By substituting equation (4-2) into equation (4-1), we can build equations for the total electric fields in all the cells in the object domain. If the electric properties of the model and the

incident field $\boldsymbol{E}^{inc}(\boldsymbol{x})$ are known, by solving the equations, we are forward modelling to calculate the total electric field for each cell in the object domain (Figure 4-1a). After that, we can use equation (4-2) to calculate the scattered electric fields at the receiver locations (Figure 4-1b).

However, these equations for the total fields in the model domain are highly nonlinear. To find a solution directly is very time-consuming. To speed up the solution, we introduce the contrast source inversion method.

4.3.2 Contrast source inversion

Firstly, we follow Abubakar et al. (2002) and define simpler notations for equation (4-1) and (4-2). Using equation (4-2), we can write the scattered field f_i at the receiver locations observed in a borehole (data domain *S*) excited by a number of incident fields $u_i^{inc}, i = 1,2, \ldots . I$ (where I is the number of transmitter locations) as

$$f_i = G_S \chi u_i^{total}, \qquad \boldsymbol{x} \in S, \tag{4-6}$$

where, G_S is a matrix, each element of which is the Green's function with the source in the object domain and the receiver in the data domain; u_i^{total} is the total electric field $\boldsymbol{E}^{total}(\boldsymbol{x})$ in the object domain D for the i^{th} transmitter location. The equation involving the total fields in the object domain can be derived by substituting equation (4-2) into equation (4-1),

$$u_i^{inc} = u_i^{total} - G_D \chi u_i^{total}, \quad \boldsymbol{x} \in D. \tag{4-7}$$

where, G_D is a matrix, each element of which is the Green's function with both the source and the receiver in the object domain. Now, the problem is to find χ in the object domain *D* for given f_i in the data domain *S*, subject to the condition that χ and u_i^{total} in *D* satisfy equation (4-7).

We define the contrast source as,

$$w_i(\boldsymbol{x}) = \chi(\boldsymbol{x}) u_i^{total}(\boldsymbol{x}), \tag{4-8}$$

which is the equivalent coupling current that produce the scattered electric fields. Equation (4-6) and (4-7) then become

$$f_i = G_S w_i, \qquad \boldsymbol{x} \in S \tag{4-9}$$

$$\chi u_i^{inc} = w_i - \chi G_D w_i, \qquad \boldsymbol{x} \in D. \tag{4-10}$$

We define the cost function as,

$$F_n(w, \chi) = \eta^S \sum_i \| f_i - G_S w_i \|_S^2 + \eta^D \sum_i \left\| \chi u_i^{inc} - w_i + \chi G_D w_i \right\|_D^2 \tag{4-11}$$

where, the subscript n denotes the iteration. The first part at the right of equation (4-11) is the data cost function $F^S(w)$; the second part is the object cost function $F^D(w, \chi)$. The normalization factors η^S and η^D are,

$$\eta^S = \left(\sum_i \| f_i \|_S^2 \right)^{-1}, \tag{4-12}$$

$$\eta^D = \left(\sum_i \left\| \chi_{n-1} u_i^{inc} \right\|_D^2 \right)^{-1}. \tag{4-13}$$

Equation (4-11) is a quadratic function. We use the conjugate gradient iterative method to minimize equation (4-11) (van den Berg et al., 1999). For each iteration, we update the contrast source w and the object profile χ alternatively. The process is described in Appendix A.

For the TE mode of the 2D electromagnetic problem, we use the dyadic Green's function to calculate the electric field from the transmitters, which is $G(\boldsymbol{r}) = (k_0^2 + \nabla^2)\, g(\boldsymbol{r})$ in equation (4-2), whose explicit form is given in Appendix B. To calculate the scattered field from a grid cell, we need to integrate the Green's function over that cell. This technique was developed by Kooij and van den Berg (1998), and is described in Appendix B.

4.4 Modelling studies

4.4.1 Equivalent 2D model and transmitting source

We build models with two 100 m-long vertical boreholes, which are 100 m apart. The centre location of two boreholes is defined as the origin of a Cartesian coordinate system (see Figure 4-4). The *x*-axis is from left to right, the *z*-axis from down to up, and the *y*-axis perpendicular to the borehole plane (the *y*-axis is not shown in the inversion results). We calculate the EM fields in one borehole with a 3D electric-dipole transmitter in the other borehole using equation (2-1) and (2-2), which assumes a homogeneous whole space (Naprstek and Smith, 2016; Li and Smith, 2017a). We model the electric fields of a 2D point source (line source in 3D) in a homogeneous whole space model with the dyadic Green's function (Appendix B). By adjusting the source strength (dipole moment), the conductivity and the permittivity of the model, we use the data from a 2D source to fit the data from a 3D dipole.

We show examples of a homogeneous whole-space model ($\sigma = 0.0003$ S/m, $\varepsilon_r = 6$ and a vertical-dipole source with moment $Ids = 1$ Am) with two different transmitting frequencies for f = 1 MHz and f = 3 MHz. Table 4-1 shows the model parameters for the 3D and the 2D models. The amplitude and the phase data along the receiver borehole with the transmitters at (*x*, *z*) = (-50, -35) and (-50, -5) in the transmitter borehole for f = 1 MHz are shown in Figure 4-2; the data for f = 3 MHz are in Figure 4-3. We can see that the data of the 2D whole-space model fit those of the 3D whole-space model quite well for both frequencies. The 2D model

parameters in Table 4-1 will be used as inputs in the inversion for the following modelling studies.

These experiments tell us that it is not difficult to adjust the parameters of a 2D homogeneous whole-space model to fit 3D data. Empirically, the phase data are mainly affected by the permittivity; the amplitude data are mainly affected by the dipole moment and the conductivity. The dipole moment affects the magnitude of the amplitude data only, while the conductivity affects both the magnitude and the shape of the data (Naprstek and Smith, 2016).

Table 4-1. Equivalent 2D models for 3D homogeneous whole-space models; and the wavelengths and the element sizes for discretizing the background of the 3D models for forward modelling.

	1 MHz		3 MHz	
Source type	3D	2D	3D	2D
Conductivity σ (S/m)	0.0003	0.000285	0.0003	0.00024
Relative permittivity ε_r	6	4.6	6	5.5
Dipole moment Ids (Am)	1	0.01	1	0.01
Wavelength (m)	113.0		40.4	
Maximum element size (m)	6		5	

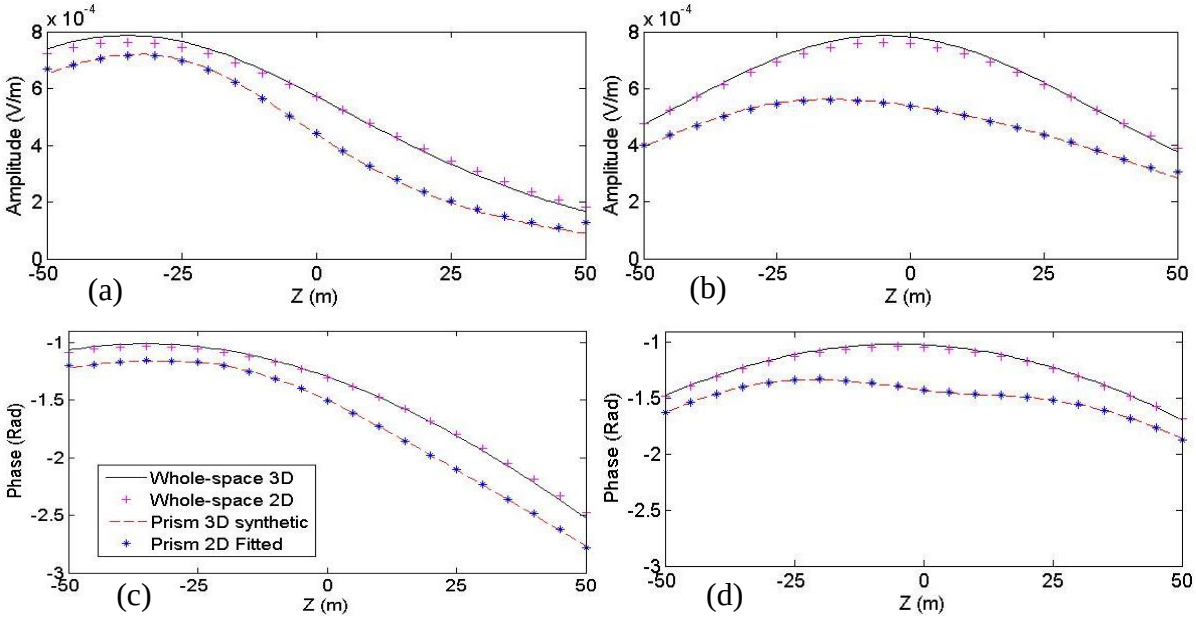

Figure 4-2. Electric fields of a 1 MHz 2D source to fit the fields of a 3D dipole source in a homogeneous whole-space model, and data of the 3D prismatic conductor model (Prism 3D synthetic) and the 2D inverted model: (a) amplitude data with the source at (x, z) = (-50, -35), (b) amplitude data with the source at (x, z) = (-50, -5), (c) phase data with the source at (x, z) = (-50, -35) and (d) phase data with the source at (x, z) = (-50, -5).

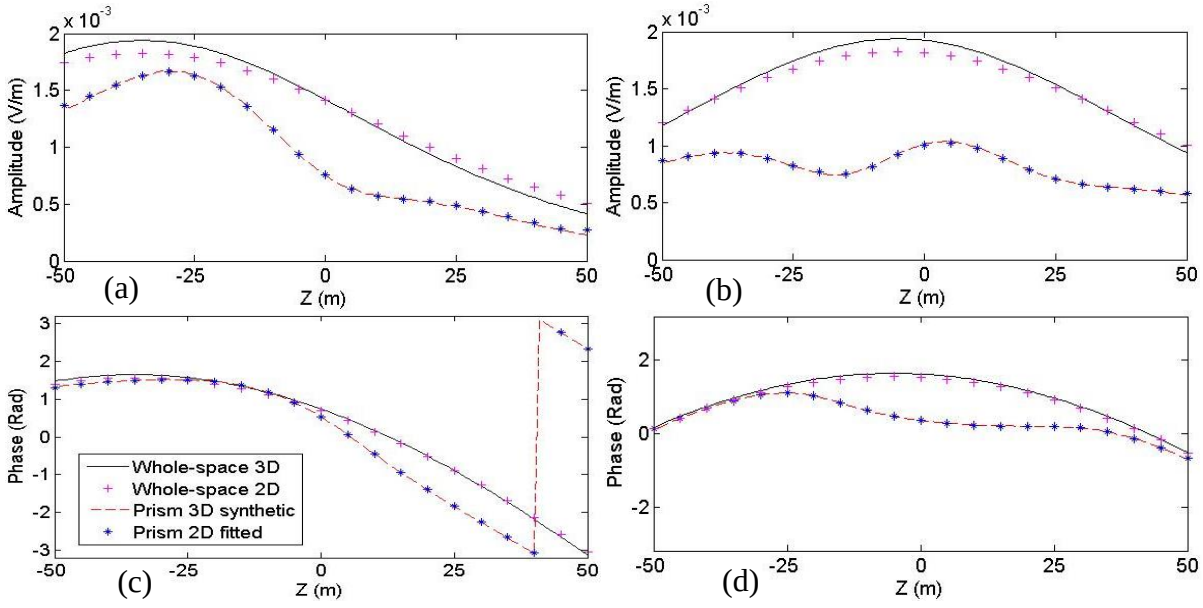

Figure 4-3. Electric fields of a 3 MHz 2D source to fit the fields of a 3D dipole source in a homogeneous whole-space model, and data of the 3D prismatic conductor model (Prism 3D synthetic) and the 2D inverted model: (a) amplitude data with the source at (x, z) = (-50, -35),

(b) amplitude data with the source at (x, z) = (-50, -5), (c) phase data with the source at (x, z) = (-50, -35) and (d) phase data with the source at (x, z) = (-50, -5).

4.4.2 Prismatic conductor with a frequency of 3 MHz

We constructed a 3D numerical model with a prismatic conductor at the centre of the borehole plane. The conductor has dimensions of 30 m × 20 m × 40 m (from x = -15 m to x = 15 m, from z = -10 m to z = 10 m, and from y = -20 m to y = 20 m). The intersections of the prism with the borehole plane are shown as pink outlines in Figure 4-4a and b. The prism is a perfect conductor, in a homogeneous background of σ = 0.0003 S/m. The relative permittivity is 6 for the whole model, as well as the models in the following subsections. We put a 3D point source at various locations in one borehole, and calculate the electric fields along the other borehole. To simulate a RIM survey, we modelled the data for transmitters every 5 m along the borehole, and we switched the transmitter borehole with the receiver borehole position to get the reciprocal data (Li and Smith, 2017a). In this case, the transmitter frequency is 3 MHz. The wavelength of the EM waves in the background material is 40.4 m (Ward and Hohmann 1988; Li and Smith 2017a). The "domain of interest" is defined as a larger prism that included the two boreholes and the conductor (in Cartesian coordinates the domain of interest goes from x = -50 m to x = 50 m, from z = -50 m to z = 50 m and from y = -20 m to z = 20 m) and is meshed with tetrahedral elements whose maximum edge length is 5 m (Table 4-1). This element size is selected to meet the requirement of more than 8 elements per wavelength, in order to achieve a modelling error less than 1% (Li and Smith 2015). The areas outside of the domain of interest are meshed with larger elements, because the element size in these domains does not significantly affect the modelling precision. Inside the prismatic conductor, the element size is not critical due to the boundary condition on the perfect conductor (Li and Smith, 2017a). We show the synthetic data of two transmitter positions at (x, z) = (-50, -35) and (-50, -5) in Figure 4-3. The phase data are retarded by the

conductor; the amplitude data are attenuated and diffraction is evident as the relatively strengthened electric fields behind the conductor (the relative maximum on Figure 4-3b at approximately z = 5 m surrounded by two minima). Detailed discussions of the EM field characteristics around a perfect conductor can be found in Li and Smith (2017a).

For the inversion, the borehole plane is meshed with 625 4 m × 4 m square cells (this cell size will be used for all the following models). Using the equivalent 2D model parameters in Table 4-1, we inverted the synthetic 3D data. The inversion adjusts the complex object profile, from which we can calculate the conductivity and the permittivity of the model. The starting values are calculated with the back propagation method (see Appendix A). Figure 4-4a, c and e show the conductivity, the permittivity and the magnitude of the object profile (χ) of the starting model respectively. Figure 4-4b, d and f show the conductivity, the permittivity and the magnitude of object profile of the inverted model after 200 iterations, respectively.

The starting model shows a slightly higher conductivity and lower permittivity at the position of the prismatic conductor (Figure 4-4a and c). The inverted conductivity model (Figure 4-4b) shows the position and the shape of the prism pretty well. The maximum conductivity in the inverted model is around 0.0012 S/m, which is four times the background conductivity. There are low conductivity artefacts (about 0.0002 S/m, slightly lower than the background) above and beneath the conductor. The inverted permittivity model (Figure 4-4d) shows lower permittivity at the position of the conductor and the higher permittivity above and beneath the conductor. The highest permittivity and the lowest permittivity in the inverted model are 7 and 3 respectively. Although the inverted permittivity model should be constant at 5.5, the fluctuation of the permittivity is smaller than the variations in the inverted conductivity. Figure 4-4f shows the inverted magnitude of the object profile, which is the combined effect

of the conductivity and the permittivity. There is a high anomaly at the position of the conductor at Figure 4-4f, but the shape is not prismatic and the magnitude is not large enough.

To investigate how the modelled data fit the synthetic data, we show the convergence of the cost functions in Figure 4-5a. The cost function ($F_n(w,\chi)$ in Equation (4-11)) is shown as a black solid line (total cost), which is the combination of the data cost function $F^S(w)$ (red dash-dotted line and the object cost function $F^D(w,\chi)$ (blue dashed line). The data cost function shows how the modelled data from the contrast sources fit the synthetic data. The object cost function shows how the object profile fit the contrast sources for all the transmitting locations. The total cost function describes the combination of the two costs. In Figure 4-5a, the cost functions decrease continuously, and after 150 iterations, the cost functions tend to be quite stable. The total cost function is mainly from the object cost function. The object cost function is higher than the data cost function after 5 iterations. The cost functions shown in Figure 4-5a indicate that the modelled data for all transmitter locations fit the synthetic data quite well. This argument is verified with the data shown in Figure 4-3, where the modelled data for two transmitter locations fit the synthetic data very well. In comparison, the object profile does not fit the contrast sources very well. Techniques for constraining the model when updating the object profile may be helpful to improve the inversion results, which requires further study.

From this modelling study, the CSI algorithm seems to be able to invert the RIM data. We can use the inverted conductivity model to interpret the location and the shape of a highly conductive object.

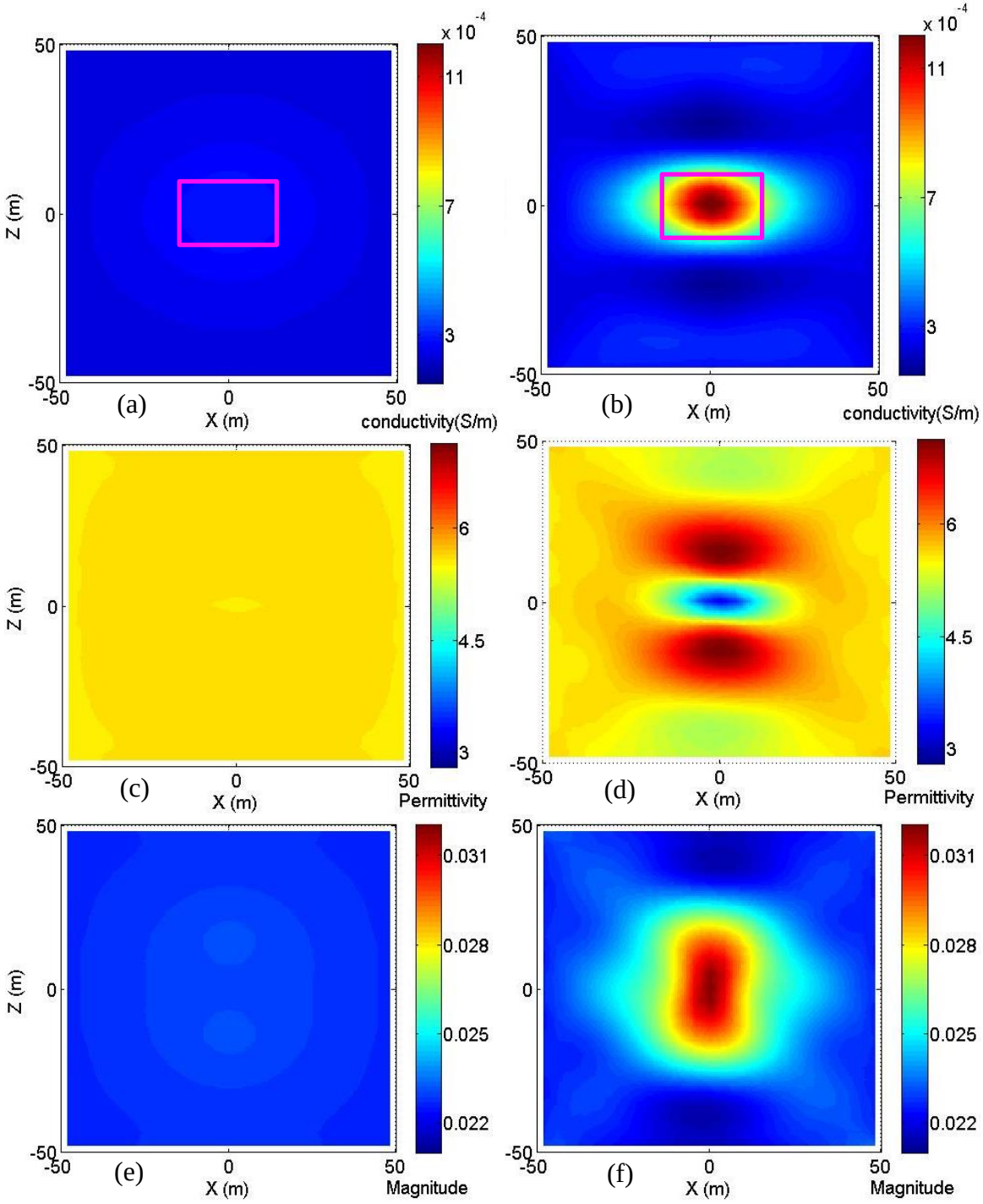

Figure 4-4. Starting models and inverted models for the synthetic data of the 3D model with a prismatic conductor (pink outlines in (a) and (b)) with f = 3 MHz: (a) starting conductivity model, (b) inverted conductivity model, (c) starting permittivity model, (d) inverted permittivity model, (e) starting magnitude of object profile and (f) inverted magnitude of object profile.

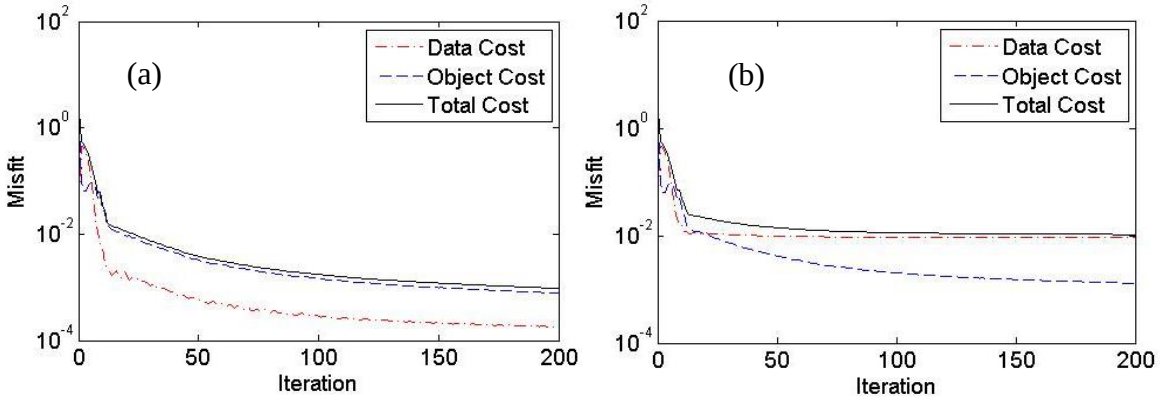

Figure 4-5. Cost functions over 200 iterations for the synthetic data without (a) and with noise (b) of the model with a prismatic conductor for f = 3 MHz.

4.4.3 Result of 1 MHz and data with noise

We study the same model as in Subsection 4.4.2, but for f = 1 MHz.The wavelength in the background is 113.04 m and we use elements with the maximum edge length of 6 m to discretize the domain of interest in Comsol in order to meet the requirements of more than 8 elements per wavelength and having enough data points along the receiver borehole. All other parameters are the same as the previous example. We show the noise-free synthetic data for two transmitter positions at (x, z) = (-50, -35) and (-50, -5) in Figure 4-2, where the amplitude attenuation and the phase retardation by the perfect conductor are evident. The perfect conductor results in a smaller variation in the data at a frequency of 1 MHz compared with those of 3 MHz (Figure 4-3). Li and Smith (2017a) showed that EM induction plays a major role in the EM field interaction with the conductor for this model. Theoretically, the CSI method is based on the TE mode of the propagation fields, so it is not appropriate for the model at 1 MHz. Here, we include this model to show the effectiveness of the CSI method when the induction fields are significant.

We use the CSI algorithm to invert the synthetic data, but only show the inverted conductivity for 1 MHz data in Figure 4-6a. For comparison, the inverted conductivity for 3MHz is shown in Figure 4-6b, and we use the same colour bar for both Figure 4-6a and b.

Figure 4-6a shows a conductive region at the correct position, but the values are not as large as those on Figure 4-6b and the shape of the region is more circular. Hence, the shape of the conductor cannot be correctly interpreted from the inversion result. According to the Rayleigh criterion, the smallest objects that can be resolved with EM waves are those with dimension larger than half of the wavelength (Abubakar et al., 2002). Considering the wavelength for 1 MHz is 113.04 m, the dimension of the perfect conductor is only a fraction of half of the wavelength, while the example of 3 MHz meets the Rayleigh criterion. Therefore, the inversion result for 1 MHz is reasonable, and not as good as the one for 3 MHz.

Another reason why the inversion result for 3 MHz is better than the one for 1 MHz can be seen by comparing the synthetic data in Figure 4-2 and Figure 4-3. The anomalies in both amplitude and phase caused by the conductor are greater for 3 MHz than the anomalies for 1 MHz, so there is greater information about the target in the data of 3 MHz.

The experiments of the models with a prismatic conductor for 1 MHz and 3 MHz suggest the quality of inversion result is related to the ratio of the wavelength to the size of the conductor: the method is suitable to image a conductor larger than half the wavelength. Even so, the inversion result for 1 MHz (Figure 4-6a) implies that we might be able to find conductors smaller than half wavelength with the CSI method, but a strong anomaly and the correct shape should not be expected.

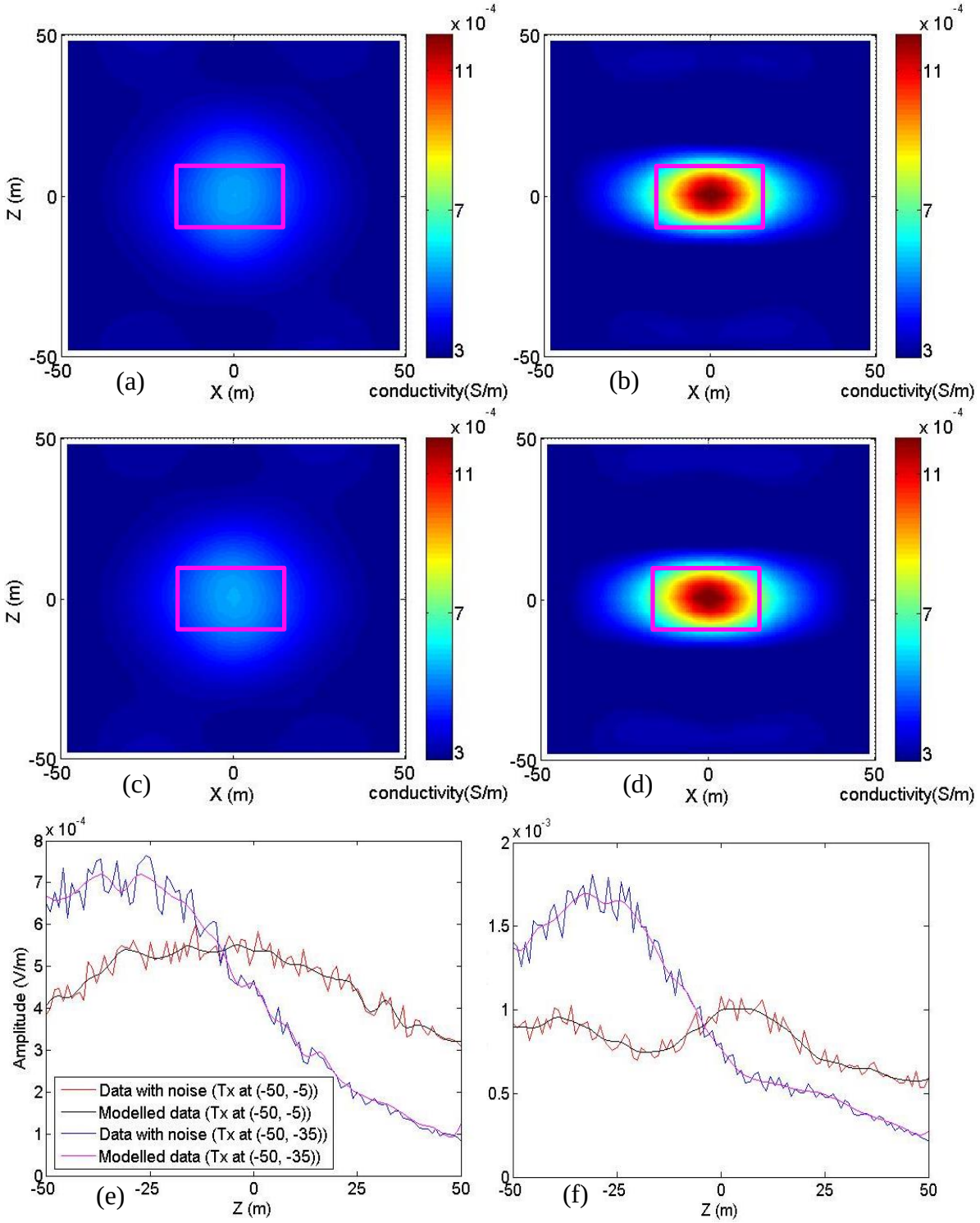

Figure 4-6. Inverted conductivity models for (a) the data of f = 1MHz, (b) for the data of f = 3MHz, (c) for the 1 MHz data with 10% noise, (d) for the 3 MHz data with 10% noise; synthetic and modelled amplitude data (e) for f = 1MHz and (f) for f = 3MHz with transmitters at (x, z) = (-50, -5) and (-50, -35).

To investigate the robustness of the CSI algorithm against noise, we add random noises to both the amplitude and the phase data of 1 MHz and 3 MHz. We assume that the noise is multiplicative, so we add random noise that varies by as much as 10% of the synthetic data. We show the synthetic amplitude data with noise ("Data with noise" in the legends) of both frequencies for two transmitter locations at (x, z) = (-50, -5) and (-50, -35) in Figure 4-6e (1 MHz) and Figure 4-6f (3 MHz). The quality of data is severely deteriorated by adding the noise.

We inverted the noisy data with the CSI method. The inverted conductivity models after 200 iterations for both frequencies are shown in Figure 4-6c (1 MHz) and Figure 4-6d (3 MHz). Comparing Figure 4-6c and d with Figure 4-6a and b, no significant changes can be observed in the inverted conductivity models after adding noises. We show the modelled data, which are used to fit the noisy synthetic data, for both frequencies with transmitters at the corresponding locations in Figure 4-6e and f. We can see from Figure 4-6e and f that, though the input data (Data with noise) for inversion are quite noisy, the modelled data are smoother in shape. The modelled data have not removed the noise, so the fitted data does not look like the amplitude data on Figure 4-2 and Figure 4-3. However, the CSI algorithm is trying to fit the broad features of the input data, rather than every spike in the input data.

To better understand the inversion process, we show the convergence of the cost function over 200 iterations for the 3 MHz data with noise in Figure 4-5b. Compared with the one for data without noise (Figure 4-5a), the object cost functions converge in a similar way, while the data cost functions are different. The data cost function for noisy data converge to around 0.01 by ten iterations and does decrease further. We interpret that the noises in the data cause a larger misfit between the contrast sources and the data. However, the noise does not affect the misfit between the contrast sources and the object profile. The effect of noise appears to

be averaged over the transmitters during the process of updating the contrast source (Appendix A), so the noise does not affect the object profile significantly. From our examples, we conclude that the CSI algorithm is very robust to the existence of noise.

4.4.4 Data from a single borehole

The CSI algorithm is used to invert the 3 MHz single borehole data (with the transmitters in the right borehole and the receivers in the left borehole) for the same model as above. The starting conductivity model and the inverted conductivity model after 200 iterations are shown in Figure 4-7a and b. The starting conductivity model with single borehole data shows a slightly more conductive region close to the centre of the left borehole. The inverted conductivity model shows three conductive areas close to the left hole. From the inverted conductivity image, it is difficult to correctly interpret the position and the shape of the prismatic conductor. Compared with the inversion results of data from both boreholes (Figure 4-4a and b), single borehole data does not provide satisfactory inversion results.

For the straight-ray method, imaging with both data sets (single and reciprocal) provided slightly improved inversion result by suppressing the impact of noise comparing with the result of the single data set (Li and Smith 2017a). For the CSI algorithm, data of the single borehole are insufficient to provide good inversion results. This is possibly because there are more variables (conductivity and permittivity) in the CSI algorithm compared with the straight-ray method (only attenuation rate). The reciprocal data from another borehole are indispensable information to get a reasonable inversion result with the CSI method.

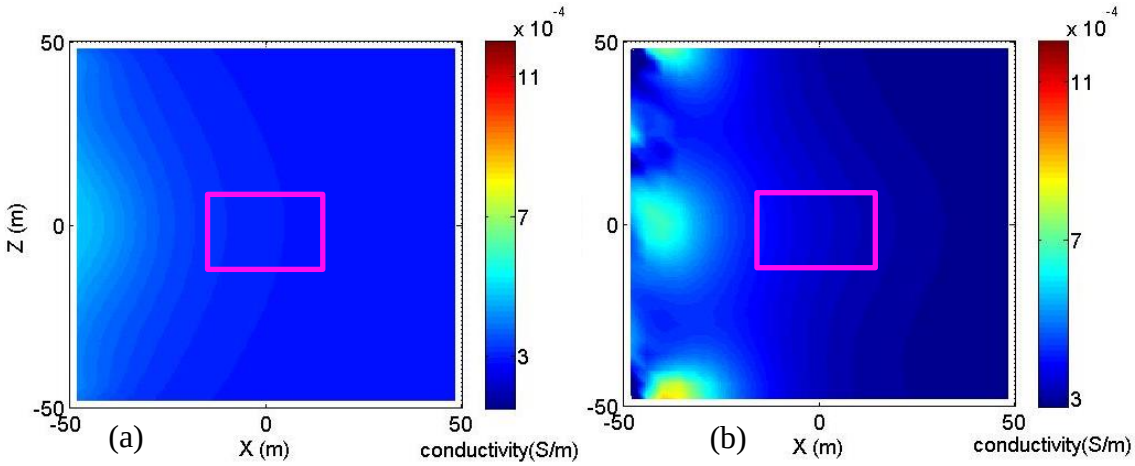

Figure 4-7. Starting conductivity model (a) and inverted conductivity model (b) for the model with a prismatic conductor (pink outlines) using the 3 MHz data with transmitters in the right borehole and receivers in the left borehole only.

4.4.5 L-shaped conductor

The effectiveness of CSI method for a more complicated model is evaluated by building an L-shaped conductor model between two boreholes. The borehole configuration is the same as the previous example, but the conductor is constructed by cutting a small prism 25 m × 25 m × 40 m from a cube that is 40 m × 40 m × 40 m, so its intersection with the borehole plane is an L-shaped polygon (pink outlines in Figure 4-8). The background conductivity is 0.0003 S/m. The conductor is a perfect conductor. We use the same discretization parameters as shown in Table 4-1 to mesh the domain of interest, and calculate the synthetic data for 1 MHz and 3 MHz.

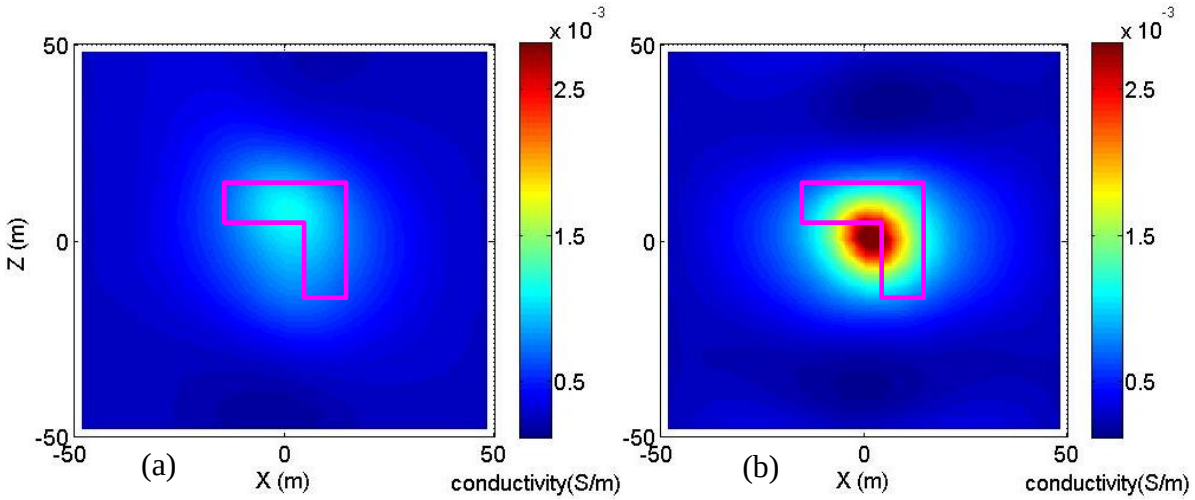

Figure 4-8. Inverted conductivity of the models with an L-shaped conductor for f = 1 MHz (a) and f = 3 MHz (b).

The inverted conductivity models are shown in Figure 4-8 for 1 MHz (Figure 4-8a) and 3 MHz (Figure 4-8b). The lower limit of the colour bars is set to be 0.0002 S/m, and the upper limit is 0.0027 S/m, which is 9 times the background conductivity. We can see conductive areas on both inverted conductivity models. The 3 MHz result (Figure 4-8b) has a higher magnitude for the inverted conductivity. If the 0.0015 S/m contour (green), where a sharp change is observed, is interpreted to be the boundary of the conductor, the ends of the conductor at three edges are in the correct position. The missing corner of the L-shaped conductor is not very well resolved, which is shown as an arc distorted slightly inward from a circle.

For the 1 MHz result (Figure 4-8a), the inverted conductivity has a weaker magnitude and is broader in shape. The highest conductivity is around 0.0012 S/m, which is actually quite strong if we compare this with the results for the models with a prismatic conductor (Figure 4-6a and b). It is difficult to interpret the boundaries of the conductor from the inversion result, but the upper left and the lower right areas are slightly more conductive, which is somewhat the correct shape of conductor. Although the Rayleigh criterion is not meet for 1

MHz data, we argue that the inverted conductivity model is helpful to infer the features of the conductors.

4.4.6 Computation times

The computation time of the CSI algorithm presented in this paper depends on a number of factors: the number of transmitter locations, the number of receiver locations for each transmitter, the number of cells in the model and the number of iterations. The compiler and computer hardware also effect the run times.

We developed the contrast source inversion codes in C# and implemented the inversion on a dual-core computer with a clock speed of 2.6 GHz. For the models with a prismatic conductor or an L-shaped conductor, it takes 17 to 18 minutes to execute an inversion that has 200 iterations and is inverted for both data sets. If a single or reciprocal data set (alone) is being inverted it takes roughly half the time, 8 to 9 minutes.

These run times should be compared to the 3D forward modelling with Comsol, which takes around 30 minutes to model the data from only one transmitter location on an 8-core computer with a clock speed of 2.6 GHz (the whole data set includes data of 42 transmitter locations).

We argue the presented CSI method is quite fast and it is affordable to use this method to invert the RIM data. If the Comsol modelling was used as the forward modelling in an inversion algorithm, the algorithm would be nowhere near as fast.

4.5 Conclusions

The contrast source 2D inversion method can be used for inverting cross-hole RIM data generated from a 3D model. This requires some preliminary fitting to determine the

conductivity, permittivity and the dipole moment of an effective 2D source that can explain the 3D data.

An experiment with a prismatic perfect conductor using a transmitting frequency of 3 MHz shows that the inversion converges and we can successfully interpret the location and the shape of a highly conductive object from the inverted conductivity. We studied the same model for a transmitter frequency of 1 MHz and found out that the resolution in the inverted conductivity result depends on the size of the conductor compared to the wavelength. An object with its size larger than half of the wavelength can be imaged successfully using the CSI method; while an object smaller than half of the wavelength can also be identified, but the shape cannot be interpreted with confidence. Experiments that added 10 % noise to the above datasets show that the presence of noise does not significantly affect the inversion results, so the CSI method is very robust to the presence of noise.

An inversion using a single borehole data set was significantly worse than an inversion that also included a reciprocal data set.

A data set generated with an L-shaped perfect conductor at transmitting frequencies of both 1 MHz and 3 MHz showed that in the 3 MHz case, the rough boundaries of three edges of the conductor can be identified, but it is hard to interpret the exact shape of the smaller features. For the 1 MHz, the edges of the conductor are more diffuse, but an overall orientation (from bottom right to top left) can be identified.

In the synthetic studies, we used perfect conductor to represent highly conductive anomalies with conductivity higher than 1 S/m. However, the inverted conductivity values are only a few times higher than the background. The inverted conductivity values are higher with higher-frequency data. We infer that it is difficult to interpret the correct conductivity values

from the inversion results. The run times for the experiments in this paper are very reasonable and will mean that the CSI method will be practical for RIM data inversion.

There are limitations on the 2D CSI method. The 2D assumption means that there is a preliminary step to estimate the parameters of the 2D model that can simulate the 3D data of the background model. This means that a background model has to be selected. If the incorrect background is selected, then the results could be different. The 2D assumption can be invalid in reality, such as the presence of an asymmetric model (asymmetric across the borehole plane). Of course, more appropriate models are 2.5D models (2D model and 3D source) and 3D models.

Even so, the modelling studies in this paper are very encouraging, which indicate that using radio-frequency EM waves for cross-hole exploration can provide high resolution imaging results. The features that can be identified using transmitters and receivers on either side of the zone of interest are much more detailed than that are normally seen when the transmitters and the receivers are on the surface. The CSI method can be extended to 3D using different Green's functions (Joachimowicz et al., 1991; Abubakar, et al., 2002). However, 3D inversion requires information from more than two boreholes. To our knowledge, the instruments available to the mining industry only have one transmitter and one receiver. More versatile instruments with multiple receivers, which can be used to receive signals in multiple boreholes, are required and we encourage the development of such tools.

Advantages of the proposed 2D CSI method as applied to RIM data are its easy implementation, and fast solution, which makes it practical for fast interpretation. Even for the 3D inversion, this method could be used to build a starting model.

4.6 Acknowledgements

The authors express acknowledgments to the Natural Sciences and Engineering Research Council of Canada (NSERC), Vale, KGHM International, Sudbury Integrated Nickel Operations -- A Glencore Company, Wallbridge Mining and the Centre for Excellence in Mining Innovation for funding this research.

4.7 References

Abubakar, A., van den Berg, P.M. and Mallorqui, J.J., 2002. Imaging of biomedical data using a multiplicative regularized contrast source inversion method. *IEEE Transactions on Microwave Theory and Techniques*, **50**(7), 1761-1771. doi: 10.1109/TMTT.2002.800427.

Catapano, I., Di Donato, L., Crocco, L., Bucci, O. M., Morabito, A. F., Isernia, T. and Massa, R., 2009. On quantitative microwave tomography of female breast. *Progress in Electromagnetics Research*, **97**, 75-93. doi: 10.2528/PIER09080604.

Davis, J. L. and Annan, A. P., 1989. Ground-penetrating radar for high-resolution mapping of soil and rock stratigraphy. *Geophysical prospecting*, **37**(5), 531-551. doi: 10.1111/j.1365-2478.1989.tb02221.x.

Dines, K. A. and Lytle, R. J., 1979. Computerized geophysical tomography. *Proceedings of the IEEE*, **67**(7), 1065-1073. doi: 10.1109/PROC.1979.11390.

Gibson, W. C., 2014. *The method of moments in electromagnetics*. CRC press. doi: 10.1080/001075109030 73302.

Hill, D., 1984. Radio propagation in a coal seam and the inverse problem. *Journal of Research of the National Bureau of Standards*, **89**(5), 385-394. doi: 10.6028/jres.089.022.

Jackson, M.J. and Tweeton, D.R., 1994. *MIGRATOM—Geophysical tomography using wavefront migration and fuzzy constraints*. Report of Investigations RI9497, Department of Interior, US Bureau of Mines, Minneapolis, MN, USA, 41 pp.

Joachimowicz, N., Pichot, C. and Hugonin, J. P., 1991. Inverse scattering: An iterative numerical method for electromagnetic imaging. *IEEE Transactions on Antennas and Propagation*, **39**(12), 1742-1753. doi: 10.1109/8.121595.

Kleinman, R. E. and van den Berg, P. M., 1992. A modified gradient method for two-dimensional problems in tomography. *Journal of Computational and Applied Mathematics*, **42**(1), 17-35. doi: doi:10.1016/0377-0427 (92)90160-Y.

Kooij, B.J. and van den Berg, P.M., 1998. Nonlinear inversion in TE scattering. *IEEE Transactions on Microwave Theory and Techniques*, **46**(11), 1704-1712.

Korpisalo A. and Heikkinen E. 2014. Radiowave imaging research (RIM) for determining the electrical conductivity of the rock in borehole section OL-KR4− OL-KR10 at Olkiluoto, Finland. *Exploration Geophysics*, **46**(2), 141-152.

Korpisalo, A.L., 2016. *Electromagnetic Geotomographic Research on Attenuating Material Using the Middle Radio Frequency Band*. PhD dissertation, University of Helsinki.

Li, Y. and Smith, R. S., 2015. Forward modeling of radio imaging (RIM) data with the Comsol RF module. *Computers & Geosciences*, **85**, 60-67. doi: 10.1016/j.cageo. 2015.08.012.

Li, Y. and Smith, R. S., 2016. A novel imaging method for cross-hole radio imaging (RIM) data: Complex permittivity inversion. *SEG Technical Program Expanded Abstracts 2016*, 2149-2153. doi: 10.1190/segam2016-13453513.1.

Li, Y. and Smith, R. S., 2017a. Modelling and straight-ray tomographic imaging studies of cross-hole radio-frequency electromagnetic data. *Geophysical Prospecting*, accepted paper.

Li, Y. and Smith, R. S., 2017b. Contrast source inversion (CSI) for cross-hole radio imaging (RIM) data - part 2: a complex synthetic example and a case study. *Journal of Applied Geophysics*, submitted paper.

Mojabi, P. and LoVetri, J., 2009. Microwave biomedical imaging using the multiplicative regularized Gauss-Newton inversion. *IEEE Transactions on Antennas and Wireless Propagation Letters*, **8**, 645-648. doi: 10.1109/LAWP.2009. 2023602.

Mojabi, P., LoVetri, J. and Shafai, L., 2011. A multiplicative regularized Gauss–Newton inversion for shape and location reconstruction. *IEEE Transactions on Antennas and Propagation*, **59**(12), 4790-4802. doi: 10.1109/TAP. 2011.2165487.

Mutton, A. J., 2000. The application of geophysics during evaluation of the Century zinc deposit. *Geophysics*, **65**(6), 1946-1960. doi: 10.1190/1.1444878.

Naprstek, T. and Smith, R. S., 2016. The effect of dielectric permittivity on the fields radiated from a radio-frequency electric dipole in a homogeneous whole space. *Geophysics*, **81**(2), K1-K8. doi: 10.1190/geo2015-0219.1

Richmond, J., 1965. Scattering by a dielectric cylinder of arbitrary cross section shape. *IEEE Transactions on Antennas and Propagation*, **13**(3), 334-341.

van den Berg P.M. and Kleinman, R.E., 1997. A contrast source inversion method. *Inverse Problems*, **13**(6), 1607-1620. doi: 10.1088/0266-5611/13/6/013.

van den Berg, P.M., Van Broekhoven, A.L. and Abubakar, A., 1999. Extended contrast source inversion. *Inverse Problems*, **15**(5), 1325 - 1344.

Ward S. H. and Hohmann G. W., 1988. Electromagnetic theory for geophysical applications. In: *Electromagnetic Methods in Applied Geophysics*, Vol. 1, (ed. M. N. Nabighian), 131-311. Society of Exploration Geophysicists. doi: 10.1190/1.9781560802631.ch4.

Chapter 5

5 Contrast source inversion (CSI) method to cross-hole radio-imaging (RIM) data - part 2: a complex synthetic example and a case study[4]

5.1 Abstract

We present two examples of using the contrast source inversion (CSI) method to invert synthetic radio-imaging (RIM) data and field data. The synthetic model has two isolated conductors (one perfect conductor and one moderate conductor) embedded in a layered background. In the inverted conductivity model, we can identify the two conductors. The shape of the perfect conductor is better resolved than the shape of the moderate conductor. The inverted conductivities of the two conductors are approximately the same, which demonstrates that the conductivity values cannot be correctly interpreted from the CSI results. The boundaries and the tilts of the upper and the lower conductive layers on the background can also be inferred from the results, but the centre parts of conductive layers in the inversion results are more conductive than the parts close to the boreholes. We used the straight-ray tomographic imaging method and the CSI method to invert the RIM field data collected using the FARA system between two boreholes near Sudbury, Canada. The RIM data include the amplitude and the phase data collected using three frequencies: 312.5 kHz, 625 kHz and 1250 kHz. The data close to the surface are contaminated by the reflected or refracted electromagnetic (EM) fields from the ground surface, which are identified and removed for all frequencies. Higher-frequency EM waves attenuate more quickly in the subsurface environment, and the locations where the measurements are dominated by noise are also removed. When the data are interpreted with the straight-ray method, the images differ substantially for different frequencies. In addition, there are some unexpected features in the images, which are difficult to interpret. Compared with the straight-ray imaging results,

[4] Original manuscript submitted to *Journal of Applied Geophysics.*

the inversion results with the CSI method are more consistent for different frequencies. On the basis of what we learned from the synthetic study, we interpret that there is one resistive layer across the middle of the borehole plane and two more conductive areas above and below this layer. Though there are some limitations in the study, such as the precise amplitudes and dipole moments being unknown, we conclude that the CSI method provides more interpretable images compared with the straight-ray method.

5.2 Introduction

The radio imaging method (RIM) is a cross-hole electromagnetic (EM) exploration method, which employs radio frequencies (typically 0.1 to 10 MHz) EM waves to delineate the electric properties on the plane defined by two boreholes. RIM is often used in mineral exploration and delineation, particularly in Sudbury, Canada (Thomson and Hinde, 1993; Stevens et al., 2000; McDowell et al., 2007). The principle of the RIM exploration is similar to the X-ray computerized tomography (CT) in medical imaging. The straight-ray imaging method has until now been the primary method for imaging RIM data, which was adopted from the CT imaging technique (Dines and Lytle, 1979; Jackson and Tweeton, 1994; Li and Smith, 2017a). The straight-ray imaging results can in some cases be helpful in interpreting the geologic structure, but in other cases can be misleading, and make interpretation even more difficult. Unfortunately, the unsuccessful cases are often not published.

Li and Smith (2015) showed that a finite-element modelling package, Comsol Multiphysics, could be used to generate reliable and valid synthetic RIM data. Li and Smith (2017a) then carried out modelling studies using the synthetic data generated with Comsol Multiphysics and found that the interaction of radio-frequency EM fields with the conductors mainly occurs as a result of induction and diffraction, and the straight-ray method cannot always provide high-quality imaging results.

In part 1 of this study (Li and Smith, 2017b), we adopted the 2D contrast source inversion (CSI) method, which was originally developed for microwave tomography in medical imaging (van den Berg and Kleinman, 1997; van den Berg et al., 1999; Abubakar et al., 2002), to work for RIM data. The effectiveness of the CSI method was assessed for RIM using synthetic data generated with Comsol Multiphysics. The studies show that the position and the rough shape of isolated conductors can be identified from the inversion results using the CSI method. The resulting images are more like the original models than those generated using the straight-ray method (Li and Smith, 2017a).

In this paper, we will present the part 2 of the study. In Section 5.3, we will present a synthetic study of a more complicated model with a perfect conductor and a moderate conductor embedded in a layered environment. This model is more representative of the complex geology seen in a mining environment, and will be helpful to interpret the inversion results of real data.

To better understand the strengths and weaknesses of the CSI algorithm and the ability of the technique to operate on noisy and incomplete field data, in Section 5.4, we will present a case study showing the application of the CSI method to real data. The data were collected near Sudbury, Canada. Working with real data requires some pre-processing steps. In Subsection 5.4.1, we will show how to identify and remove the field data contaminated by noise. Though synthetic studies show that CSI method is quite robust to noise (Li and Smith, 2017b), the synthetic models do not take into account reflected or refracted fields from the atmosphere/earth interface (Hill, 1984), and these will significantly affect the inversion results. In order to reduce the effect of this interface, we explain how we remove the affected waves for the inversion. In our companion paper, we showed how to use an equivalent 2D model to represent the 3D background model for the synthetic data. In Subsection 5.4.2, we

will show how to find the equivalent models for the observed data. In Subsection 5.4.3, we will present the inversion results for the field data obtained with the CSI method, and compare these with the straight-ray imaging results. We will show how the inversion results of the complex synthetic example in Section 5.3 can help us to interpret the inversion results for the real data.

5.3 A synthetic example with layered background

5.3.1 Model setup and background model

Table 5-1. Conductivity, wavelength and maximum element size for the sub-domains of the more complex synthetic example

Sub-domains	Conductivity (S/m)	Wavelength (m)	Maximum element size (m)
centre layer	0.0001	48.87	8
upper, lower layers	0.001	43.26	7
conductor 2	0.01	19.18	3.8
conductor 1	Infinite	Infinitesimal	8

To demonstrate that the CSI method can be used to invert the RIM data in a realistic situation, we build a model with two isolated conductors embedded in a layered background in Comsol Multiphysics. The model shown in Figure 5-1a is in a Cartesian coordinate system with the *x*-axis from left to right, *z*-axis from down to up and *y*-axis perpendicular to the page. Figure 5-1a shows the geometry of the borehole plane ($y = 0$): the background is a three-layered model; the upper layer and the lower layer have a conductivity of 0.001 S/m; the centre layer has a conductivity of 0.0001 S/m; the two conductors are embedded in the centre layer; conductor 1 is a perfect conductor; conductor 2 is a moderate conductor with a conductivity of 0.01 S/m. We use a constant relative permittivity $\varepsilon_r = 6$ and a constant relative magnetic permeability $\mu_r = 1$ for the whole model. Both conductors are rectangular

prisms with a strike length of 60 m (from y = -30 m to y = 30 m). Conductor 1 has an rectangular intersection of 80 m × 30 m with the borehole plane, which is tilted 30 degree to the upper-right from the horizontal direction; conductor 2 has an rectangular intersection of 75 m × 25 m, and is tilted 15 degree to the upper-right. These isolated conductors are repersentative of conductive nickel copper orebodies and the upper and lower layers are representative of slightly more conductive lithologies.

Two sub vertical boreholes are on either side of the borehole plane. The left borehole is from (x, z) = (-210, 100) to (-190, 440); the right borehole is from (5, 100) to (-5, 440). The domain of interest is a prism of 215 m × 340 m × 60 m, which includes the two boreholes and five sub-domains (the two conductors and the three layers). We simulate a RIM survery with receivers spaced at 5 m intervals in one borehole and transmitters every 20 m in the other hole. Data sets with the transmitter locations in both boreholes are generated. The transmitting frequency is 2.5 MHz, which is one of the operating frequencies of the FARA system (Li and Smith, 2015). The dipole moment of the source is 4000 Am. Each sub-domain has a different conductivity and wavelength, requiring that for the Comsol forward modelling, we mesh each sub-domain with different element sizes (Li and Smith, 2015), that are between 1/5 to 1/7 of the wavelength (Table 5-1). The exception is conductor 1, which is a perfect conductor and the boundary condition means that the volume inside does not have to be discretized carefully (Li and Smith, 2017a). With this meshing, the expected errors in the synthetic data are less than 5% (Li and Smith, 2015). To consider the slight dip of the boreholes, the modelled data at the receiver boreholes are projected onto the borehole axis direction and the dipole source is aligned with the direction of the transmitter borehole trajectory.

In the companion paper, we explained that the CSI method solves for the deviation from a universal background wavenumber, with more conductive anomalies resulting in weaker amplitudes (Li and Smith, 2017b). We want to make the background material the most resistive material in the borehole section and then solve for more conductive zones. To find an equivalent 2D background model, we look for the most resistive part of the borehole plane, where the EM waves have the less attenuation. Then we fit the data of a dipole source in a homogeneous model using the fields of a 2D dipole in a homogeneous whole-space model.

As the centre layer is the most resistive, we define the parameters of the centre layer to be the background model. We use a 2D model to fit the 3D data generated for a whole space by adjusting the conductivity, permittivity and the dipole moment of the 2D model (Table 5-2). The only significant adjustment requires is a smaller dipole moment for the 2D model.

Table 5-2. Equivalent 2D model to fit the 3D homogeneous whole-space model for the frequency of 2.5 MHz

	3D model	2D model
Conductivity (S/m)	0.0001	0.0001
Permittivity	6	5.7
Dipole moment (Am)	4000	40

5.3.2 Inversion results

In the inversion process, we mesh the 215 m × 340 m borehole plane with 322 cells, each of which is a rectangle of size 15.4 m × 14.8 m. The dip of the boreholes is accounted for in the inversion: the fitted data are the appropriate combination of the x- and z-directed components and the sources are the appropriate combination of x- and z-axis dipoles. Throughout the inversion, the cost function converges stably and arrives at a value of 0.0015 after 400 iterations (Li and Smith, 2017b), which indicates a good fit between the observed data and

the fitted data. No significant improvement in the results can be observed with further iterations. We show the inverted conductivity on Figure 5-1b. The central parts of the upper layer and the lower layer have the highest conductivity value in the inverted conductivity model, which is higher than the true conductivity (0.001 S/m). Even though the central parts of the upper and the lower layers are conductive and the left and the right parts of each of these layers are more resistive, we can still interpret the boundaries and the angles of the tilted interfaces from Figure 5-1b. The embedded conductor 1 is clearly shown in the inversion results in the correct position, with a roughly correct shape and tilted in the correct orientation. There is a conductive area at the centre position of conductor 2, but the right boundary of conductor 2 is poorly resolved. We infer the reason for the lower resolution of conductor 2 is that the lower conductivity causes weaker scattered fields. There are low conductivity areas between adjacent conductors, which can be used to identify the zones as separate conductors within the inverted conductivity model.

The highest inverted conductivity value of the two conductors in the centre layer is about 0.0006 S/m. This is much lower than the true values (infinite and 0.01 S/m). As noted above, the central parts of the upper layer and the lower layer have higher conductivities than the part close to the borehole, which is identified as the resistive artefacts. We infer that these artefacts are caused by the large volume of the upper and lower layers, which has highly attenuated the EM fields. A high conductivity in the central parts of these layers can account for these attenuations. From this model, we can see that, besides the conductivity, the size of a conductor also affects the inverted conductivity model.

We conclude that, the inverted conductivity model with the CSI method provides information that is helpful in identify isolated conductive zones in resistive environment, as well as the

interfaces and orientations of the conductive layers. The results of this synthetic study are helpful to interpret the inversion sections delivered from real data.

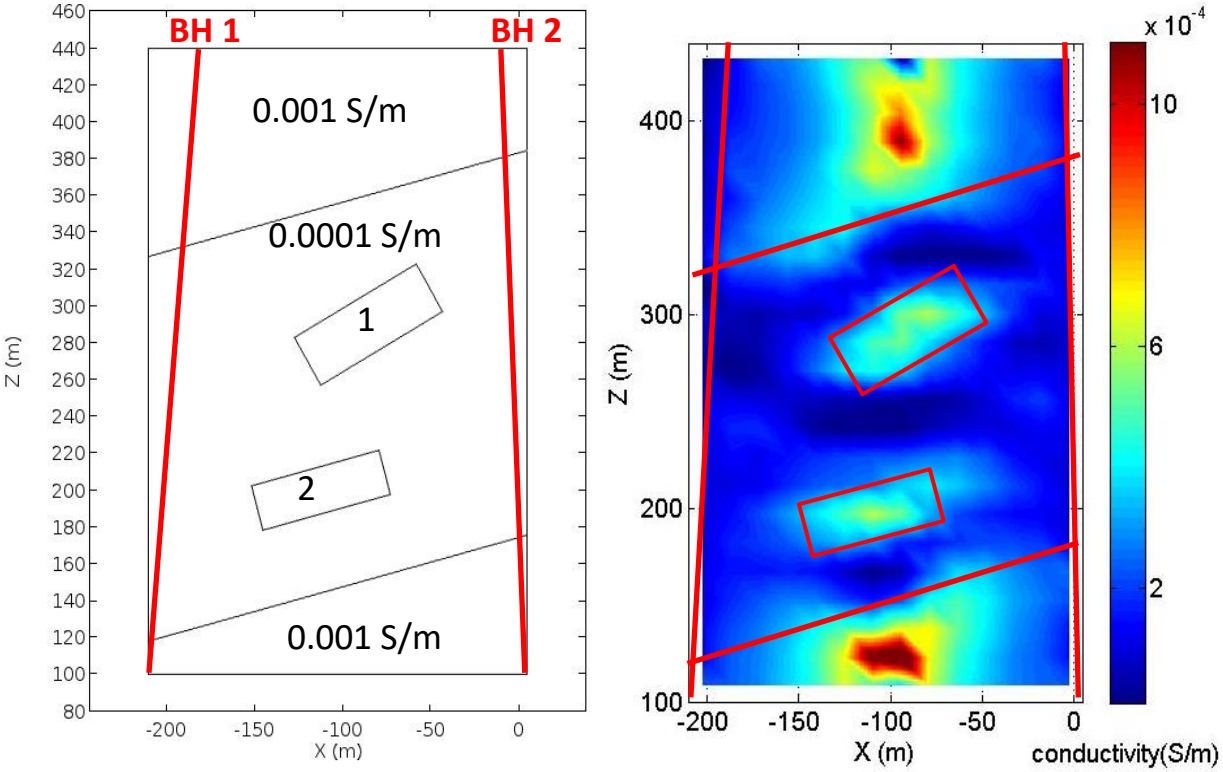

Figure 5-1. Synthetic example with layered background and two conductors. (a) Conductivity of upper layer and lower layer is 0.001 S/m; centre layer is 0.0001 S/m. A perfect conductor (conductor 1) and a moderate conductor (conductor 2) with conductivity of 0.01 S/m are embedded in the centre layer. (b) Inverted conductivity after 400 iterations.

The inversion time is 6.5 minutes for 400 iterations in a dual-core computer with a clock speed of 2.6 GHz. It takes around 90 minutes to compute the synthetic data for one transmitter location only. There are 36 transmitter locations in total. Compared with the Comsol modelling, the computation time for the CSI method is quite reasonable and will make it practical to use.

One question on the inversion process is whether the cell size has an effect the inversion results. We carried out experiences to invert synthetic data using cell sizes of side lengths from 10 m to 30 m. We found that when using the cell sizes with side length less than 15 m,

the inversion process is unstable and cost function did not converge. When using the cell size with side length between 15 m to 30 m, the cost function converge stably and the inversion results are quite consistent. Theoretically, smaller features could be imaged with smaller cell sizes, and longer computational time is required. However, the number of cells determines the degree of freedom in the model, so we need to select a cell size according to the number of data to avoid an underdetermine problem. To select a reasonable cell size, the resolution of the EM waves, which is determined by the wavelength, should be considered as well. From the experiment results, we empirically recommend the cell size with side length longer than 75% of the transmitter spacing.

5.4 Field study

The RIM data are collected between two boreholes using the FARA system (Li and Smith, 2015). The top of the two boreholes is about 570 m apart. The boreholes are sub vertical as shown on the left and the right side of Figure 5-6a.

The FARA system transmits current at multiple discrete frequencies (312.5 kHz, 625 kHz and 1250 kHz) at the same time, and measures the signal in another borehole. By processing the signals, the amplitude and the phase data of each of three frequencies are extracted as the measurements. So, for each transmitter-receiver pair, there are six measurements. The units of the amplitude data are not calibrated (in this paper, the unit of the amplitude data is given arbitrary or unknown units). The current generating the EM field at each frequency is not provided by the FARA system, so the dipole moment of the source is also unknown.

The data set for each frequency has 48 transmitter locations. In the left borehole, the transmitter location starts at a depth of 370 m, and ends at 1210 m. In the right borehole, the transmitter location starts at 360 m and ends at 1360 m. The transmitter spacing is 40 m for both boreholes. The receiver spacing is 1.5 m.

5.4.1 Data pre-processing

The data measured in the right borehole with the transmitter at a depth of 370 m in the left borehole are shown on Figure 5-2. Figure 5-2a and b shows the amplitude and the phase respectively measured at 312.5 kHz; Figure 5-2c and d show the same for 625 kHz; while Figure 5-2e and f show 1250 kHz. We identify the data highlighted in dashed boxes as the data affected by noise. These noisy data show rapid fluctuations in the phase data and low values of the amplitude data. Here, we attribute the 'noise' to be the combined effects of environmental noise, instrument noise and low sensitivity of the antennae. From Figure 5-2, it can be observed that the amplitude data lower than 300 - 1000 units appear to be contaminated by noise. We infer that the noise level of this survey is around 300 - 1000 units. Higher-frequency EM waves attenuate more quickly, and thus these data tend to be more affected by the noise.

It can also be observed that the phase data above 300 m (highlighted in dotted boxes) also show rapid fluctuation, but the value of the corresponding amplitude data are not always below the noise level. These effects appear for all the frequencies. We speculate that these data are affected by surface effects, which are caused by the reflection or refraction of the EM fields on the ground surface (Hill, 1984).

From the definition of the cost function in the CSI method, the data with higher amplitude values have higher weights than the low amplitude data in the inversion process (Li and Smith, 2017b). So, the noisy data with low amplitude values (< 1000 units) do not significantly affect the inversion results. But the data affected by surface effects, which have relative high amplitude values, will certainly deteriorate the inversion results. So, these data should be removed.

Although the noisy data do not significantly affect the inversion results, they do affect the inversion process. Greater amounts of data results in a larger matrix to build and a longer computation time. In this study, we removed the noisy data highlighted in dashed boxes to speed up the computation.

Figure 5-2e and f show that the 1250 kHz data are of low quality when the source is at 370 m depth. If we remove the highlighted data, it seems there are not much 1250 kHz data left. In Figure 5-3, we plot the 1250 kHz data with the source at a depth of 810 m in the left borehole. The data show only a little bit of noise around the top and bottom of the borehole. These data are of much higher quality, implying less attenuation of the signal between the boreholes, so there might be less conductive material proximal to the borehole at a depth of 810 m; conversely we might expect more conductive material at a depth of 370 m, resulting in greater attenuation.

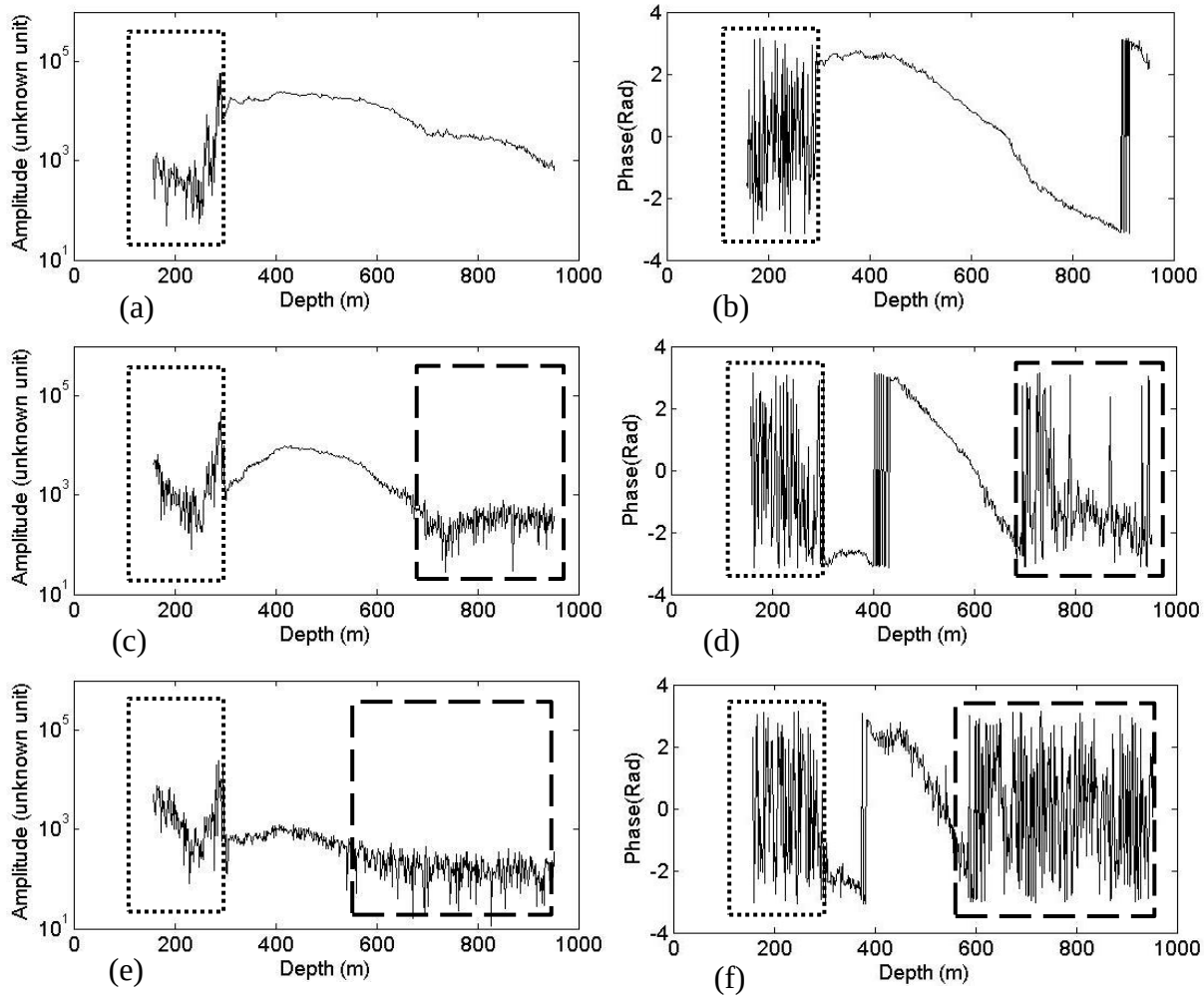

Figure 5-2. Surface effects (in dotted boxes) and noise (in dashed boxes) in the data measured in the right hole with the source at depth of 370 m in the left borehole for 312.5 kHz (a and b), 625 kHz (c and d) and 1250 kHz (e and f). The unit of the amplitude data is unknown.

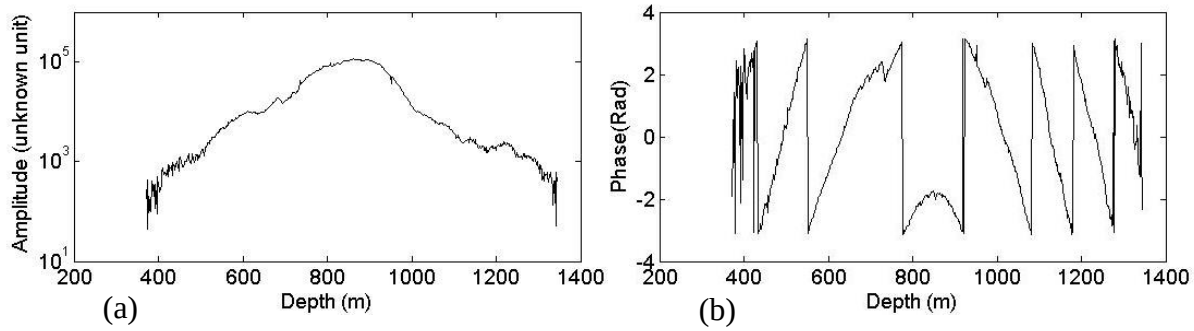

Figure 5-3. The amplitude (a) and phase data (b) measured in the right borehole with the source at the depth of 810 m in the left borehole for 1250 kHz. The amplitudes are not as attenuated, so the material proximal to 810 m is inferred to be more resistive.

5.4.2 Background model

In the synthetic model in Section 5.3, we use the physical properties of the most resistive layer to represent the background model. However, for the field data, the physical properties of the most resistive part are unknown and need to be estimated. To find the 2D background model, we look for the largest amplitudes, which represent where the data shows the least attenuation. A similar procedure is described by Naprstek and Smith (2016).

Because the transmitted dipole moment is unknown, we rely on the conductivity values to estimate the dipole moment. Conductivity measurement of the drill cores in this area shows that the conductivity values of the most resistive host rocks are on the order of 10^{-6} to 10^{-4} S/m. The permittivity values of the drill cores are usually not measured. Since, the permittivity value does not significantly affect the amplitude and we are more interested on the conductivity contrast, we will adjust the permittivity value to fit the gradient of the phase data.

Figure 5-4 shows the data at 1250 kHz measured in the left borehole with the source at a depth of 920 m in the right borehole. The amplitude values at depths close to 900 m are the largest (least attenuated) values in the data set. We fit the highest amplitude value and the gradient of the phase data using a 3D point source with a dipole moment of 2×10^5 Am, a conductivity of 1×10^{-5} S/m and a relative permittivity of 15.4. When we used a 2D source, the best fit is with a dipole moment of 1×10^3 Am, a conductivity of 1×10^{-5} S/m and a relative permittivity of 15 (Table 5-3). For the 2D and 3D models, the dipole moments are quite different, but the conductivities and relative permittivities are similar, which is similar to our observation for the synthetic example. We can see from Figure 5-4 that the 2D data and the 3D data roughly fit the highest amplitude data, and the gradients of the modelled

phase data and the observed phase data are quite consistent. Following the same procedure, we found the background models for 312.5 kHz and 625 kHz (Table 5-3).

Without knowledge of the transmitting current and the accurate conductivity of the environment, we can fit the data with many background models with conductivities from 10^{-6} to 10^{-4} S/m. We tested the inversion with some other background models (not shown in this paper). In the experiment, the inversion results are not significantly affected by using different background models. But this experiment is not a thorough study, and for each set of field data, further experiments should be carried out to demonstrate the effects of different background parameters. If the transmitting current for each frequency was fixed or measured, then a lot of this ambiguity would be removed.

When determining the background model, the fitting of the phase data are done visually and manually, so the fitting result is somewhat subjective. Moreover, the gradient of the phase data can be fit very well for some transmitter locations, but not well for some locations. We experimented with the inversion using permittivities in the range from 6 to 18. The overall inversion results are consistent in this range. Again, this conclusion only applies to this data set and further experimentation is required for other data, or further research is required to define a robust procedure to select a background model.

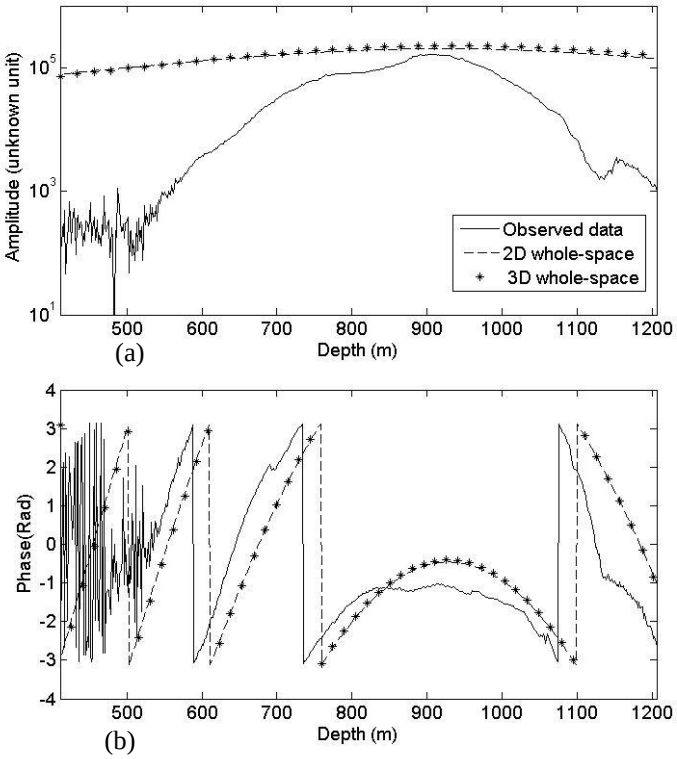

Figure 5-4. Background model fitting using a 2D model (dashed lines) and a 3D model (marked only with '+' symbols) for the 1250kHz data using the model parameters shown in Table 5-3. The data shown are the amplitude (a) and phase data (b) measured in the left borehole with the source at a depth of 920 m in the right borehole.

Table 5-3. 3D and equivalent 2D background model parameters for the real data.

	312.5 kHz		625 kHz		1250 kHz	
	3D model	2D model	3D model	2D model	3D model	2D model
Conductivity (S/m)	1×10^{-5}	1×10^{-5}	1×10^{-5}	1×10^{-5}	1×10^{-5}	1×10^{-5}
Relative permittivity	12	10.7	12.5	11.8	15.4	15
Dipole moment (Am)	10^{6}	2.5×10^{3}	3×10^{5}	9×10^{2}	2×10^{5}	1×10^{3}

5.4.3 Inversion

We use the 2D background parameters listed in Table 5-3 as input models to invert the data.

In the inversion process, the borehole planes are meshed with 665 grid cells, each of which is

about 30 m × 30 m. The borehole plane for 312.5 kHz (Figure 5-5a) extends to shallower depths because the data quality at this lower frequency is better and less data were removed close to the surface. Figure 5-5 shows the inversion results obtained with the CSI method after 200 iterations. The cost function converges stably throughout the inversion process and arrives at 0.0014, which indicates a good fit between the observed data and the fitting data. No significant changes on the inversion results can be observed with extra iterations.

We show the straight-ray imaging results in Figure 5-6. The images are provided by the contractor as final products. The quantity imaged is the resistivity (in Ωm), which is the inverse of the conductivity. Hence, for comparison purposes, we have imaged the inversion results from the CSI method (Figure 5-5) in the same units.

It can be observed from Figure 5-6 that the straight-ray imaging results for different frequencies are not consistent. There are some unexpected features at the centre of the images associated with the lower frequencies: two diagonal high resistivity (blue) zones that intersect in the centre of Figure 5-6a and b. Figure 5-6c is better, but we can still see a subtle resistive zone from upper left to lower right, which cuts through a more conductive (red) area as a green zone at a depth of the about 1050 m. These features do not look like geological structures, and are difficult to interpret.

We can see more geologically reasonable inversion results for different frequencies with the contrast source inversion method in Figure 5-5. Figure 5-5a and b (the lower frequencies) are quite similar to each other. Both show a resistive layer between the two boreholes at a depth of about 900 m (between two purple lines). There is a more conductive area at the center of this resistive layer in Figure 5-5c. We infer that, there may be some moderately conductive materials (slightly more conductive than the background) in this location, which is less sensitive to lower frequencies.

Above and below this resistive layer, more conductive areas have been identified. These conductive zones tend to be more conductive at the centre and closer to the background resistivity near the edges of the borehole plane. This is an artefact similar to what we have observed in the synthetic example in Figure 5-1, where the conductive layer actually extends all the way to the edge of the borehole plane. So, we infer the conductive zones identified at the top and the bottom of the resistive zone extend all the way to the edge of the borehole plane and the purple lines indicate a major change in the rock type.

The conductive area at the base of the plane (below the lower purple line) shows as a thin layer in Figure 5-5a and b, while it shows as a conductive area extending to the bottom of the plane in Figure 5-5c. But the transmitter locations in the left borehole stop at a depth of 1210 m. So the area close to the bottom of the plane does not have much data coverage and would be better displayed as white. We will interpret that there is a conductive layer right below the lower purple line, but the vertical extent of this layer cannot be interpreted with confidence.

The features within the upper conductive area (above the upper purple line) are quite different for different frequencies. There are horizontal slightly more resistive features in the center parts of the conductive layers, which may be caused by minor changes in the rock type. More horizontal features are found in the frequencies of 1250 kHz (Figure 5-5c), but these are comparable to the cell size and might be a consequence of the discretization, not the geology. Comparing Figure 5-5 and Figure 5-6, we found the inversion results with the CSI method are more consistent for different frequencies and easier to interpret compared with the straight-ray imaging results.

For the data of 625 kHz and 1250 kHz, it takes 26.5 minutes to invert the data at each frequency using the CSI method in the same computer as mentioned in Section 5.3. For the data of 312.5 kHz, it takes 28.5 minutes. Using the straight-ray method, the computation time

is less than 10 seconds for the data of one frequency. Though the computation times for the CSI method are much larger than those of the straight-ray method, considering the volume of the data, and the interpretability of the results, we argue that the computation time are acceptable.

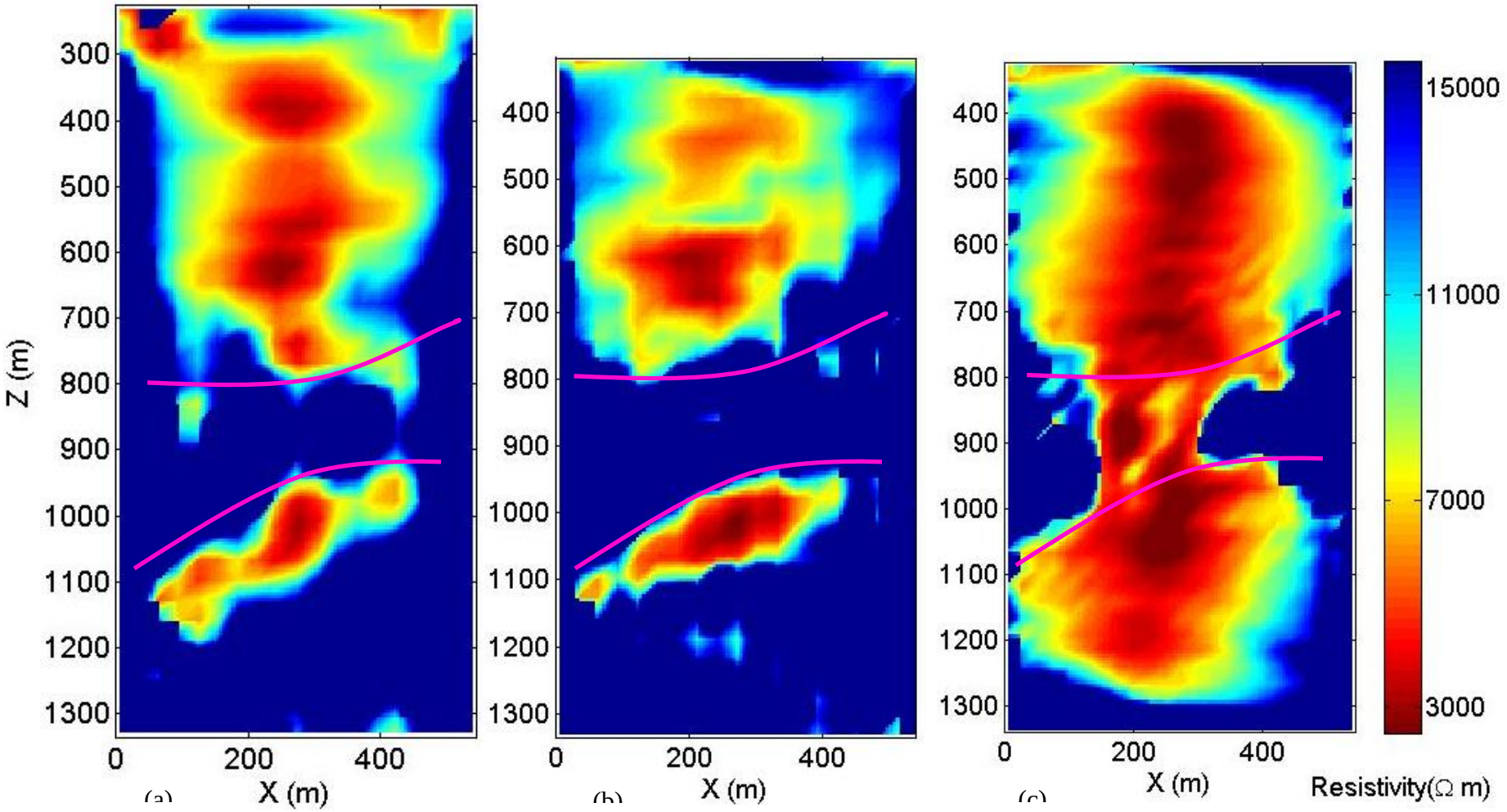

Figure 5-5. Inverted resistivity models with the contrast source inversion method for the data of 312.5 kHz (a), 625 kHz (b), and 1250 kHz (c). Interfaces between major rock units are interpreted from the images and shown as purple lines. Data courtesy of Vale.

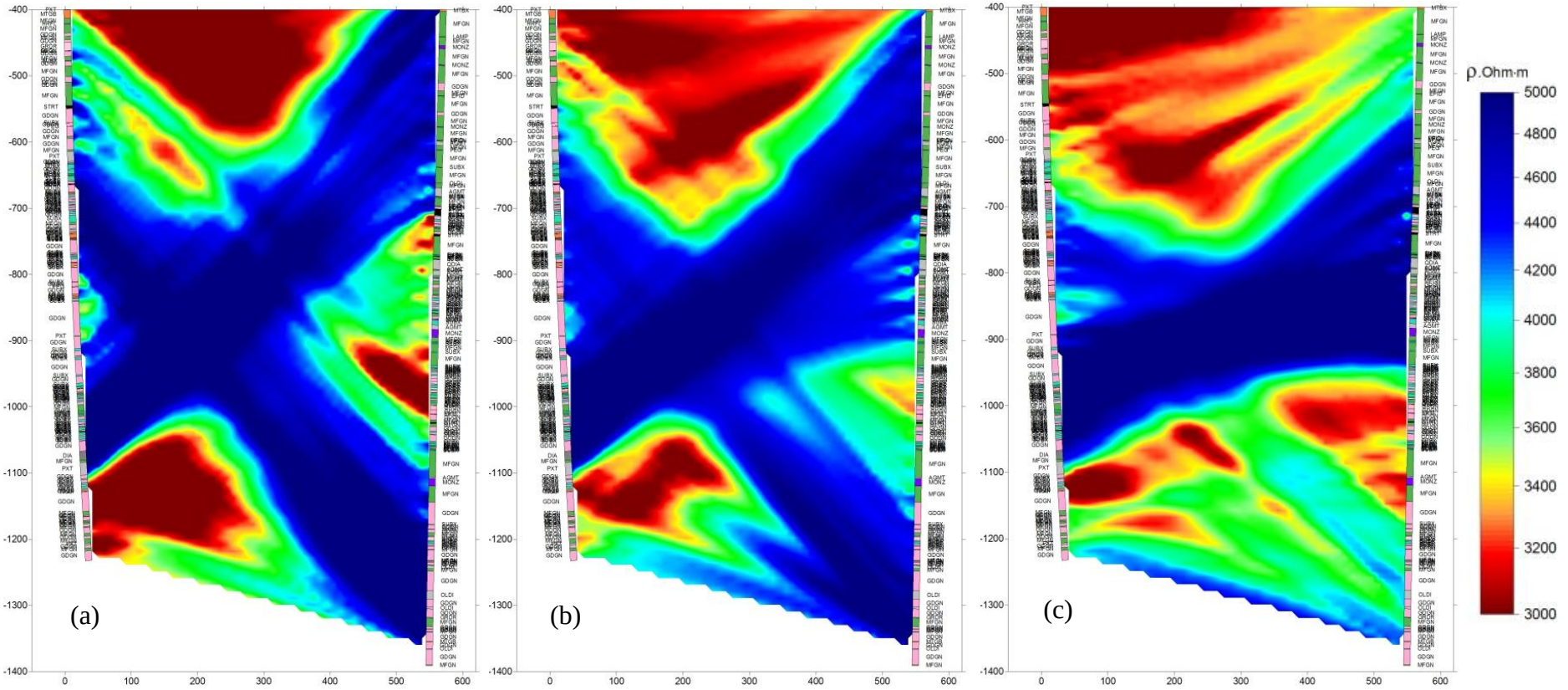

Figure 5-6. Resistivity images reconstructed with the straight-ray method for the data of 312.5 kHz (a), 625 kHz (b) and 1250 kHz (c) on a borehole section near Sudbury, Canada. The quantity on the image is resistivity (Ωm). Images courtesy of Vale.

5.5 Conclusions

We calculated synthetic RIM data using Comsol Multiphysics for a model with a perfect conductor and a moderate conductor with a conductivity of 0.01 S/m, both of which were embedded in a layered background, and used the contrast source inversion method to invert the synthetic data. The synthetic study showed that we can interpret the locations of the two isolated conductors from the inverted conductivity model. The shape of the perfect conductor is better resolved than the shape of the moderate conductor. The inverted conductivities of the two conductors are approximately the same, which reinforce the argument in our companion paper that, the conductivity values are not well resolved with the CSI method. The boundaries and the tilts of the upper and the lower conductive layers in the layered background can also be inferred from the results. At the edges of the zone of interest, near the boreholes, resistive artefacts were identified, which showed that the centre parts of conductive layers extending between the boreholes appear on sections as more conductive than the parts close the boreholes.

We applied the contrast source inversion method for RIM field data collected between two boreholes near Sudbury, Canada. The data close to the ground surface of all frequencies are contaminated by a surface effect. The higher frequency data tend to be more affected by noise. We removed the corrupted and noisy data prior to the inversion. The background model was obtained by fitting the largest amplitude part of the response and the phase slope in a resistive (low attenuation/high amplitude) area. Because the amplitude and dipole moments of the transmitter are unknown and the background models are chosen visually and manually, there is some uncertainty in the estimated values.

We inverted the data with the CSI method, and compared the results with the straight-ray imaging results. The straight-ray imaging results are not consistent for different frequencies, and show some unexplained features which are difficult to interpret. The inversion results with the CSI method are more consistent for different frequencies and easier to interpret. From the inversion results, we interpreted two major rock changes at depths of 800 and 1000 m. There is a resistive layer between the two boreholes at a depth of about 900 m. The conductive layers (above and below the resistive layer) show the center part more conductive than the areas toward the boreholes, which were resistive artefacts and interpreted to be conductive zones that extend across the borehole plane by the synthetic example. There is some hint of an embedded conductor between the upper and lower layers, but only on the highest frequency (1250 kHz). There is no such hint on any of the straight-ray sections.

For the synthetic model, it takes 6.5 minutes to invert the data. For the real data, it takes less than 30 minutes for one frequency. We argue that the computation times are acceptable given the interpretability of the results.

The methodology for estimating the background model could be improved if the amplitude were measured in calibrated units and the dipole moment of the transmitter could be measured or fixed. The inversion process could be improved by using an automatic method to select a background model. The effect of varying background parameters could also be investigated more thoroughly. Even so, from the results in this paper, we conclude that the CSI method provides imaging results that are more consistent for different frequency and easier to draw a geological interpretation compared with the straight-ray method.

5.6 Acknowledgements

The authors express acknowledgments to the Natural Sciences and Engineering Research Council of Canada (NSERC), Vale, KGHM International, Sudbury Integrated Nickel

Operations -- A Glencore Company, Wallbridge Mining and the Centre for Excellence in Mining Innovation for funding this research. We also thank Vale for providing the RIM data and the straight-ray reconstructed images.

5.7 References

Abubakar, A., van den Berg, P.M. and Mallorqui, J.J., 2002. Imaging of biomedical data using a multiplicative regularized contrast source inversion method. *IEEE Transactions on Microwave Theory and Techniques*, **50**(7), 1761-1771. doi: 10.1109/TMTT.2002.800427.

Dines, K.A., Lytle, R.J., 1979. Computerized geophysical tomography. *Proceedings of the IEEE,* **67**(7), 1065-1073. doi:10.1109/PROC.1979.11390.

Hill, D., 1984. Radio propagation in a coal seam and the inverse problem. *Journal of Research of the National Bureau of Standards*, **89**(5), 385-394. doi: 10.6028/jres.089.022.

Jackson, M.J., Tweeton, D.R., 1994. *MIGRATOM—Geophysical tomography using wavefront migration and fuzzy constraints*. Report of Investigations RI9497, Department of Interior, US Bureau of Mines, Minneapolis, MN, USA, 41 pp.

Li, Y. and Smith, R. S., 2015. Forward modeling of radio imaging (RIM) data with the Comsol RF module. *Computers & Geosciences*, **85**, 60-67. doi: 10.1016/j.cageo. 2015.08.012.

Li, Y. and Smith, R. S., 2017a. Modelling and straight-ray tomographic imaging studies of cross-hole radio-frequency electromagnetic data. *Geophysical Prospecting*, accepted paper.

Li, Y. and Smith, R. S., 2017b. Contrast source inversion (CSI) method for cross-hole radio imaging (RIM) data – part 1: theory and synthetic studies. *Journal of Applied Geophysics*, submitted paper.

McDowell G. M., Stewart R. and Monteiro R. N. 2007. In-mine Exploration and Delineation Using an Integrated Approach. *Proceedings of Exploration,* **07**, 571-589.

Naprstek, T. and Smith, R. S., 2016. The effect of dielectric permittivity on the fields radiated from a radio-frequency electric dipole in a homogeneous whole space. *Geophysics*, **81**(2), K1-K8. doi: 10.1190/geo2015-0219.1.

Stevens K., Watts A. and Redko G. 2000. In-mine applications of the radio-wave method in the Sudbury igneous complex. *In 2000 SEG Annual Meeting. Expanded Abstracts*, 1130-1133. doi: 10.1190/1.1815587.

Thomson, S., Hinde, S., 1993. Bringing geophysics into the mine: radio attenuation imaging and mine geology. *Exploration Geophysics,* **24**(3-4), 805-810. doi: 10.1071/EG993805.

van den Berg P.M. and Kleinman, R.E., 1997. A contrast source inversion method, *Inverse Problems*, **13**(6), 1607-1620. doi: 10.1088/0266-5611.

van den Berg, P.M., Van Broekhoven, A.L. and Abubakar, A., 1999. Extended contrast source inversion, *Inverse Problems*, **15**(5), 1325-1344. doi: 10.1088/0266-5611.

Chapter 6

6 Conclusions

6.1 Summary of research findings

6.1.1 Forward modelling

In Chapter 2, I introduced the finite element (FEM) modelling tool, Comsol Multiphysics, to model radio-imaging (RIM) data and compared the Comsol modeling results (with 6 types of element sizes at 4 frequencies) with the analytical solution for the homogeneous whole space. I found that the synthetic data generated with 5 elements per wavelength have modeling errors less than 5%; 7 to 8 elements per wavelength yield errors of approximately 1%; and 10 elements per wavelength give errors less than 1%. The comparison studies for anomalous models show that the Comsol modeling results are consistent with the analytical solutions and the solutions of other numerical modeling methods. Further, the guidelines for element sizes derived from homogeneous whole space models can be applied to inhomogeneous models with satisfactory results.

I used a modeling example with two moderately conductive bodies between boreholes to illustrate the capability of the Comsol package. A receiver profile and a relative variation map were used to visualize the data and to study the physical phenomena of radio-frequency electromagnetic (EM) waves. The study shows that, with the transmitting frequency 2.5 MHz and the EM wavelength around 47 m, the attenuation inside the two conductive bodies is apparent in the relative variation map and a radio shadow behind the conductors is observed; however, this shadow is not as sharp as the ray theory would predict. Reflections are also apparent between the source and the conductive bodies. With the simultaneous iterative reconstructive technique (SIRT) algorithm (one of the straight-ray imaging algorithms), the approximate location and the shape of the conductive anomalies can be reconstructed

somewhat successfully. The imaging results have some problems such as low resolution, incorrect conductivity estimation, and some artefacts. The Comsol package is a useful FEM modeling tool for modelling RIM data, and will be used to undertake further studies to understand the EM phenomena in this thesis.

6.1.2 Modelling and straight-ray imaging studies

In Chapter 3, I carried out modelling and imaging studies with the straight-ray method. From the studies at the transition between the diffusive regime and the propagation regime, I conclude that the behaviour and characteristics of radio-frequency EM fields depend mainly on the wavelengths and the geometry of the borehole configuration. When a perfect conductor is less than one wavelength from the source, induction has a major influence on the character of the data. In this situation, straight-ray phase tomography cannot recover the location of the conductor; but amplitude tomography can recover the location of the objects with simple geometries. When a conductor is more than two wavelengths away from the source, wave propagation effects play a major role on the data. In this situation, phase tomography works quite well if the absolute phase data can be recovered successfully; however, amplitude tomography generates low-quality images with a conductive zone surrounding a more resistive zone at the centre of the conductor; I believe this is due to the diffraction phenomenon.

The far-field approximation is applicable more than about two wavelengths away from the source in the polar angle ranges between about -50 and +50 degrees. In this situation, the diffraction of EM waves around highly conductive objects causes retardation of the phase data, which is similar to the phase shift propagating inside moderate conductors, which explains why an anomaly in the phase data can be observed and phase tomograms provide reasonable images. For these highly conductive objects, the interactions of the radiation

waves with the conductors mainly causes attenuation inside the conductors, and reflection and diffraction outside the conductors, which results in amplitude tomography providing low-quality images. Although for conductors having simple geometries, amplitude tomography can recover the location, and phase tomography can reconstruct the location and the approximate shape, the value of the reconstructed conductivities are just a few times higher than the background conductivity, which is much lower than the conductivities of most ore zones. Practitioners should be aware that the precise conductivity value cannot be recovered from the straight-ray tomograms.

From the imaging studies with reciprocal data generated for the L-shaped model, I found that, for noise-free data, the imaging results with the original data, the reciprocal data and the combined data set are similar; and the reciprocal data do not significantly improve the image quality. However, for noisy phase data, imaging with the combined data set can reduce the impact of noise and improve the quality of the images somewhat, compared to those images generated with only one data set. This suggests that it is beneficial to collect the reciprocal data if straight-ray imaging is to be undertaken on the data.

From the amplitude tomographic studies of the conductive models with different lateral extents, I found that for my example, the extents of the conductive zones with conductivity of 1 S/m cannot be imaged accurately. The imaging results for models with conductive zones of different lengths and using two different frequencies are similar, because the electric field attenuations at the receivers inside the conductor are so strong that their impact on the imaging was overwhelming. Practitioners should be aware that if a conductive zone is intersected by one hole, it is difficult to determine how far that conductive zone extends towards the other hole using straight-ray tomography.

Although imaging studies showed that I can recover the location and rough shape of conductors with phase tomography, the phase data are not always able to be unwrapped successfully. For example, I did not show the phase tomograms in the imaging studies for conductors of different lateral extent (section 3.4.4), because highly conductive material near the boreholes result in noisy data at the receivers, and thus the absolute phase data cannot be recovered. This is a limitation of phase tomography in many circumstances.

As different-wavelength EM fields have different characteristics and the wavelength varies over a large range, it is necessary to investigate the wavelengths of the EM fields before carrying out a RIM survey. The wavelength depends on both frequency and electric properties (conductivity and relative permittivity) of the environment and I recommend that study of the local electric properties should be carried out.

From the experimental results in this paper, I conclude that the straight-ray attenuation model is not appropriate for describing the EM field distribution over the whole radio-frequency range. Even so, I acknowledge that the positions of conductor can be recovered for some conductor with simple geometries, which explains the good results of some case studies (Thomson and Hinde 1993; Stevens *et al*. 2000). Hence, the straight-ray method can be used in these specific circumstances as a preliminary imaging method because of its fast processing time (the computation time for each experiment in Chapter 3 is less than 10 seconds on a dual-core laptop with the clock speed 2.6 GHz).

To better interpret RIM data, inversion algorithms based on the full EM solution would be a more generally applicable method, and development efforts in this direction were subsequently undertaken as part of the work program for this thesis. If there is a limitation on the computation time and an approximation of the EM field has to be used, methods that are most appropriate are those that account for induction effects (e.g. Yu and Edwards 1997,

MacLennan *et al*. 2013) to image the near-field data (less than one wavelength; lower frequencies). For far-field data (more than two wavelengths away; high frequencies), I suggest using wave-based tomographic methods (e. g. Joachimowicz *et al.* 1991, Abubakar *et al*. 2002).

6.1.3 Contrast source inversion

In Chapter 4, I introduced the 2D contrast source inversion (CSI) method for the cross-hole RIM data. The CSI method is based on forward modelling the EM fields with the moment method, which makes use of the solutions of the Helmholtz equation in a homogeneous environment. Thus, the CSI method accounts for EM wave phenomena. The 2D CSI method applied for RIM data requires some preliminary fitting to determine the conductivity, permittivity and the dipole moment of an effective 2D source that can explain the 3D data.

An experiment with a prismatic perfect conductor using a transmitting frequency of 3 MHz shows that the inversion converges and I can successfully interpret the location and the shape of a highly conductive object from the inverted conductivity. I studied the same model for a transmitting frequency of 1 MHz and found that the resolution of the object in the image depends on the ratio of the size of the conductor to the wavelength. An object with its size larger than half of the wavelength can be imaged successfully using the CSI method; while an object smaller than half of the wavelength can also be identified, but the shape cannot be interpreted with confidence. We found in Chapter 3 that the EM interactions with the conductors are mainly shown as diffraction at 3 MHz, and induction at 1 MHz. The experiments of the same models using CSI method indicate that the CSI method works better for the cases when the EM waves phenomena occurs.

Experiments that added 10 % noise to the above datasets show that the presence of noise does not significantly affect the inversion results, so the CSI method is very robust to the presence

of noise. An inversion using a single borehole data set was significantly worse than an inversion that also included a reciprocal data set. Hence, if the CSI method is to be used to image RIM data, reciprocal data are definitely recommended.

A data set generated with an L-shaped perfect conductor at transmitting frequencies of both 1 MHz and 3 MHz showed that in the 3 MHz case the rough boundaries of three edges of the conductor can be identified, but it is hard to interpret the exact shape of the smaller features. For the 1 MHz data, the edges of the conductor are more diffuse, but an overall orientation (from bottom right to top left) can be identified.

In the synthetic studies, I used a perfect conductor to represent highly conductive anomalies with conductivity higher than 1 S/m. However, the inverted conductivity values are only a few times higher than the background. The inverted conductivity values are higher with higher-frequency data. I infer that it is difficult to interpret the correct conductivity values from the inversion results. The run times for the experiments using the CSI method are 17 to 18 minutes and will mean that the CSI method will be practical for RIM data inversion.

There are limitations on the 2D CSI method. The 2D assumption means that there is a preliminary step to estimate the parameters of the 2D model that can simulate the 3D data of the background model. This means that a background model must be selected. If the incorrect background is selected, then the results may be different. The 2D assumption can be invalid in reality, such as the presence of an asymmetric model (asymmetric across the borehole plane). Of course, more appropriate models are 2.5D models (2D model and 3D source) and 3D models. The 2.5D model was not implemented in this thesis as it would be 1) more complex to code and 2) take longer to run.

Even so, the modelling studies in Chapter 4 are very encouraging. The features that can be identified using transmitters and receivers on either side of the zone of interest are much

more detailed than that are normally seen when the transmitters and the receivers are on the surface. The CSI method can be extended to 3D using different Green's functions (Joachimowicz et al., 1991; Abubakar, et al., 2002). However, 3D inversion was not implemented for this thesis as it requires information from more than two boreholes. To my knowledge, the instruments available to the mining industry only have one transmitter and one receiver in two boreholes. More versatile instruments with multiple receivers, which can be used to receive signals in multiple boreholes, are required and I encourage the development of such tools.

Advantages of the proposed 2D CSI method as applied to RIM data are its easy implementation, and fast solution, which makes it practical for fast interpretation. Even for the 3D inversion, this method could be used to build a starting model.

6.1.4 Case studies

In Chapter 5, I calculated synthetic RIM data using Comsol Multiphysics for a model with a perfect conductor and a moderate conductor with a conductivity of 0.01 S/m, both of which were embedded in a layered background, and used the contrast source inversion method to invert the synthetic data. The synthetic study showed that I can interpret the locations of the two isolated conductors from the inverted conductivity model. The shape of the perfect conductor is better resolved than the shape of the moderate conductor. The inverted conductivities of the two conductors are approximately the same, which verified the argument in Chapter 4 that, the conductivity values are not well resolved with the CSI method. The boundaries and the tilts of the upper and the lower conductive layers in the layered background can also be inferred from the results. At the edges of the zone of interest, near the boreholes, resistive artefacts were identified, which showed that the centre parts of

conductive layers extending between the boreholes appear on sections as more conductive than the parts close the boreholes.

I applied the contrast source inversion method for RIM field data collected between two boreholes near Sudbury, Canada. The data close to the ground surface of all frequencies are contaminated by a surface effect. The higher frequency data tend to be more affected by noise. I removed the corrupted and noisy data prior to the inversion. The background model was obtained by fitting the largest amplitude part of the response and the phase slope in a resistive (low attenuation/high amplitude) area. Because the amplitude and dipole moments of the transmitter are unknown and the background models are chosen visually and manually, there is some uncertainty in the estimated values.

I inverted the data with the CSI method, and compared the results with the straight-ray imaging results. The straight-ray imaging results are not consistent for different frequencies, and show some unexplained features which are difficult to interpret. The inversion results with the CSI method are more consistent for different frequencies and easier to interpret. From the inversion results, I interpreted two major rock changes at depths of 800 and 1000 m. There is a resistive layer between the two boreholes at a depth of about 900 m. The conductive layers (above and below the resistive layer) show the centre part more conductive than the areas toward the boreholes, which were resistive artefacts and interpreted to be conductive zones that extend across the borehole plane by the synthetic example. There is some hint of an embedded conductor between the upper and lower layers, but only on the highest frequency (1250 kHz). There is no such hint on any of the straight-ray sections.

For the synthetic model, it takes 6.5 minutes to invert the data. For the real data, it takes less than 30 minutes for one frequency. I argue that the computation times are acceptable given the interpretability of the results.

The methodology for estimating the background model could be improved if the amplitude were measured in calibrated units and the dipole moment of the transmitter could be measured or fixed. The inversion process could be improved by using an automatic method to select a background model. The effect of varying background parameters could also be investigated more thoroughly. Even so, from the results in Chapter 5, I conclude that the CSI method provides imaging results that are more consistent for different frequencies and easier to interpret geologically compared with the straight-ray method.

6.2 Suggestions for future studies

In this thesis, I only presented one case study for the CSI method. More case studies should be carried out to prove the effectiveness and to explore the strengths and weaknesses of the method.

The presented CSI method is based on a 2D source and model, with an assumption that I can use an equivalent 2D model to represent the 3D EM fields. The consequence of this assumption is that a uniform background wavenumber is used for the whole model when calculating the Green's function, which I believe results in the resistive artefacts on the edges of the conductive layers (Section 5.3.2). To improve the inversion result, it is worthwhile investigating inversion algorithms that use the Green's functions for stratified media (Chew, 1995; Michalski and Mosig, 1997), particularly if electric properties of the subsurface imply a layered structure.

The CSI method presented in this thesis treats the RIM data of a single frequency at a time. To generate an inversion result that can be interpreted with more confidence, I suggest trying to generate a single model that is consistent with the data collected at multiple frequencies (e.g. Bloemenkamp et al., 2001).

The 2D assumption of the CSI method is a limitation. More detailed model studies are required to determine if any artefacts are caused by this assumption.

To improve the inversion, I suggest developing inversion methods based on a 2.5D model (2D model and 3D source), similar to those implemented for low frequency electromagnetic data (Abubakar et al., 2008).

In fact, the contrast source method can be extended to 3D using the 3D dyadic Green's function. Pioneering works on 3D back scattering inversion can be found at Joachimowicz et al. (1991) and Abubakar et al. (2002).

However, 3D exploration requires information from more than two boreholes. To my knowledge, the cross-hole EM instruments available to the mining industry only have one transmitter and one receiver (Li and Smith, 2015; Korpisalo, 2016). I encourage the development of a more versatile instrument with one transmitter in one borehole and multiple receivers (Figure 6-1), which can be used to receive signals in multiple boreholes at the same time.

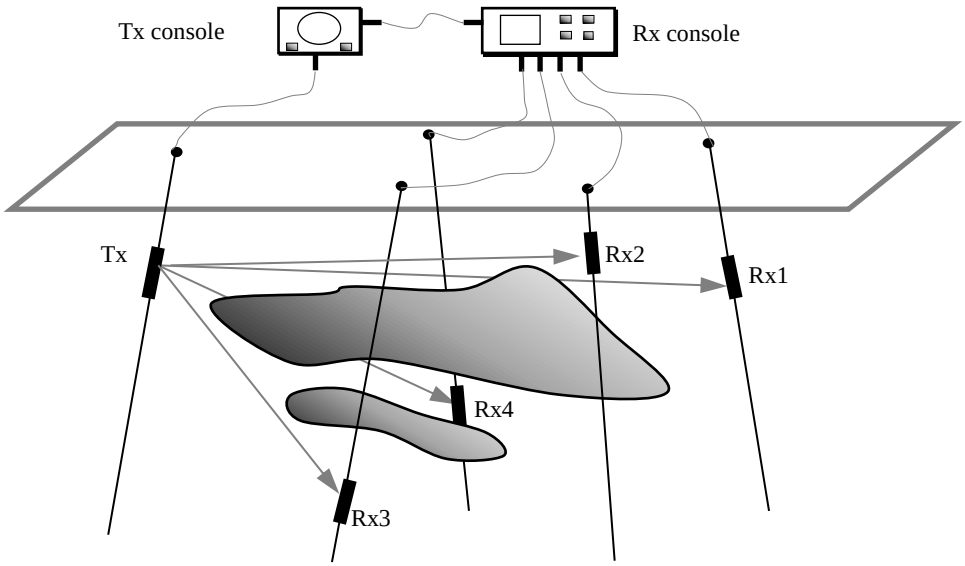

Figure 6-1. Schematic diagram of a 3D cross-hole EM exploration system with a transmitter (Tx) in one borehole and multiple receivers (Rx) in multiple boreholes.

6.3 References

Abubakar, A., van den Berg, P.M. and Mallorqui, J.J., 2002. Imaging of biomedical data using a multiplicative regularized contrast source inversion method. *IEEE Transactions on Microwave Theory and Techniques*, **50** (7), 1761-1771. doi: 10.1109/TMTT.2002.800427.

Abubakar, A., Habashy, T.M., Druskin, V.L., Knizhnerman, L. and Alumbaugh, D., 2008. 2.5 D forward and inverse modeling for interpreting low-frequency electromagnetic measurements. *Geophysics*, **73**(4), pp.F165-F177. doi: 10.1190/1.2937466.

Bloemenkamp, R.F., Abubakar, A. and Van Den Berg, P.M., 2001. Inversion of experimental multi-frequency data using the contrast source inversion method. *Inverse problems*, **17** (6), p.1611. doi: 10.1088/0266-5611/17/6/305.

Chew, W.C., 1995. *Waves and fields in inhomogeneous media* (Vol. 522). New York: IEEE press.

Joachimowicz, N., Pichot, C. and Hugonin, J. P., 1991. Inverse scattering: An iterative numerical method for electromagnetic imaging. *IEEE Transactions on Antennas and Propagation*, **39**(12), 1742-1753. doi: 10.1109/8.121595.

Korpisalo A. L. 2016. *Electromagnetic Geotomographic Research on Attenuating Material Using the Middle Radio Frequency Band*. PhD thesis, University of Helsinki, Finland.

Li, Y. and Smith, R. S., 2015. Forward modeling of radio imaging (RIM) data with the Comsol RF module. *Computers & Geosciences*, **85**, 60-67. doi: 10.1016/j.cageo. 2015.08.012.

MacLennan K., Karaoulis M. and Revil A. 2013. Complex conductivity tomography using low-frequency crosswell electromagnetic data. *Geophysics* **79** (1), E23-E38. doi: 10.1190/geo2012-0531.1.

Michalski, K.A. and Mosig, J.R., 1997. Multilayered media Green's functions in integral equation formulations. *IEEE Transactions on Antennas and Propagation*, **45** (3), pp.508-519. doi: 10.1109/8.558666

Stevens K., Watts A. and Redko G. 2000. In-mine applications of the radio-wave method in the Sudbury igneous complex. *In 2000 SEG Annual Meeting. Expanded Abstracts*, 1130-1133. doi: 10.1190/1.1815587.

Thomson, S., Hinde, S., 1993. Bringing geophysics into the mine: radio attenuation imaging and mine geology. *Exploration Geophysics* **24** (3-4), 805-810. doi: 10.1071/EG993805.

Yu L. and Edwards R. N. 1997.

On crosswell diffusive time-domain electromagnetic tomography. *Geophysical Journal International* **130** (2), 449-459. Doi: https://doi.org/10.1111/j.1365-246X.1997.tb05660.x.

Appendix A Contrast source inversion (CSI) algorithm

In this section, I will introduce the detailed process to minimize equation (4-11) in section 4.3. I use the extended contrast source inversion algorithm (van den Berg et al., 1999) to update the contrast sources w and the object profile χ alternatively. The update scheme they proposed is described below.

A.1. Updating the contrast source, w

The data error $\rho_{i,n}$ and object error $r_{i,n}$ are defined as:

$$\rho_{i,n} = f_{i,n} - G_S w_{i,n} \,, \tag{A. 1}$$

$$r_{i,n} = \chi_n u_i^{inc} - w_{i,n} + \chi_n G_D w_{i,n} \,. \tag{A. 2}$$

where, f_i is the scattered field at the receiver locations observed in a borehole (data domain S) excited by a number of incident fields $u_i^{inc}, i = 1,2, \ldots . I$ (where I is the number of transmitter locations); G_S is a matrix, each element of which is the Green's function with the source in the object domain and the receiver in the data domain; G_D is a matrix, each element of which is the Green's function with both the source and the receiver in the object domain D; subscript n denotes the nth iteration.

As $w_{i,n-1}$ and χ_{n-1} are known from the previous iteration, update w_i by

$$w_{i,n} = w_{i,n-1} + \alpha_n^w v_{i,n} \,, \tag{A. 3}$$

where, α_n^w is a real constant parameter and $v_{i,n}$ is the update direction. For $v_{i,n}$, van den Berg et al. (1999) use the Polak-Ribière conjugate gradient direction, which is given by

$$v_{i,0} = 0\,,$$

$$v_{i,n} = g_{i,n}^{w} + \frac{\mathrm{Re}\sum_k \langle g_{k,n}^{w}, g_{k,n}^{w} - g_{k,n-1}^{w}\rangle_D}{\sum_k \langle g_{k,n-1}^{w}, g_{k,n-1}^{w}\rangle_D} v_{i,n-1}\,, \tag{A. 4}$$

where

$$g_{i,n}^{w} = -\eta^S G_S^* \rho_{i,n-1} - \eta_n^D \left[r_{i,n-1} - G_D^* \left(\bar{\chi}_{n-1} r_{i,n-1} \right) \right], \tag{A. 5}$$

which is the partial derivative of equation (4-11) with respect to $w_{i,n}$. In equation (A. 5), G_S^* and G_D^* are the conjugate transpose matrices of G_S and G_D. The overbar denotes the complex conjugate. The real constant parameter α_n^w is derived by substituting equation (A. 3) into equation (4-11) and taking the partial derivative with respect to α_n^w, which is explicitly

$$\alpha_n^w = \frac{-\mathrm{Re}\sum_i \langle g_{i,n}^{w}, v_{i,n}\rangle_D}{\eta^S \sum_i \left\| G_S v_{i,n} \right\|_S^2 + \eta_n^D \sum_i \left\| v_{i,n} - \chi_{n-1} G_D v_{i,n} \right\|_D^2}\,. \tag{A. 6}$$

For the starting values of the contrast source, van den Berg et al. (1999) use the contrast source obtained by the back propagation method,

$$w_{i,0}^{bp} = \frac{\| G_S^* f_i \|_D^2}{\| G_S G_S^* f_i \|_S^2} G_S^* f_i\,. \tag{A. 7}$$

A.2. Updating the object profile, χ

If $w_{i,n}$ are known from the previous iteration, the object profile is updated by minimizing the object cost function

$$F^D(w_i, \chi) = \eta^D \sum_i \left\| \chi u_i^{inc} - w_i + \chi G_D w_i \right\|_D^2\,. \tag{A. 8}$$

Firstly, the total fields are computed with

$$u_{i,n}^{total} = u_i^{inc} + G_D w_{i,n} \,. \tag{A. 9}$$

Then, the object profile χ are updated by

$$\chi_n = \chi_{n-1} + \alpha_n^{\chi} d_n \tag{A. 10}$$

where, α_n^{χ} is a real constant parameter and d_n are the update directions. Here for d_n, use the Polak-Ribière conjugate gradient directions, which is given by

$$\begin{aligned} d_0 &= 0 \,, \\ d_n &= g_n^{\chi} + \frac{\mathrm{Re}\langle g_n^{\chi}, g_n^{\chi} - g_{n-1}^{\chi} \rangle_D}{\langle g_{n-1}^{\chi}, g_{n-1}^{\chi} \rangle_D} d_{n-1} \,, \end{aligned} \tag{A. 11}$$

where,

$$g_n^{\chi} = \frac{-\eta_n^D \sum_i (\chi_{n-1} u_{i,n}^{total} - w_{i,n}) \overline{u_{i,n}^{total}}}{\sum_j \left| u_{i,n}^{total} \right|^2} \,. \tag{A. 12}$$

To find out the constant α_n^{χ}, substitute equation (A. 10) into the object cost function,

$$F_{D,n} = \frac{\sum_i \left\| \chi_n u_{i,n}^{total} - w_{i,n} \right\|_D^2}{\sum_i \left\| \chi_n u_i^{inc} \right\|_D^2} = \frac{\sum_i \left\| (\chi_{n-1} + \alpha_n^{\chi} d_n) u_{i,n}^{total} - w_{i,n} \right\|_D^2}{\sum_i \left\| (\chi_{n-1} + \alpha_n^{\chi} d_n) u_i^{inc} \right\|_D^2} \,. \tag{A. 13}$$

Then as $F'_{D,n}(\alpha_n^{\chi}) = 0$, α_n^{χ} is found to be

$$\alpha_n^{\chi} = \frac{-(aC - Ac) + \sqrt{(aC - Ac)^2 - 4(aB - Ab)(bC - Bc)}}{2(aB - Ab)}, \tag{A. 14}$$

where, the coefficients are

$$a = \sum_i \left\| d_n u_{i,n}^{total} \right\|_D^2 \,, \qquad A = \sum_i \left\| d_n u_i^{inc} \right\|_D^2 \,,$$

$$b = \mathrm{Re}\sum_i < \chi_{n-1} u_{i,n}^{total} - w_{i,n}, d_n u_{i,n}^{total} >_D \ , \quad B = \mathrm{Re}\sum_i < \chi_{n-1} u_i^{inc}, d_n u_i^{inc} >_D \ ,$$

$$c = \sum_i \left\| \chi_{n-1} u_{i,n}^{total} - w_{i,n} \right\|_D^2 \ , \qquad C = \sum_i \left\| \chi_{n-1} u_i^{inc} \right\|_D^2 \ .$$

For the starting object profile, use the contrast sources $w_{i,0}^{bp}$ estimated with the back propagation method to calculate the initial total field $u_{i,0}^{total}$, and then

$$\chi_0 = \frac{\sum_i w_{i,0}^{bp} \overline{u_{i,0}^{total}}}{\sum_i \left| u_{i,0}^{total} \right|^2} \ . \tag{A. 15}$$

Appendix B Dyadic Green's function and integration over a grid cell

B.1. 2D dyadic Green's function

For the TE mode of the 2D electromagnetic problem, the electric fields at the point (x, z) induced by a point source at (x', z') have a horizontal component (x) and a vertical component (z). The dyadic Green's function is a matrix with four elements: G_{xx} is used to calculate the x-component field E_x generated with the x-component source current; G_{xz} is to calculate the x-component field E_x generated by the z-component source; similarly for G_{zx} and G_{zz}. From equation (4-2), the dyadic Green's function can be written as,

$$\mathbf{G}(\mathbf{r}) = (k_0^2 + \nabla^2) g(\mathbf{r}) = \left(\begin{bmatrix} k_0^2 + \frac{\partial^2}{\partial x^2} & \frac{\partial^2}{\partial x \partial z} \\ \frac{\partial^2}{\partial x \partial z} & k_0^2 + \frac{\partial^2}{\partial z^2} \end{bmatrix} \right) g(\mathbf{r}) = \begin{pmatrix} G_{xx} & G_{xz} \\ G_{zx} & G_{zz} \end{pmatrix} . \quad \text{(B. 1)}$$

According to the properties of the Hankel function of the second kind, the elements of $\mathbf{G}(\mathbf{r})$ are written as,

$$\begin{aligned} G_{xx} &= \left(-\frac{ik_0^2}{4} \right) H_0^{(2)}(k_0|\mathbf{r}|) + \frac{k_0 i}{4r} H_1^{(2)}(k_0|\mathbf{r}|) - \frac{ik_0^2 x^2}{4r^2} H_2^{(2)}(k_0|\mathbf{r}|) , \\ G_{xz} &= G_{zx} = -\frac{ik_0^2 xz}{4r^2} H_2^{(2)}(k_0|\mathbf{r}|) , \\ G_{zz} &= \left(-\frac{ik_0^2}{4} \right) H_0^{(2)}(k_0|\mathbf{r}|) + \frac{k_0 i}{4r} H_1^{(2)}(k_0|\mathbf{r}|) - \frac{ik_0^2 z^2}{4r^2} H_2^{(2)}(k_0|\mathbf{r}|) , \end{aligned} \quad \text{(B. 2)}$$

where, $|\mathbf{r}| = \sqrt{(x - x')^2 + (z - z')^2}$.

The electric fields from a 2D source can be calculated with

$$\mathbf{E}(\mathbf{r}) = \mathbf{G}(\mathbf{r})\mathbf{S}(x', z'), \tag{B. 3}$$

in which, $\mathbf{S}(x', z') = (Ids_x, Ids_z)^T$ is the source vector, where Ids_x and Ids_z are the x- and the z-component source moments respectively; the superscript T denotes transposition.

B.2. Integral of dyadic Green's function over a grid cell

To calculate the scattered field from a grid cell in the TE mode, it is necessary to integrate the dyadic Green's function over that cell. Richmond (1965) showed that the integral of the zeroth-order Hankel function of the second kind over a circle with a radius a is

$$\frac{-i}{4}\int_0^{2\pi}\int_0^{a} H_0^{(2)}(k_0|\mathbf{r}|)r'dr'd\varphi = \begin{cases} \frac{i}{2k_0^2}\left[2i - \pi k_0 a H_1^{(2)}(k_0 a)\right], & |\mathbf{r}| = 0, \\ \frac{-i\pi a}{2k_0} J_1(k_0 a) H_0^{(2)}(k_0|\mathbf{r}|), & |\mathbf{r}| > \text{a}. \end{cases} \tag{B. 4}$$

In this thesis, I chose $a = \frac{1}{2}\min(\Delta x, \Delta z)$, where Δx and Δz are the lengths of the grid cell along the horizontal and vertical direction respectively. I use the average zeroth-order Hankel function of the second kind in the circle for the whole grid cell, so the integral over a grid cell $A(x, z)$ is

$$A(x,z) = \frac{\Delta\text{x}\Delta\text{z}}{\pi a^2} g(x,z) = \begin{cases} \frac{i\Delta\text{x}\Delta\text{z}}{2\pi a^2 k_0^2}\left[2i - \pi k_0 a H_1^{(2)}(k_0 a)\right], & |\mathbf{r}| = 0, \\ \frac{-i\Delta\text{x}\Delta\text{z}}{2ak_0} J_1(k_0 a) H_0^{(2)}(k_0|\mathbf{r}|), & |\mathbf{r}| > \text{a}. \end{cases} \tag{B. 5}$$

I use the pulse function and the rooftop function from Kooij and van den Berg (1998) to derive the terms involving the higher-order Hankel functions, so the final results are

$$G_{xx} = k_0^2 A(x,z) + (\Delta x)^{-2}\big(A(x-\Delta x,z) - 2A(x,z) + A(x+\Delta x,z)\big),$$

$$G_{xz} = G_{zx} = \frac{1}{4\Delta x \Delta z}\big(A(x-\Delta x, z-\Delta z) - A(x-\Delta x, z+\Delta z) \\ - A(x+\Delta x, z-\Delta z) + A(x+\Delta x, z+\Delta z)\big), \tag{B. 6}$$

$$G_{zz} = k_0^2 A(x,z) + (\Delta x)^{-2}\big(A(x,z-\Delta z) - 2A(x,z) + A(x,z+\Delta z)\big).$$